

**Technical Report  
1046**

# **Passive Localization of Moving Emitters Using Out-of-Plane Multipath**

S.D. Coutts

**DTIC QUALITY INSPECTED 2**

30 September 1998

---

**Lincoln Laboratory**  
MASSACHUSETTS INSTITUTE OF TECHNOLOGY  
*LEXINGTON, MASSACHUSETTS*



---

Prepared for the Defense Advanced Research Projects Agency  
under Air Force Contract F19628-95-C-0002.

Approved for public release; distribution is unlimited.

19981009 127


This report is based on studies performed at Lincoln Laboratory, a center for research operated by Massachusetts Institute of Technology. This work was sponsored by the Defense Advanced Research Projects Agency, STO, under Air Force Contract F19628-95-C-0002.

This report may be reproduced to satisfy needs of U.S. Government agencies.

The ESC Public Affairs Office has reviewed this report, and it is releasable to the National Technical Information Service, where it will be available to the general public, including foreign nationals.

This technical report has been reviewed and is approved for publication.

FOR THE COMMANDER

  
Gary Tutungian  
Administrative Contracting Officer  
Contracted Support Management

Non-Lincoln Recipients

PLEASE DO NOT RETURN

Permission is given to destroy this document  
when it is no longer needed.

## **REPRODUCTION QUALITY NOTICE**

**This document is the best quality available. The copy furnished to DTIC contained pages that may have the following quality problems:**

- **Pages smaller or larger than normal.**
- **Pages with background color or light colored printing.**
- **Pages with small type or poor printing; and or**
- **Pages with continuous tone material or color photographs.**

**Due to various output media available these conditions may or may not cause poor legibility in the microfiche or hardcopy output you receive.**



**If this block is checked, the copy furnished to DTIC contained pages with color printing, that when reproduced in Black and White, may change detail of the original copy.**

MASSACHUSETTS INSTITUTE OF TECHNOLOGY  
LINCOLN LABORATORY

**PASSIVE LOCALIZATION OF MOVING EMITTERS  
USING OUT-OF-PLANE MULTIPATH**

*S.D. COUTTS*  
*Kwajalein*  
*(Work performed as member of Group 103)*

TECHNICAL REPORT 1046

30 SEPTEMBER 1998

Approved for public release; distribution is unlimited.

LEXINGTON

MASSACHUSETTS

## ABSTRACT

The purpose of this work is to establish how a moving emitter can be localized by a passive receiver through the use of out-of-plane multipath signals reflected by the terrain. This is a novel localization technique that assumes no *a priori* knowledge of the location of the multipath sources. The emitter parameters of range, heading, velocity, and altitude are estimated by exploiting the correlation between the direct-path signal and the delayed, attenuated, and Doppler modulated signals reflected by the terrain.

Two basic assumptions about the terrain scattering properties lead to different maximum likelihood (ML) estimators of emitter parameters. The first assumption is that the terrain scattering is fundamentally homogeneous; in this case the ML estimator is found to have the structure of a time-varying FIR filter. The second assumption is that the terrain scattering is fundamentally inhomogeneous and dominated by a number of discrete scatterers. This assumption leads to a two-part estimator which first estimates the scattering parameters of azimuth, differential delay, and Doppler shift, and then estimates the emitter parameters using the scatterer parameter estimates. The Cramer-Rao lower bounds of the variances for each estimator are derived and used to study estimator performance for several scenarios.

The proposed estimators are successfully demonstrated using field data collected at White Sands Missile Range during the DARPA/Navy Mountaintop program. Several extensions to the basic results are considered such as localizing pulsed and self-correlated emitters, multiple emitters, and the effects of receiver motion.

## **PREFACE**

The material presented in this report is identical to that in a dissertation submitted to Northeastern University, Department of Electrical and Computer Engineering, August 1997, in partial fulfillment of the requirements for the degree of Doctor of Philosophy.

## ACKNOWLEDGMENTS

I would like to thank many individuals, at both Northeastern and Lincoln Laboratory, for their contributions toward the successful completion of this work. I would like to thank Mr. Gerard Titi first for suggesting this fruitful research topic and also, along with Dr. Steven Krich, for providing encouragement, and support including the computer resources that permitted me to work effectively at home while maintaining a full-time position at Lincoln Laboratory. I also wish to thank Dr. Kenneth Senne for many helpful suggestions during the preparation of my ASAP presentations on this material.

I am deeply indebted to Prof. Ram Raghavan, my principal advisor, for many stimulating technical discussions and invaluable guidance on completing and writing up this work. Thanks also to committee members Dr. Ronald Fante, Dr. Robert Gabel, Prof. Hanoch Lev-Ari, Prof. David McLaughlin, and Dr. James Ward for their encouragement, help, and valued comments on draft copies of this work. Dr. Gabel's help using and interpreting the Mountaintop data was particularly appreciated. I would also like to thank Prof. Daniel Fuhrman for several useful suggestions during the early stages of this project.

I wish to thank all my friends and colleagues who have influenced this work in one way or another. I also wish to acknowledge Dr. Jen Jao who, through his example, taught me the importance of being meticulous with my work.

Finally, I am very thankful for the encouragement and moral support provided by my wife Lynn Eriksen, son Alexander, and parents Bernice and Robert Coutts. I am especially indebted to my wife Lynn. The completion of this work would not have been possible without her understanding and support.

# TABLE OF CONTENTS

Abstract	iii
Preface	v
Acknowledgments	vii
List of Illustrations	xi
List of Tables	xvi
 1. INTRODUCTION	 1
1.1 Background	1
1.1.1 Multiple Sensor Localization Techniques	1
1.1.2 Single Sensor Localization Techniques	4
1.1.3 Background Literature	5
1.2 Introduction to Localization Using Out-of-Plane Multipath	6
1.2.1 Contributions	10
1.2.2 Report Organization	10
 2. LOCALIZATION USING OUT-OF-PLANE MULTIPATH	 13
2.1 Introduction	13
2.2 Receiver Signal and Noise Models	13
2.2.1 Mountaintop Radar Receiver and Emitter	14
2.3 Bistatic Geometry and Scattering Considerations	15
2.3.1 Direct and Scattered Signal Levels	17
2.4 Localization of a Moving Emitter	18
2.4.1 Delay-Doppler Ridge	18
2.4.2 Bistatic Hough Transform	20
2.4.3 Uniqueness of Parameter Space Mapping	26
2.5 Chapter Summary	28
 3. LOCALIZATION IN HOMOGENEOUS CLUTTER	 29
3.1 Introduction	29
3.2 Basic Scattering Model	29
3.3 Statistical Formulation	30
3.4 Maximum Likelihood Estimator	32
3.5 Solution Technique	38
3.5.1 Sub-optimal Technique	38
3.6 Chapter Summary	39
 4. LOCALIZATION IN INHOMOGENEOUS CLUTTER	 41
4.1 Introduction	41
4.2 Basic Model for Inhomogeneous Scattering	41
4.3 Statistical Formulation	43
4.3.1 Part 1: Estimation of Scattering Parameters	43
4.3.2 Part 2: Estimation of Emitter Parameters	44
4.3.3 Physical Interpretation	47
4.3.4 Solution Technique	47
4.4 Chapter Summary	48



## TABLE OF CONTENTS (Continued)

5.	ESTIMATOR PERFORMANCE	49
5.1	Introduction	49
5.2	Estimator for the Homogeneous Clutter Model	49
5.2.1	Determination of the Cramer-Rao Lower Bounds	49
5.2.2	CRLB Calculations and Behavior	52
5.2.3	Monte-Carlo Simulations	60
5.3	Estimator for the Inhomogeneous Clutter Model	63
5.3.1	Parameter Covariance Calculations	63
5.3.2	Monte-Carlo Simulation	67
5.4	Application of CRLB to Real Data	68
5.5	Chapter Summary	68
6.	APPLICATION TO MOUNTAINTOP DATA	69
6.1	Introduction	69
6.2	Results Using the Estimator for Homogeneous Clutter	71
6.2.1	Data Set HOT-6067	71
6.2.2	Data Set HOT-6161	75
6.2.3	Data Set HOT-6132	78
6.3	Results Using the Estimator for Inhomogeneous Clutter	80
6.3.1	Data Set HOT-6067	82
6.3.2	Data Set HOT-6161	85
6.3.3	Data Set HOT-6132	85
6.4	Results for Reduced Emitter Power and Bandwidth	87
6.5	Chapter Summary	91
7.	EXTENSIONS TO THE BASIC RESULTS	93
7.1	Introduction	93
7.2	Moving Receiver and Emitter	93
7.3	Pulsed Emitter Waveform	95
7.4	Self-Correlated Emitter Waveform	97
7.5	Multiple Emitters	99
7.5.1	Sub-optimum Technique	100
7.5.2	Full Maximum Likelihood Approach	100
7.5.3	Maximum Likelihood EM Approach	101
7.5.4	Two Emitter Example Using the Sub-optimum Technique	102
7.6	Chapter Summary	104
8.	SUMMARY AND CONCLUSIONS	107
8.1	Summary	107
8.2	Future Research	108

## **TABLE OF CONTENTS**

### **(Continued)**

APPENDICES	111
APPENDIX A: DOPPLER TERMS FOR TWO-DIMENSIONAL APPROXIMATION	113
APPENDIX B: DOPPLER TERMS FOR THREE-DIMENSIONAL APPROXIMATION	117
APPENDIX C: DOPPLER TERMS FOR COMPLETE THREE-DIMENSIONAL SOLUTION	119
APPENDIX D: ELEMENTS OF THE FISHER INFORMATION MATRIX	125
References and Bibliography	129

## LIST OF ILLUSTRATIONS

Figure No.		Page
1.1	(a) Emitter localization via triangulation. (b) Two emitters generate four intersections resulting in two ghost or false target positions in addition to the true target positions.	2
1.2	Three sensor hyperbolic localization scheme.	3
1.3	Single sensor localization using multipath (assumes a flat earth model).	5
1.4	Top-down two-dimensional view of the radar, emitter, and three scatterers $[s_1, s_2, s_3]$ in the horizontal plane.	7
1.5	A determination of range difference, $D_i = (a_i + b_i - R)$ , and scatterer azimuth $\phi$ is not enough to determine the range to an emitter. This figure shows two bistatic triangles with the same range difference, $D$ , and scatterer azimuth, $\phi$ , but different scatterer ranges, $a_i$ , result in different emitter ranges, $R_i$ .	8
1.6	Top-down view of the radar, emitter, and three scatterers $[s_1, s_2, s_3]$ . Emitter is moving with velocity $V$ in the direction $H$ .	9
2.1	Basic model for the emitter, receiver, and multipath. The reference channel collects the emitter signal via the direct path and the multipath channel collects the signals reflected by the ground.	14
2.2	Bistatic scattering regions and geometry.	16
2.3	Bistatic delay and Doppler contours for an emitter at a range of 150 km traveling north at a velocity corresponding to a maximum Doppler shift of 200 Hz directly in front of the emitter and -200 Hz behind the emitter. The Doppler shift for the direct-path signal is zero for this geometry and the heading is 90 degrees.	19
2.4	Delay-Doppler ridge for bistatic scattering from a moving emitter and the geometry of Figure 2.3.	20
2.5	Bistatic triangle formed by the receiver, emitter, and scatterer.	21
2.6	Pseudo-code for bistatic Hough transform localization algorithm.	23
2.7	Hough transform of (a) point in delay-Doppler space is (b) a curve in the trial range-heading space.	24
2.8	(a) Three scatterers located on the delay-Doppler locus and (b) the corresponding Hough transform.	24
2.9	Localization using Hough transform. (a) Thirty scatterers on the delay-Doppler ridge are transformed to emitter parameter space (b,c,d). Parts (c) and (d) are views of the parameter space after the curves shown in (b) have been accumulated.	25

## LIST OF ILLUSTRATIONS (Continued)

Figure No.		Page
2.10	Hough transforms of a measured delay-Doppler ridge assuming three different emitter velocities.	27
2.11	Delay-Doppler ridges for the three parameter sets suggested by Figure 2.10. The delay-Doppler ridges are nearly identical.	27
2.12	Delay-Doppler ridges for the three parameter sets and a $-30$ degree receive azimuth.	28
3.1	Range and Doppler contours for a moving emitter. A reference beam pointed at the emitter directly samples the emitter waveform and a multipath beam collects the attenuated, delayed, and Doppler-shifted replicas of the emitter waveform.	31
3.2	Finite impulse response (FIR) model for system identification.	33
3.3	Emitter localization filter structure for a single multipath beam. The emitter parameter set that minimizes the output power is the ML estimate.	36
3.4	Emitter localization filter for multiple beams. The emitter parameter set that minimizes the output power is the ML estimate.	37
4.1	Range and Doppler contours for a moving emitter. A reference beam pointed at the emitter directly samples the emitter waveform, and multipath beams collect attenuated, delayed, and Doppler-shifted replicas scattered by the discrete scatterers.	42
4.2	Maximum likelihood estimator for independent scattering parameters $[D, \omega, \phi]$ .	44
5.1	Basic localization scenario for CRLB analysis.	53
5.2	Outputs from scattering model include (a) reflectivity map, (b) scattered power map, (c) delay-Doppler map, and (d) filter coefficient amplitude for an 8-degree beam at 30 degrees azimuth.	54
5.3	CRLB for the emitter parameters of (a) range, (b) heading, (c) velocity, and (d) altitude all as a function of emitter velocity.	56
5.4	CRLB for the emitter parameters of (a) range, (b) heading, (c) velocity, and (d) altitude all as a function of emitter altitude.	57
5.5	CRLB for the emitter parameters of (a) range, (b) heading, (c) velocity, and (d) altitude all as a function of receive azimuth.	58
5.6	CRLB for the emitter parameters of (a) range, (b) heading, (c) velocity, and (d) altitude all as a function of emitter heading.	59

## LIST OF ILLUSTRATIONS (Continued)

Figure No.		Page
5.7	Comparison of Monte-Carlo simulations (*) to CRLB calculations for (a) range and (b) heading.	62
5.8	(a) Emitter range and (b) heading histograms for 110 simulations. The mean range was 99.85 and the mean heading was 90.16. The solid curve represents the theoretical PDF based on the CRLB calculations.	62
5.9	CRLB for the two estimators are equivalent for the same scattering scenario.	65
5.10	CRLB versus velocity for 50 scatterers spread in azimuth from $-45$ to $+45$ .	66
5.11	Histograms for 1700 simulations. The mean of the simulations equal 99.991 km, 90.000 deg., 180.005 m/s, 7.015 km for range, heading, velocity, and altitude, respectively. The solid curve represents the theoretical PDF based on the CRLB calculations.	67
6.1	Photograph of Mountaintop installation and Lear jet emitter at North Oscura Peak, NM	69
6.2	Map showing Mountaintop radar site and location of emitters.	70
6.3	Geometry for data set HOT-6067. Emitter heading and Mountaintop boresight are given in degrees relative to true north.	71
6.4	Emitter parameter estimates of heading and velocity are determined relative to the receive antenna boresight.	71
6.5	3-D log-likelihood function for HOT-6067 at a fixed altitude.	72
6.6	Range-altitude slice for fixed heading and velocity.	73
6.7	Slices through the four-dimensional log-likelihood function at the emitter (a) range, (b) heading, (c) velocity, and (d) altitude. The dashed lines denote the true parameter values obtained via GPS.	74
6.8	Emitter SNR versus receiver azimuth for HOT-6161 using conventional and MVDR beamformers. Emitter and beam azimuthal angles are shown as vertical lines.	76
6.9	(a) Altitude and (b) range cuts through the log-likelihood functions for five multiple beams. (Data set HOT-6161.)	77
6.10	Range-heading slice through four-dimensional log-likelihood function for HOT-6161.	77
6.11	Multiple range cuts through log-likelihood function for HOT-6132. Localization is unsuccessful.	79

## LIST OF ILLUSTRATIONS (Continued)

Figure No.		Page
6.12	Delay-Doppler map shows wide Doppler spread across ( $-60$ deg) beam.	79
6.13	Estimator for scatterer parameters of delay, Doppler, azimuth, and SNR.	80
6.14	Delay-Doppler map showing energy in the delay, Doppler, and azimuth sidelobes. The delay sidelobes are the horizontal bands of energy and the Doppler sidelobes are vertical bands. Scatterers outside of the dashed lines are off of the delay-Doppler ridge and are therefore in the beam's edges or sidelobes.	81
6.15	Examples of errors produced by closely spaced scatterers. True system responses and measured responses for (a) in-phase and (b) out-of-phase combinations are shown. The two in-phase scatterers merge into a single extended scatterer while the out-of-phase scatterers seem to "repel" each other.	82
6.16	Cross-correlation plots for HOT-6067. Part (a) shows correlation vs. time, part (b) shows correlation vs. Doppler, and part (c) shows correlation vs. delay and Doppler for a single beam at $-40$ degrees. The position of each scatterer is denoted by an "x."	83
6.17	Least-squares search through parameter space for HOT-6067.	84
6.18	Least-squares search through range-heading parameter space for HOT-6132.	86
6.19	Delay-Doppler contours for the multiple-beam bounds calculation. The area that is shaded is included in the CRLB calculation.	88
6.20	Loci of constant performance versus emitter SNR and average bistatic clutter strength.	88
6.21	Emitter localization filter for showing injected noise and lowpass filter operations.	89
6.22	Cancellation ratio of localization filter versus range cut for emitter SNR ranging from 60 down to 10 dB.	90
6.23	Range-velocity slices of the log-likelihood function for (a) 700W/200 kHz and (b) 0.35W/10 kHz cases.	91
7.1	Doppler contours for (a) moving receiver, (b) moving emitter, and (c) moving receiver and emitter.	94
7.2	Bistatic triangle formed by the receiver, emitter, and scatterer.	94
7.3	Received power versus sample for (a) the direct path beam at 302 degrees (true north), and multipath beams at (b) 228 and (c) 262 degrees.	96

## LIST OF ILLUSTRATIONS (Continued)

Figure No.		Page
7.4	Map of scatterers used for the localization of data set HOT-6138.	97
7.5	Correlation in the emitter waveform can produce multiple TDOA estimates which can generate false emitter positions when using multisensor localization TDOA techniques.	97
7.6	Schematic for introducing self correlation.	98
7.7	Autocorrelation function of self-correlated emitter waveform.	98
7.8	Log-likelihood function (a) without and (b) with self-correlation. No false targets are generated.	99
7.9	Localization of two emitters. The multipath beam contains energy from both emitters. Separate reference beams collect the two emitter waveforms.	100
7.10	Conventional and MVDR spatial power spectra in dB above thermal noise for single-emitter data sets (a) HOT-6161, (b) HOT-6165, and (c) the two-emitter combination of data sets. The dashed lines represent the true emitter angles. Part (d) shows the eigenvalues for the combined data set.	103
7.11	Adapted beam patterns for the two reference beams. Spatial nulls are placed at the location of the other emitter.	104
7.12	Single and multiple emitter localization results for data set HOT-6161 and HOT-6165. Parts (a) and (b) show the single emitter results, and (c) and (d) show the multiple emitter results for HOT-6161 and HOT-6165, respectively.	105
A.1	Bistatic triangle formed by the receiver, emitter, and scatterer.	113
C.1	General three-dimensional bistatic geometry.	119
C.2	Delay-Doppler ridge for three methods of calculation. The emitter range is 100 km and its heading is 90 degrees. The altitudes for the emitter and receiver are 8 km and 1.2 km, respectively.	122

## LIST OF TABLES

<b>Table No.</b>		<b>Page</b>
2.1	Mountaintop Parameters for TSI and Emitter Localization Experiments	15
4.1	Discrete Clutter Model	42
6.1	Estimation Results for Data Set HOT-6067	75
6.2	Estimation Results for Data Set HOT-6161	76
6.3	Results for Data Set HOT-6067	84
6.4	Results for Data Set HOT-6061	85
6.5	Results for Data Set HOT-6132	86
6.6	Results for Data Set HOT-6132 With One Scatterer Removed	87
6.7	Results for Reduced Emitter Power and Bandwidth Using the Estimator for Inhomogeneous Clutter	91
7.1	Results for Data Set HOT-6138	95



# 1. INTRODUCTION

## 1.1 BACKGROUND

Passive localization of an emitting source is a problem that has received considerable interest from both the radar and sonar communities. Localization refers to the estimation of source parameters such as the range, angle, heading, velocity, and altitude or depth of a radiating source by receiving and processing the source emissions. For military applications, a passive localization system offers advantages over an active one because it operates covertly. That is, it can perform the localization without active transmissions that could give away its own position. Strictly speaking, a radar operating in a passive mode is not acting as a radar but as a radio frequency (RF) receiver. Hence, when the term radar is used in this report, we are usually referring to the radar receiver.

Classes of emitters that will be considered include communications transmitters, pulse transmitters, and noise transmitters or jammers. A jammer is a high power emitter that radiates a noise-like signal designed to disable a radar or sonar system by increasing the noise level [1]. Very-low sidelobe or adaptive antennas can be employed to reduce the susceptibility to jamming via the antenna sidelobes [2]–[5]; however, if the jammer is in the active sensor's mainbeam, the sensor may be completely disabled. Thus, an active sensor is not able to determine the range to a jammer because it cannot detect its own relatively weak echoes traveling the same propagation path as the very strong jamming signal. The jammed sensor will be able to determine the jammer azimuth and elevation angles by passively receiving and performing angle-of-arrival estimation (AOA), or direction finding (DF), using the jammer's strong direct-path signal. However, these angle measurements alone do not yield the range to the jammer. Since emitters of this type often represent important targets, techniques to localize these emitters are important to both the radar and sonar communities.

The work presented in this report is primarily geared towards radar with the Mountaintop UHF phased-array radar as the principal sensor. Extensive Mountaintop data containing airborne emitters have been collected for the analysis of terrain scattered interference (TSI) [6],[7] (or so-called "hot clutter [8]") and bistatic clutter [6],[9],[10]. This same data will be used to study emitter localization techniques presented herein [11],[12]. The potential use of TSI for emitter localization was suggested first by Gerard Titi [11].

Before introducing the novel out-of-plane multipath localization concept that is the subject of this report, we first review some basic multisensor and single-sensor localization techniques. These are presented to introduce the localization problem and to define some commonly used localization terms.

### 1.1.1 Multiple Sensor Localization Techniques

There are numerous passive techniques that can be used to localize an emitting source. For radio-wave emitters, [13] briefly discusses nineteen passive ranging techniques, and for underwater acoustic sources, [14] discusses several ranging and direction finding techniques. A few of these

techniques are discussed in this section in order to introduce some localization terms and concepts. They provide background for the single-sensor techniques described in the next section and the out-of-plane multipath technique introduced in Section 1.2.

One of the simplest forms of localization is triangulation which is shown in Figure 1.1 (a) and (b). In part (a), two physically separated but cooperating receivers obtain angle-of-arrival estimates (AOA), which are also called direction lines, or lines-of-position (LOP), by measuring the angle to the emitter using some angle measurement technique. (A discussion of AOA and DF techniques can be found in [15]–[17].) The master station receives angle measurements from the other stations in the localization network, over data links, and determines the emitter position. Cooperating AWACS (E3A) radars utilize a passive mode to localize emitters in this manner [18]. If more than one emitter is present, false associations may occur and generate false targets that are commonly referred to as ghosts. This is illustrated in Figure 1.1 (b) for a two station, two emitter scenario. Ghost targets can often be removed by employing cross-correlation and time-difference of arrival (TDOA) techniques [19],[20].

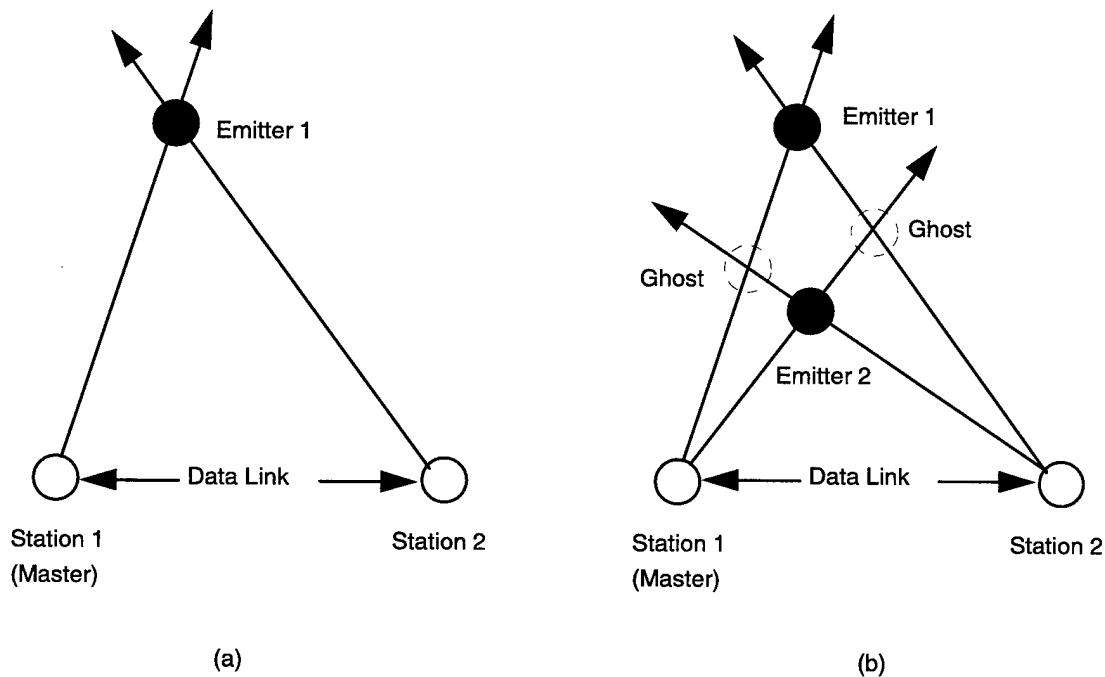
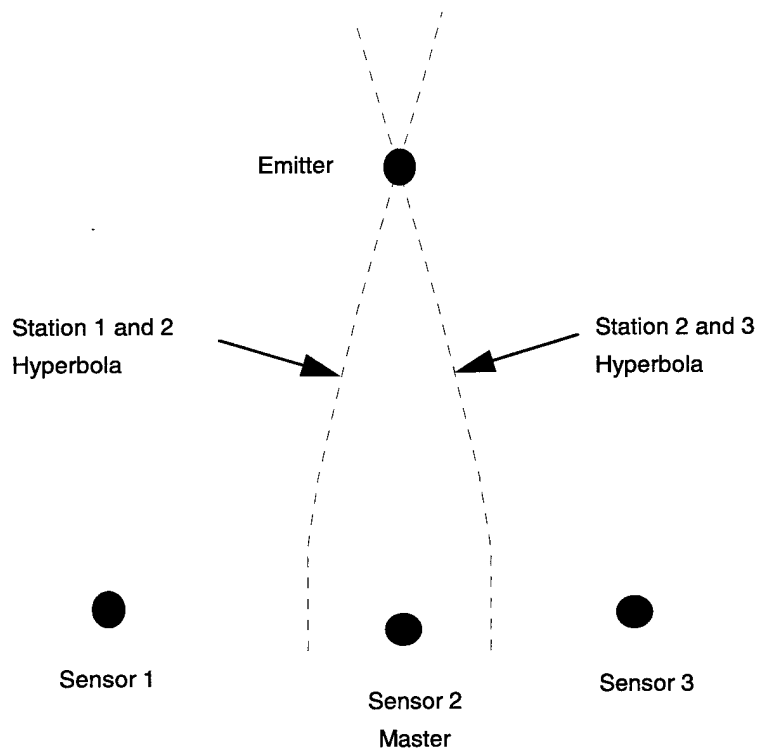


Figure 1.1. (a) Emitter localization via triangulation. (b) Two emitters generate four intersections resulting in two ghost or false target positions in addition to the true target positions.

Hyperbolic measurements systems use TDOA measurements instead of angle measurements to localize an emitter. An example using three isotropic sensors and an emitter in a horizontal two-dimensional plane is shown in Figure 1.2. The master station receives replicas of the emitter waveform from the other stations over a data link. TDOA estimates are obtained by cross-correlating the emitter signals received at the various stations. The time differences specify hyperbolic curves and the intersection of these curves yields the emitter position. For localization in three dimensions, four sensors are commonly used and the emitter position is taken from the intersection of three hyperboloids. If there is relative motion between the emitter and the sensors, differential Doppler measurements may also be utilized. Hybrid localization systems combine multiple discriminants, such as TDOA, AOA, or differential Doppler.



*Figure 1.2. Three sensor hyperbolic localization scheme.*

### 1.1.2 Single Sensor Localization Techniques

Single-sensor localization techniques rely on virtual sensors to perform localization estimates. The virtual sensors are formed by multiple propagation paths (multipath) or by sensor motion. Once the virtual sensors are realized, localization can be performed using multisensor techniques like those described in the preceding section. The obvious advantage to the single-sensor techniques is that only a single sensor is required; no multisensor coordination or data links are necessary. The single passive sensor functions independently. Passive localization using out-of-plane multipath, the topic of this report, is a single sensor technique.

Sensor motion, such as that achieved with an airborne radar receiver, permits AOA measurements to be performed at multiple sensor positions. The AOA measurements are used to triangulate the emitter in the same manner as the multisensor technique illustrated in Figure 1.1(a). Since the sensor measurements are performed sequentially, this technique is often called sequential localization. This method works well when the receiver is moving and the emitter is stationary but may have difficulties when the emitter is moving. In contrast, we shall see in Chapter 5 that the performance of the estimators designed in this report improves with increasing emitter velocity.

Several in-plane multipath techniques may be used to perform single-sensor localization. A few simple examples are shown in Figure 1.3. This figure shows a radar using reflections from the ground or ionosphere, and a sonar using reflections from the ocean floor or surface, to localize the emitter. The virtual sensors are the images of the true sensor generated by multipath. Autocorrelation of the sensor signal yields TDOA estimates between the direct propagation path and the reflected paths. Angle measurement techniques can be used to measure the angle of arrival of the direct and reflected propagation paths. The TDOA or AOA measurements, when combined with knowledge of the position of the reflecting surfaces, are used to perform the localization using the multisensor techniques described in the preceding section.

Knowledge of the position of reflecting surface is essential for these single-sensor localization techniques. That is, the high-frequency (HF), over-the-horizon (OTH) radar receiver needs to know the height of the ionosphere, and the general radar receiver using ground reflection needs to know its altitude relative to the reflection point. Similarly, the sonar needs to know its depth and distance to the ocean floor. Errors in knowledge of the position of the reflecting surfaces translate directly to errors in emitter localization. The out-of-plane multipath technique developed in this report requires no prior knowledge of scatterer location.

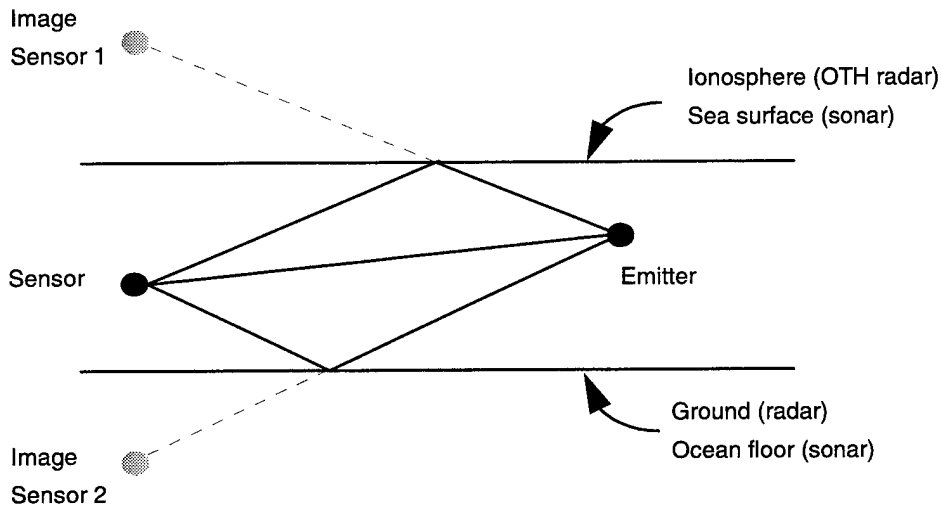


Figure 1.3. Single sensor localization using multipath (assumes a flat earth model).

### 1.1.3 Background Literature

The preceding two sections provide a brief qualitative introduction to localization using multiple- and single-sensor techniques. The reader is referred to the very rich literature on emitter localization if more information is required. Some of the papers we found helpful are indicated in this section.

Most of work in the emitter localization literature discusses one or more of the four basic components of the problem: *the geometrical model*, *the statistical model*, *parameter estimation*, and *the accuracy or performance assessment*. The *geometrical model*, including sensor configurations, is unique for a specific problem. The equations describing the emitter and source geometries for localization are usually nonlinear, such as the intersection of hyperbolas discussed in Section 1.1.1. The *statistical model* usually describes measured data collected by the sensors in the presence of measurement noise. For example, when measurement noise is present, more than two hyperboloids will not intersect at a single point. The problem becomes that of determining the most likely position and assessing the accuracy of the result. The *parameter estimation* component is concerned with determining the best emitter parameter set based on some optimization criterion, such as least-square error or a maximization of the likelihood function. The *accuracy or performance assessment* usually contains a determination of the Cramer-Rao lower bounds (CRLB) which specify the minimum variance an unbiased estimator can achieve. If sub-optimum parameter estimators are employed, they are usually accompanied by an evaluation of bias and a comparison to the CRLB.

A discussion of statistical models and the other components of the localization problem can be found in [21]–[23] for many of the multisensor localization techniques. These references linearize the

nonlinear geometrical equations by expanding in a Taylor series and retaining only the linear terms. These results are expanded to include sensor position uncertainty in [24],[25]. Single sensor localization techniques using reflection from the ionosphere are described in [26],[16],[27]–[29]. These techniques can be thought of as vertical triangulation [26], and the localization sensors are called single-site locators (SSL). Sequential localization techniques for stationary emitters and moving sensors are found in [20],[30]. Sequential techniques that also employ Doppler shift are found in [31],[32]. The accuracy of systems using virtual sensors generated by multipath is discussed in [33] for two sensors and two paths (direct and reflected) and in [34] for an arbitrary number of sensors and paths. The sonar practice of matched field processing (MFP) [35]–[37], is a technique whereby a plane-wave beamformer is replaced by a generalized beamformer with weighting vectors computed from a multipath model of the ocean waveguide. These techniques localize a source in range, depth, and azimuth, and may include as many as forty or more rays or modes in the multipath model. It is considered an inverse problem that is solved by constructing an “infinite” number of forward solutions on a parameter grid and selecting the best match to the observed signal.

Localization methods that utilize relative time delay or Doppler frequency difference estimates (i.e., TDOA or FDOA estimates) can draw upon the extensive literature on these subjects. The maximum likelihood estimator for time-delay estimation is based on cross-correlation and is described in [38],[39]. Reference [39] is a tutorial review of coherence and time-delay estimation which contains an additional 74 references. Time-delay estimation using LMS adaptive tapped-delay-line filters is described in [40],[41]. Estimation of differential Doppler shift is discussed in [42]. The maximum likelihood estimator for the joint estimation of differential delay and Doppler is discussed in [43] where it is shown that the estimation of differential Doppler is uncoupled from differential delay and phase estimators. A discussion of localization using both TDOA and FDOA methods for a stationary transmitter and two moving receivers can be found in [44],[45].

## 1.2 INTRODUCTION TO LOCALIZATION USING OUT-OF-PLANE MULTIPATH

This section introduces the concept of localization using out-of-plane multipath that is the subject of this report. This is a new localization technique that makes no *a priori* assumptions about the locations of the scatterers. The acoustic (sonar) and electromagnetic (radar) multipath examples depicted in Figure 1.3 were examples of in-plane multipath localization. The direct propagation path and the forward scattered path are contained in a vertical plane perpendicular to the horizontal reflecting surfaces. These are specular reflections from flat surfaces that obey Snell’s law of reflection, i.e., the angle of incidence equals the angle of reflection. Out-of-plane scattering refers to reflections from scatterers in the horizontal plane and is illustrated in Figure 1.4, which shows a receiver, emitter, and reflections from three scatterers. These reflections are much weaker than the in-plane reflections described above but for a strong emitter such as a jammer, they may be appreciable. The fact that these reflections are significant is evidenced by the interest in the terrain scattered interference (TSI) problem [6],[8]–[10]. These papers describe the use of adaptive signal processing techniques to remove the TSI signals from the desired radar signal. The unwanted jammer reflections described in those papers are the same signals that will be

exploited here to perform emitter localization. This is yet another instance of the adage “One radar’s clutter is another radar’s target [46].”

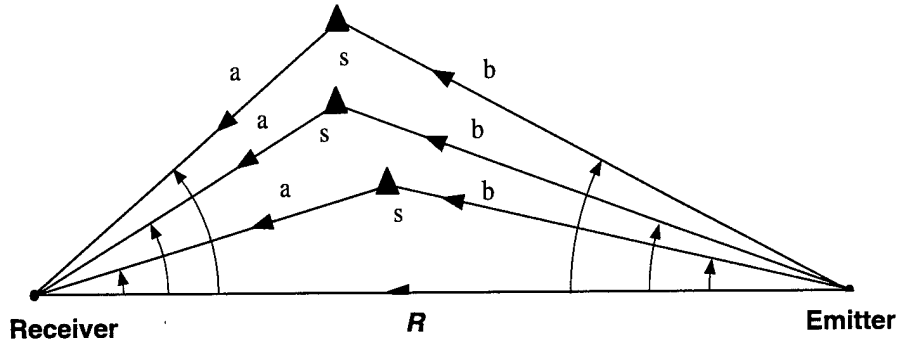


Figure 1.4. Top-down two-dimensional view of the radar, emitter, and three scatterers  $[s_1, s_2, s_3]$  in the horizontal plane. (A three-dimensional view of this geometry is provided in Figure 2.2.)

Before developing the out-of-plane multipath localization concept further, we need to make some assumptions about the capabilities of the receiver. The receiver must be capable of performing direction-finding or angle estimation in the horizontal plane. That is, the receiver is capable of measuring the angle-of-arrival of the emitter and azimuthal angle,  $\phi_i$ , of the scatterers. The angle of the emitter is used to orient the coordinate system and is thus set to zero degrees in this section. In addition to estimating the angle of the scatterers, the receiver must also be capable of estimating the time difference of arrival (TDOA),  $\tau_i$ , between the emitter direct path and the scattered paths. As we shall see below, the receiver must also be capable of measuring the Doppler frequency difference of arrival (FDOA),  $f_i$ , for the direct and scattered paths. The Mountaintop system [6] meets these requirements. This system has a nominal bandwidth of 200 kHz, a beamwidth of 8 degrees, and a center frequency of 435 MHz.

To proceed with our development, we first consider the case of TDOA measurements,  $[\tau_1, \tau_2, \tau_3]$ , and angle measurements,  $[\phi_1, \phi_2, \phi_3]$ , for the three scatterers and a stationary emitter shown in Figure 1.4. Can we localize the emitter using this information? Each scatterer forms a bistatic triangle with sides  $a_i$ ,  $b_i$ , and  $R$ , where  $R$  is the desired localization quantity of emitter range. The TDOA is  $\tau_i = (a_i + b_i - R)/c$ , where  $c$  is the speed of light. The TDOA estimates are converted to range-difference measurements by multiplying by the speed of light,  $D_i = (a_i + b_i - R)$ . This relation and the law of cosines,  $b_i^2 = a_i^2 + R^2 - 2a_i R \cos \phi_i$ , can be solved for  $R$  in terms of the range-difference estimates  $D_i$ , and range to the scatterer  $a_i$ , giving

$$R = \frac{a_i D_i - D_i^2 / 2}{D_i - a_i + a_i \cos \phi_i}. \quad (1.1)$$

Similar equations arise in bistatic radar problems where  $R$  is the range to a target and  $a_i$  is the distance from the bistatic receiver to the bistatic transmitter [47]. The three scatterers give rise to three equations; however, there are four unknowns: the three scatterer ranges,  $[a_1, a_2, a_3]$ , and the desired quantity,  $R$ . For  $N$  scatterers, there will be  $N+1$  unknowns and the system remains underdetermined with infinitely many solutions. Therefore, we cannot determine the range to this emitter without *a priori* knowledge of the scatterer locations. This is demonstrated graphically in Figure 1.5 which shows two bistatic triangles with the same azimuth  $\phi$ , and range difference  $D = a_1 + b_1 - R_1 = a_2 + b_2 - R_2$ . However, if the range to a single scatterer,  $a$ , were known, along with the measured scatterer azimuth  $\phi$  and range difference  $D$ , the emitter range could be determined using a single application of (1.1). This is the case where *a priori* knowledge of the scattering points is available and is similar to the single-sensor techniques described in Section 1.1.2. This case will not be explored in this report.

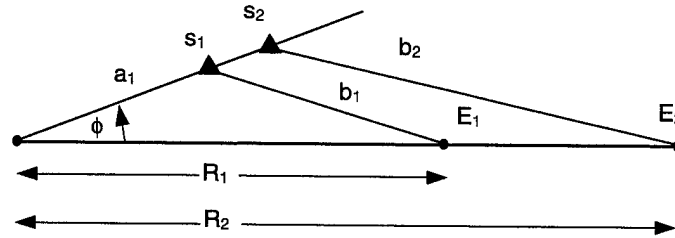


Figure 1.5. A determination of range difference,  $D_i = (a_i + b_i - R)$ , and scatterer azimuth  $\phi$  is not enough to determine the range to an emitter. This figure shows two bistatic triangles with the same range difference,  $D$ , and scatterer azimuth,  $\phi$ , but different scatterer ranges,  $a_i$ , result in different emitter ranges,  $R_i$ .

We now consider the case of an emitter moving with velocity  $V$  and direction or heading  $H$ . The emitter motion produces Doppler shifts in the scattered and direct-path signals that provide additional information that can be used to localize the emitter. Specifically, the Doppler shifts provide information that may be used to determine the angles  $[\gamma_1, \gamma_2, \gamma_3]$  which are shown in Figure 1.6. With  $\gamma_i$  determined, all the angles of the bistatic triangle are known since  $\alpha_i = 180 - \phi_i - \gamma_i$  and  $\phi_i$  was measured by the receiver. With the angles known, the range  $R$  can be determined using the law of sines and the measured range difference  $D_i$  by writing

$$R = \frac{D_i}{\left( \frac{\sin \gamma_i}{\sin \alpha_i} + \frac{\sin \phi_i}{\sin \alpha_i} - 1 \right)} \quad (1.2)$$



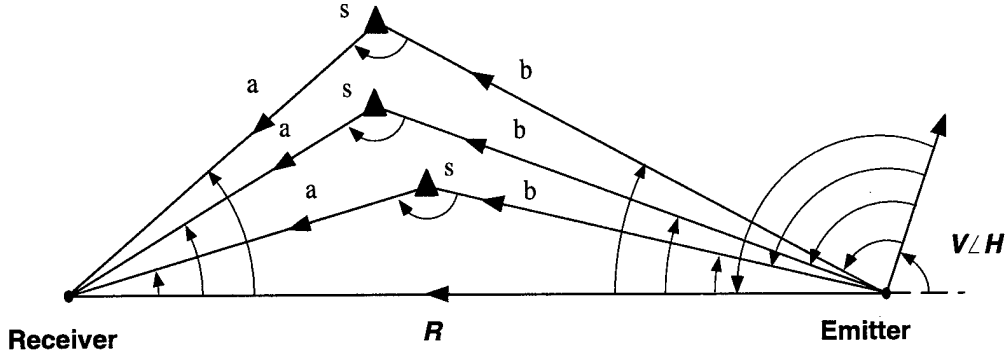


Figure 1.6. Top-down view of the radar, emitter, and three scatterers  $[s_1, s_2, s_3]$ . Emitter is moving with velocity  $V$  in the direction  $H$ .

The receiver cannot measure the absolute Doppler shift of the emitter direct-path signal and the individual scattered signals because it does not know the original emitter waveform. Instead, the relative Doppler shift between the direct and scattered paths is obtained using cross-correlation techniques. The observable quantity is the Doppler frequency difference (FDOA) for the direct and scattered signal paths. Denoting the Doppler shift for the direct path as  $f_{dp}$  and the scattered path as  $f_s$ , the differential Doppler shift is  $f = f_s - f_{dp}$ . With measurements of differential Doppler  $f_i$  for each scatterer, the desired angle  $\gamma_i$  can be written as

$$\gamma_i = -H + \cos^{-1} \left( \cos(H) - \frac{f_i \lambda}{V} \right), \quad (1.3)$$

where  $\lambda$  is the wavelength corresponding to the center of the receiver narrowband filter,  $V$  is the emitter velocity, and  $H$  is the emitter heading. The derivation of this equation is contained in Section 2.4.2. It is derived based on a two-dimensional approximation that ignores emitter altitude. This is a common approximation for bistatic radar problems because the emitter range is usually much greater than the emitter altitude [48]. A more general three-dimensional treatment will be used for the estimation of emitter altitude, however.

We proceed by using equation (1.3) in (1.2) to yield

$$R = \frac{\tilde{D}_i}{\left( \frac{\sin \gamma_i(H, V, \tilde{f}_i)}{\sin \alpha_i(H, V, \tilde{f}_i)} + \frac{\sin \tilde{\phi}_i}{\sin \alpha_i(H, V, \tilde{f}_i)} - 1 \right)}, \quad (1.4)$$

which expresses the emitter range  $R$  in terms of its velocity  $V$ , heading  $H$ , and the measured quantities for each scatterer  $[\tilde{f}_i, \tilde{D}_i, \tilde{\phi}_i]$ . The tilde was added to indicate that these quantities are measured. These equations are highly nonlinear and must be solved numerically. Since there are three unknowns  $[R, H, V]$  at least three scatterers with corresponding estimates of differential Doppler  $f_i$ , differential range  $D_i$ , and azimuth  $\phi_i$  are required. In practice, a large number of scatterers will be used to improve estimation accuracy and to eliminate ambiguities or ghosts.

In this section, the *localization using out-of-plane multipath* concept was introduced. The technique uses a combination of scatterer AOA, TDOA, and FDOA measurements resulting in a set of nonlinear equations that can be solved numerically. This approach is based on an inhomogeneous clutter assumption because it relies on the presence of a number of dominant scattering points and distinct propagation paths. No prior assumptions about the positions of the scattering elements are assumed, however. A homogeneous approach that makes different assumptions about the characteristics of the bistatic clutter will be developed as well. The basic elements of the localization problem, including the geometrical model, statistical model, parameter estimators, and an accuracy assessment, will be developed for both the homogeneous and inhomogeneous clutter models.

### 1.2.1 Contributions

The fundamental contribution is the development of single-sensor emitter localization techniques that utilize out-of-plane multipath signals to localize moving emitters in range, heading, velocity, and altitude. More specific contributions include:

1. The development of the necessary geometrical relations required to localize emitters using multipath.
2. The development of statistical models for the description of emitter multipath signals.
3. The design of estimators for the localization of moving emitters using out-of-plane multipath with no *a priori* knowledge of scatterer locations. Both homogeneous and inhomogeneous scattering models are considered.
4. The determination of estimation accuracy via the Cramer-Rao lower bounds on emitter parameter variance.
5. The demonstration of the effectiveness of the estimators using Mountaintop field data containing airborne emitters.
6. The examination of several extensions to the basic results, such as the localization of multiple emitters, effects of receiver motion, and performance for various emitter waveforms.

### 1.2.2 Report Organization

This report contains eight chapters and four appendices. Two estimators will be designed that are based on two bistatic clutter modeling approaches. The first approach is to assume that the bistatic clutter is essentially homogeneous and this leads to one estimator design. The second approach is to assume that the bistatic clutter is inhomogeneous and dominated by some number of discrete scatterers. This leads to an alternative estimator design. Separate chapters will be devoted to the development of each estimator. The contents of each chapter are considered below.

Chapter 1 (this chapter) provides background on general localization techniques and introduces the out-of-plane localization concepts. Chapter 2 extends this introduction further describing in more detail the bistatic scattering geometry and its use for emitter localization. A bistatic Hough transform is developed that can detect an intensity locus or ridge in bistatic delay-Doppler space. This will be used to examine ambiguities that may occur using this localization technique.

In Chapter 3 an estimator is designed based on the assumption that the bistatic clutter is essentially homogeneous. A statistical formulation is presented and the maximum likelihood estimator is determined for an additive Gaussian noise assumption. The estimator is found to have the structure of a time-varying finite impulse response (FIR) filter. The complex filter coefficients are determined using least squares. These coefficients are treated as nuisance parameters that are estimated along with the desired emitter parameters. Optimum and sub-optimum estimation techniques will be presented.

In Chapter 4 an estimator is designed based on the assumption that bistatic clutter is inhomogeneous and dominated by a number of discrete scatterers. This model requires a two-part estimation procedure. The receiver first estimates the pertinent scattering parameters, such as relative time delay,  $\tau$ ; differential Doppler,  $f$ ; azimuth,  $\phi$ ; and amplitude,  $a$ , for some number of the dominant scatterers. The scatterer estimates are then used to estimate the emitter parameters. The highly nonlinear localization equations are linearized by using a Taylor series expansion and retaining only the linear terms.

Chapter 5 contains a discussion of the performance of the estimators designed in Chapters 3 and 4. The Cramer-Rao lower bounds (CRLB) are determined and evaluated for various localization scenarios. The effect of varying the emitter parameters of range, heading, velocity, altitude, and power, as well as the receiver parameters of bandwidth, beamwidth, steering direction, integration time, etc., will be considered. Monte-Carlo simulations are performed to validate the bounds calculations and overall implementation of the estimators prior to their use with field data.

In Chapter 6 we use the estimators designed in Chapters 3 and 4 to localize airborne emitters contained in Mountaintop data collected at the White Sands Missile Range (WSMR). In this chapter we localize several emitters using both the homogeneous and inhomogeneous techniques. Estimation errors obtained with real data are compared to the CRLB. This chapter serves to demonstrate the results presented in the three previous chapters using experimental field data. Problems encountered when applying theoretical results to experimental data will be discussed.

In Chapter 7 we show how the basic results could be extended to include a broader range of scenarios and class of emitter signals. We discuss how to incorporate Doppler modulation generated by a moving receiver as well as that generated by the moving emitter. We also consider the localization of multiple emitters. In addition, various emitter waveforms are examined including pulsed, periodic, and self-correlated waveforms. Generally these waveforms cause problems for localization schemes because multiple peaks arise in auto- and cross-correlation functions. The multiple peaks may generate a large number of false emitters or ghosts. However, we shall see that the out-of-plane multipath technique offers some immunity against these problems because it uses FDOA as well as TDOA information in the multipath signals. The FDOA information arises from the Doppler shifts generated by the *true* emitter which may be effective in eliminating ghosts.

Chapter 8 contains a summary and conclusions as well as suggestions for future research.

Four appendices are included that contain the necessary mathematical details to support the estimator designs and the CRLB calculations.

## 2. LOCALIZATION USING OUT-OF-PLANE MULTIPATH

### 2.1 INTRODUCTION

This chapter contains additional background and introductory information necessary to develop the out-of-plane multipath estimation techniques that are the subject of this report. It begins with the basic signal and noise models for the receiver. Properties of the emitter waveform and receiver noise are also described. A description of the bistatic scattering geometry and its use in solving the emitter localization problem is also provided. The chapter concludes with the development of a bistatic Hough transform which will be used to perform emitter localization graphically and for examining potential ambiguities that may arise when using out-of-plane multipath for emitter localization.

### 2.2 RECEIVER SIGNAL AND NOISE MODELS

The three major components to this problem are the emitter, the receiver, and the ground. These components are shown in Figure 2.1. The receiver samples the emitter waveform directly using a reference channel and the scattered replicas of the waveform using the multipath channel. One or more multipath channels may be used. Each channel consists of a directive antenna beam, a mixer, a lowpass filter, and an analog-to-digital (A/D) converter. The directive antenna beams permit angle measurement in the horizontal plane. No directivity in the vertical or elevation plane is assumed. This assumption is consistent with airborne surveillance radars, such as the E2C or E3A, which generally have small vertical apertures.

The received signals for each channel are amplified, mixed, filtered, sampled, and stored for processing. The amplifier is noisy and contributes additive, zero-mean, white Gaussian noise which is independent from sample to sample as well as from channel to channel. A quadrature mixer shifts the center frequency from  $f_0$  to zero-Hz baseband. A lowpass filter band limits the white Gaussian noise. The bandwidth of the lowpass filter is matched to the bandwidth of the emitter waveform to maximize the signal-to-noise ratio of the received signals. The result is a narrowband, complex amplitude or complex envelope representation of the original signal received at the antenna terminals. This signal is sampled by the A/D converter above the Nyquist rate to avoid aliasing. This process of reducing a narrowband signal to its complex amplitude representation is described in many texts; see, for example, [4],[49].

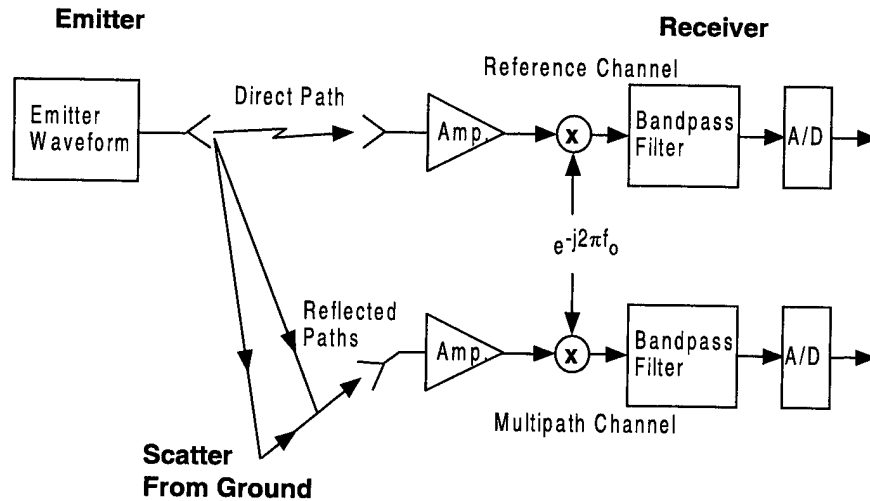


Figure 2.1. Basic model for the emitter, receiver, and multipath. The reference channel collects the emitter signal via the direct path and the multipath channel collects the signals reflected by the ground.

### 2.2.1 Mountaintop Radar Receiver and Emitter

The localization techniques developed in this report will be demonstrated with field data collected as part of the DARPA/NAVY Mountaintop Program [6]. This program utilized the 14-element phased-array radar system RSTER (Radar Surveillance Technology Experimental Radar) [50] and was designed to support the evaluation of space-time adaptive processing (STAP) algorithms [51] in the presence of clutter and jamming. Jamming was provided by an airborne emitter containing a 2 kW transmitter carried by a Lear Jet. The emitter waveform was a 600 kHz pseudo-noise (PN) sequence. The phased-array antenna permitted the simultaneous collection of multiple receive beams. The major system parameters are listed in Table 2.1.

**TABLE 2.1****Mountaintop Parameters for TSI and Emitter Localization Experiments**

Parameter	Value
Antenna Gain	29 dBi
Antenna Type	14 El. Phased Array
Antenna Element Gain	17.5 dBi
Operating Frequency	400-500 MHz
Instantaneous Bandwidth	200 kHz
Noise Figure	8 dB
Beamwidth - Azimuth	8 degrees
Beamwidth - Elevation	6 degrees
Radar PRF	312.5 Hz
Max. Coherent Time	153.5 ms (48 PRIs)
Receiver Altitude	2.43 km MSL, ~1.2 km AGL
Airborne Emitter Power	2 kW over 600 kHz
Emitter Altitude	~9.2 km MSL, ~8 km AGL

**2.3 BISTATIC GEOMETRY AND SCATTERING CONSIDERATIONS**

The geometry that describes bistatic scattering is illustrated in Figure 2.2. Three angles are required to describe this geometry. The angle of incidence is denoted as  $\theta_i$  and the scattered angle of incidence is denoted as  $\theta_s$ . The out-of-plane angle is denoted as  $\theta_o$  and is defined as shown. Instead of incidence angles, the complementary depression angles are sometimes used. Also, some investigators use the bistatic angle instead of the out-of-plane angle when describing bistatic scattering. This is the angle subtended by the incident and scattered rays.

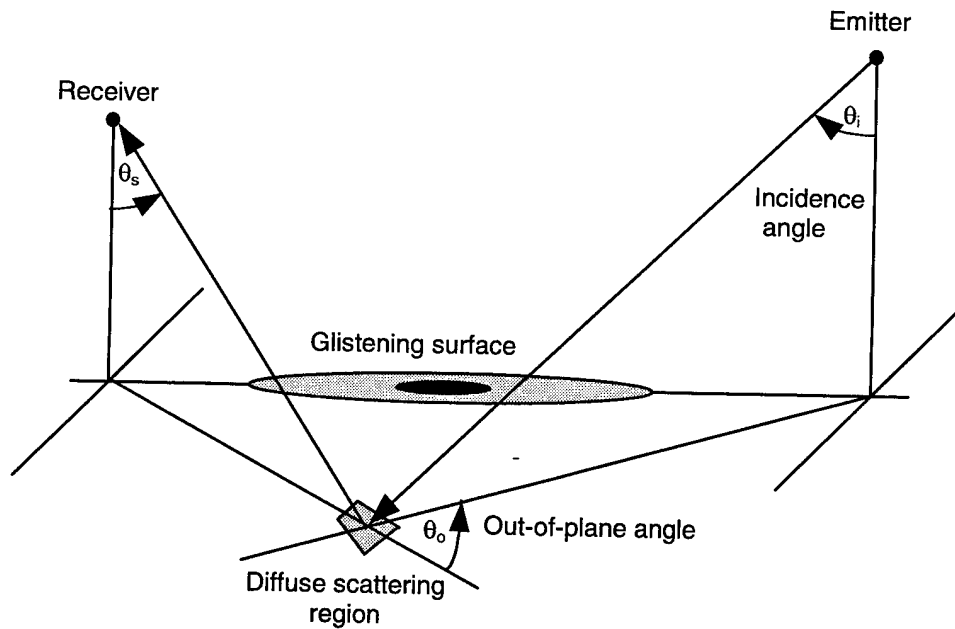


Figure 2.2. Bistatic scattering regions and geometry.

There are three scattering regions evident in Figure 2.2: the specular point, the glistening surface, and the diffuse scattering region. The strongest scattering occurs at the specular point (or region) which is represented by the darkest shading in the figure. At this point the out-of-plane angle is zero and the angle of incidence is equal to the angle of reflection. This area is comprised of the first several Fresnel zones [52] and is typically small. Image theory can be used to determine the contribution due to the specular point. Surrounding the specular point is the glistening surface that is comprised of quasi-specular points formed by favorably tilted planes or facets. This is an area of strong scattering present for small out-of-plane angles near zero. The scattering mechanism at work in the glistening surface is plane boundary reflections from tilted planes that are physically large compared to a wavelength. (Most of us have experienced an optical version of a glistening surface when viewing the reflection of the sun or moon in a body of slightly rough water.) The third area of bistatic scattering is the diffuse scattering which is the weakest form of scattering. Here the out-of-plane angle is large so that, neglecting discrete scatterers, there are usually no planes favorably tilted for generating quasi-specular returns. Instead, the scattering mechanism is Bragg resonant scattering which is characterized by small perturbation theory and the scattering strength is proportional to the small-scale surface roughness spectrum. Here the deviations of the surface height about its mean are assumed to be smaller than a wavelength. More detail on bistatic scattering and bistatic clutter modeling can be found elsewhere [10],[53]–[55]. Note that the localization techniques that are the subject of this report do not rely on a specific scattering model or mechanism; the only requirement is that out-of-plane bistatic scattering is present.



The out-of-plane scattering is the weakest of the three types of bistatic scattering described above, but it is this weak scattering that will be used for localization. A principal reason why the out-of-plane scattering is useful is that the scattered signals are easily resolved, in delay, Doppler, and azimuth, from the strong direct-path signal. It is generally not possible to resolve the glistening surface or the specular multipath point from the direct path because the differential time of arrival is too small to be observed with narrowband receivers. For example, using the altitudes for Mountaintop in Table 2.1 and an emitter slant range of 200 km, the path length of the in-plane specular multipath route is 200.096 km. The difference of 96 m corresponds to a time difference of arrival of only 0.32  $\mu$ s. This would require receiver bandwidths exceeding 3 MHz to resolve using standard correlation techniques. A similar argument holds for angle measurements. The specular multipath and glistening surface are at the same azimuth angle as the direct path and the separation in elevation is a small fraction of the elevation beamwidth that cannot be resolved using conventional beamforming techniques.

### 2.3.1 Direct and Scattered Signal Levels

The signal transmitted by the emitter travels to the receiver via the direct propagation path and reflections from the ground. The received power due to the direct path is

$$P_{dp} = \frac{P_t G_t G_r \lambda^2}{(4\pi R)^2}, \quad (2.1)$$

where  $P_t$  is the emitter transmit power,  $G_t$  is the transmit antenna gain,  $G_r$  is the receive antenna gain,  $R$  is the range from the emitter to the receiver, and  $\lambda$  is the receiver wavelength. The aperture of the receive antenna  $A_r$  is related to the gain by  $A_r = G_r \lambda^2 / 4\pi$ . The effective radiated power (ERP) is the product of the transmitter power  $P_t$  and the transmitter gain  $G_t$ .

The average power reflected from a differential patch of ground  $dP_r$  is proportional to the scattering cross section per unit area,  $\sigma_0$ , times the area of the patch,  $ds$ . The total average power received is obtained by integrating the differential power over the area illuminated by the transmitter and receiver antenna patterns in

$$P_r = \iint_{\text{area}} \frac{P_t G_t G_r \lambda^2 \sigma_0}{(4\pi)^3 R_t^2 R_r^2} ds, \quad (2.2)$$

where  $R_t$  and  $R_r$  are, respectively, the ranges from the transmitter and the receiver to the differential patch of ground  $ds$ . This expression is the area-extensive bistatic radar equation [47]. The received power from a discrete scatterer, such as a water tower, building, or terrain feature, can be obtained using the standard bistatic radar equation given by

$$P_r = \frac{P_t G_t G_r \lambda^2 \sigma}{(4\pi)^3 R_t^2 R_r^2}, \quad (2.3)$$

where  $\sigma$  is the radar cross section (RCS) of the discrete scatterer. The discrete scatterers are commonly modeled as uniformly distributed scatterers with densities of one 40-dBsm scatterer per square mile [56] for higher frequencies (X-band). Results described in Section 6.3 suggest discrete clutter distributions closer to 0.01 scatterers per square mile for the Mountaintop system and parameters at WSMR.

We now consider the relative amplitudes of the signals described by (2.1)–(2.3) using the Mountaintop system parameters in Table 2.1. An emitter with an ERP of 2 kW located at a range of 200 km will result in a received direct-path signal of –69 dBW (decibels-Watt) ignoring the specular in-plane multipath. The receiver thermal noise power is equal to  $kT_0BF_n$ , where  $k$  is Boltzmann's constant,  $T_0$  is the temperature,  $B$  is the receiver bandwidth, and  $F_n$  is the receiver noise figure. (At room temperature,  $kT_0 = 4 \times 10^{-21}$  W/Hz.) The resulting noise power is –143 dBW and hence the signal-to-noise ratio (SNR) for the direct path is 74 dB which is a very strong signal. Next consider an application of (2.2) to compute the power received from a 100-km<sup>2</sup> patch of ground. The average reflectivity observed at WSMR of –45 dB [6],[9] will be assumed. The RCS  $\sigma$  is equal to the product of the reflectivity,  $\sigma_0$ , and the area (80 dBm<sup>2</sup>) and is equal to 35 dBm<sup>2</sup>. If we assume the ranges  $R_t = R_r = 150$  km, then (2.3) yields a received power of –144.5 dBW for an SNR of –1.5 dB which is a weak signal. Next we consider scattering from a clutter discrete at the same range as the clutter patch. Discrete scatterers with cross sections as high as 60 dBm<sup>2</sup> have been observed [9], but we shall assume a more conservative level of 40 dBm<sup>2</sup>. Equation (2.3) yields a received power level of –139.5 dBW for an SNR of 3.5 dB which is also a weak signal. Signal integration techniques will be used to boost these signal-to-noise ratios to values that will be more useful. For example, if 1000 samples can be coherently integrated, then these ratios will be boosted by 30 dB (assuming an integration gain equal to the number of samples,  $N$ ).

## 2.4 LOCALIZATION OF A MOVING EMITTER

The remainder of this section contains a description of the bistatic delay and Doppler contours and the delay-Doppler locus or ridge that is observed in a multipath receive beam. The bistatic Hough transform is introduced as a technique for localizing an emitter under an idealized scattering scenario. This technique is useful because it provides insight by permitting a graphical interpretation to the localization process. More rigorous statistical formulations will be developed in Chapters 3 and 4.

### 2.4.1 Delay-Doppler Ridge

Differential delay and Doppler contours for a moving emitter and a stationary receiver are shown in Figure 2.3. The contours of constant Doppler are hyperbolas formed by the intersections of cones with the ground. We shall assume that the ground is flat. The cones are described by  $f = V/\lambda \cos \psi$ , where  $V$  is the emitter velocity,  $\lambda$  is the emitter wavelength, and  $\psi$  is the angle measured from the emitter direction vector. The contours of constant delay are intersections of ellipsoids with the ground. If both the receiver and the emitter are located on the ground, then the contours become ellipses with foci at their locations.

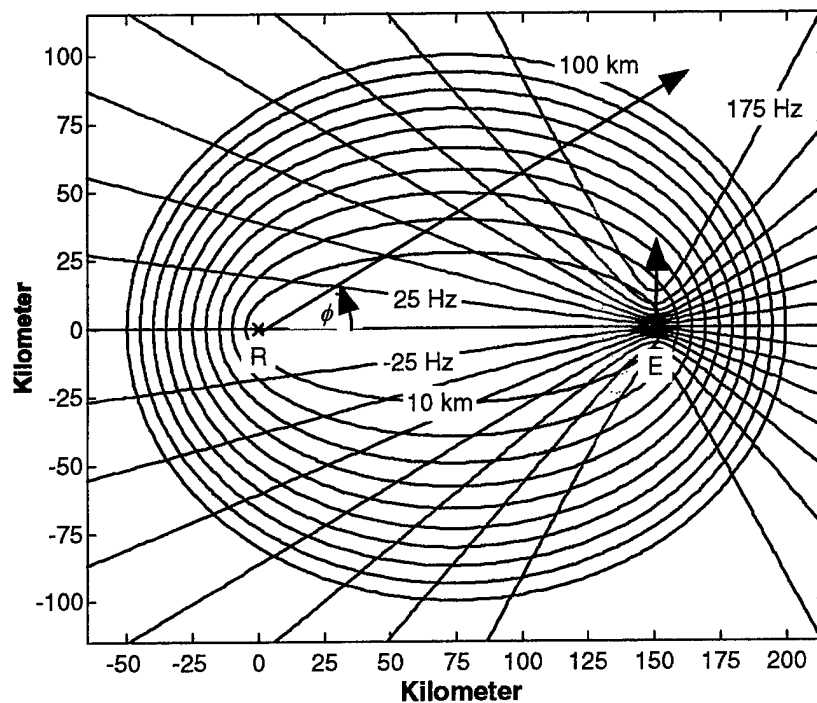


Figure 2.3. Bistatic delay and Doppler contours for an emitter at a range of 150 km traveling north at a velocity corresponding to a maximum Doppler shift of 200 Hz directly in front of the emitter and  $-200$  Hz behind the emitter. The Doppler shift for the direct-path signal is zero for this geometry and the heading is 90 degrees.

The receiver depicted in Figure 2.3 has formed a beam in the direction  $\phi$  which is 30 degrees. This beam is assumed to be very narrow and is shown in the figure as a line. The emitter signal scattered by the ground at each point along the line will be delayed and Doppler shifted by amounts indicated by the differential delay and Doppler contours. The energy in the scattered signal will be confined to a locus or ridge in delay-Doppler space as shown in Figure 2.4. The remainder of the scattered delay-Doppler intensity map will contain only receiver thermal noise. The differential Doppler ranges from zero Hz corresponding to the direct path, to a maximum of 200 Hz at a bistatic delay near 100 km. The ridge is shown as a line since the antenna beamwidth was assumed to be very narrow. These delay-Doppler ridges have been observed in practice [9] where the ridge was spread somewhat due to the nonzero antenna beamwidths. In the next section we use the bistatic Hough transform to localize an emitter by processing several scatterers on the delay-Doppler ridge.

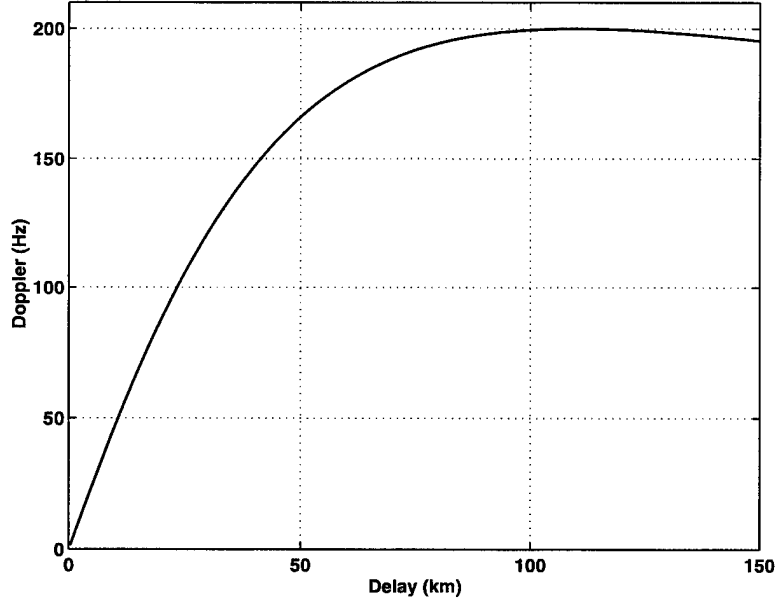


Figure 2.4. Delay-Doppler ridge for bistatic scattering from a moving emitter and the geometry of Figure 2.3.

### 2.4.2 Bistatic Hough Transform

In this section we derive the bistatic Hough transform. This is a numerical transform technique that is closely related to template matching [57] and the Radon transform [58]. It will be used to localize an emitter in an idealized scattering scenario and to provide insight into the localization using out-of-plane multipath process. It will also be useful as a tool for examining ambiguities that may occur when using out-of-plane multipath for emitter localization.

The Hough transform (HT) was introduced as a means to detect straight line segments in binary digital images [59]. It maps a spatially extended shape such as a line in image space to a point in parameter space. The first application of the HT for use in radar was considered in [60] where it was used to detect weak linear target tracks. In this section the HT will be used to detect the bistatic delay-Doppler ridge.

The Hough transform for line detection can be written in integral form as [61]

$$H(p, \theta) = \iint_{-\infty}^{\infty} I(x, y) \delta(p - x \cos \theta - y \sin \theta) dx dy, \quad (2.4)$$

where  $I(x, y)$  represents the image space and  $H(p, \theta)$  represents the parameter space. The impulse function is nonzero only when  $p = x \cos \theta + y \sin \theta$ . This expression is known as the normal parameterization of

a line. This parameterization is preferred over the more common parameterization,  $y = mx + b$ , because it avoids the numerical problems that can arise when dealing with vertical lines which have infinite slopes. For a binary image  $I(x, y)$  and the  $i^{\text{th}}$  pair of parameters  $(p_i, \theta_i)$ , the integral evaluates to the number of image points that coincide with the line  $p_i = x \cos \theta_i + y \sin \theta_i$ . For example, suppose  $I(x, y)$  is a 100 by 100 binary image consisting of a vertical line ( $\theta = \pi/2$ ) passing through the origin ( $p=0$ ). The Hough transform will contain a peak in parameter space of magnitude 100 located at  $(p, \theta) = (0, \pi/2)$  and some very small residual terms—mostly equal to one or zero at other values of  $(p, \theta)$ .

For the emitter localization problem, the image space is the delay-Doppler map and the parameter space contains the emitter parameters we want to estimate. A bistatic Hough transform designed to detect the delay-Doppler ridge contained in a bistatic delay-Doppler map can be written as

$$H(R, H, V) = \iint_{-\infty}^{\infty} M(D, f) \delta \left( R - \frac{D}{\left( \frac{\sin \gamma(H, V, f)}{\sin \alpha(H, V, f)} + \frac{\sin \phi}{\sin \alpha(H, V, f)} - 1 \right)} \right) dD df, \quad (2.5)$$

where:  $H(R, H, V)$  is the HT in parameters  $R, H, V$ ,

$M(D, f)$  is the bistatic delay-Doppler intensity map,

$D$  is the differential range delay,

$f$  is the differential Doppler shift (measured relative the direct path),

$R$  is the range from the receiver to the emitter,

$H$  is the emitter heading,

$V$  is the emitter velocity,

$\phi$  is the radar look azimuth,

$\gamma$  is the angle to the scatterer which is a function of  $D, H$ , and  $V$ , and

$\alpha$  is the remaining angle in the bistatic triangle which is shown in Figure 2.5.

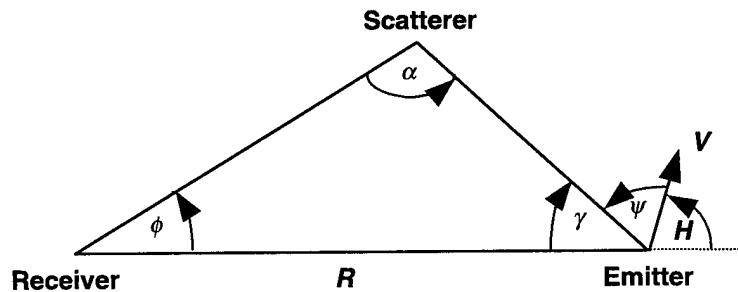


Figure 2.5. Bistatic triangle formed by the receiver, emitter, and scatterer.

The argument of the impulse function is taken from (1.2). This equation was derived using the law of sines to compute the emitter range using a single bistatic scatterer when the emitter velocity and heading is known. Here the emitter velocity and heading are parameters that will be treated as independent variables for the integration in (2.5). The integrand is non-zero only when the argument of the impulse function is equal to zero. To evaluate the integral, we solve for  $R$  as a function of the measured quantities of delay  $D$ , differential Doppler  $f$ , and radar azimuth  $\phi$ ; and the adjustable parameters of emitter velocity  $V$  and heading  $H$ . The angle  $\gamma$  is related to the emitter velocity, heading, and differential Doppler and can be determined as follows.

The direct-path absolute Doppler shift is

$$f_d = \frac{V}{\lambda} \cos(180 - H) , \quad (2.6)$$

and the scatterer absolute Doppler is

$$f_s = \frac{V}{\lambda} \cos(\psi) = \frac{V}{\lambda} \cos(180 - H - \gamma) . \quad (2.7)$$

The differential Doppler that is measured by the receiver is

$$f = f_s - f_d = \frac{V}{\lambda} [\cos(180 - H - \gamma) - \cos(180 - H)] , \quad (2.8)$$

but  $\cos(180 - H) = -\cos(H)$  and  $\cos(180 - H - \gamma) = -\cos(H + \gamma)$  , so

$$f = \frac{V}{\lambda} [-\cos(H + \gamma) + \cos(H)] . \quad (2.9)$$

Equation (2.9) can be used to determine  $\gamma$  since

$$\frac{V}{\lambda} \cos(H + \gamma) = \frac{V}{\lambda} \cos(H) - f , \quad (2.10)$$

and finally

$$\gamma = -H + \cos^{-1} \left( \cos(H) - \frac{f\lambda}{V} \right) , \quad (2.11)$$

and

$$\alpha = 180 - \phi - \gamma . \quad (2.12)$$

Using the above equations (2.5)–(2.12), we can describe the Hough transform algorithm with pseudo-code in Figure 2.6.

```

For each delay-Doppler cell  $M(D,f)$  containing scattered emitter energy
  For each trial emitter velocity parameter  $V$ 
    For each trial emitter heading  $H$ 
      calculate  $R$  (from argument of impulse function in (2.5))
      Accumulate counts in parameter space  $(R, H, V)$ 
    end
  end
end
Search parameter space  $(R,H,V)$  for peak.

```

*Figure 2.6. Pseudo-code for bistatic Hough transform localization algorithm.*

Localization using the Hough transform will now be demonstrated by an example. The emitter is located at a range of 150 km traveling with a heading of 90 degrees and a velocity of 140 m/s which corresponds to a maximum absolute Doppler shift of 200 Hz. We first assume that the emitter velocity is known. This restricts the parameter space to only two dimensions  $(R, H)$  thereby reducing the parameter search to only two dimensions.

Consider first a single scatterer located on the delay-Doppler ridge as shown in Figure 2.7(a). The Hough transform of this single point in delay-Doppler image space is a curved line in parameter space, which is shown in Figure 2.7(b). This result may be interpreted as follows: An emitter traveling at a known velocity cannot be localized using delay-Doppler information from a single scatterer; however, the information from the single scatterer confines the emitter parameters of range and heading to the curve in Figure 2.7(b). Transformation of additional scatterers in delay-Doppler space will result in additional curves in parameter space and the intersection of these curves yield the desired emitter parameters. This is illustrated in Figure 2.8 for three scatterers. The curves intersect at the correct emitter range of 150 km and heading of 90 degrees. This is somewhat similar to the intersecting hyperboloids discussed in Section 1.1.1.

When many scatterers are present, a sharp peak occurs in the parameter space. This is shown in Figure 2.9 for about 30 scatterers. The emitter parameters are estimated by searching the parameter space for the peak. For this example, the impulsive peak clearly identifies the correct emitter range of 150 km and bearing of 90 degrees.

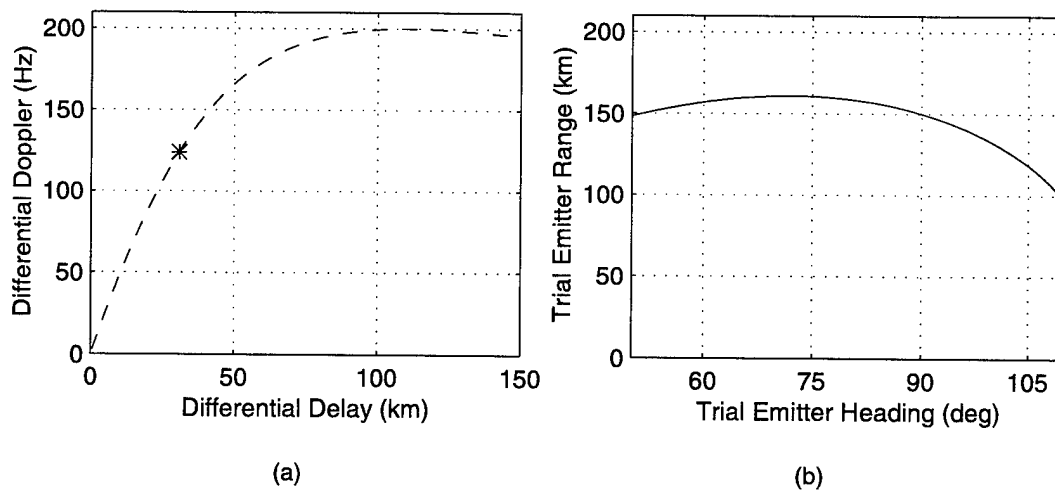


Figure 2.7. Hough transform of (a) point in delay-Doppler space is (b) a curve in the trial range-heading space.

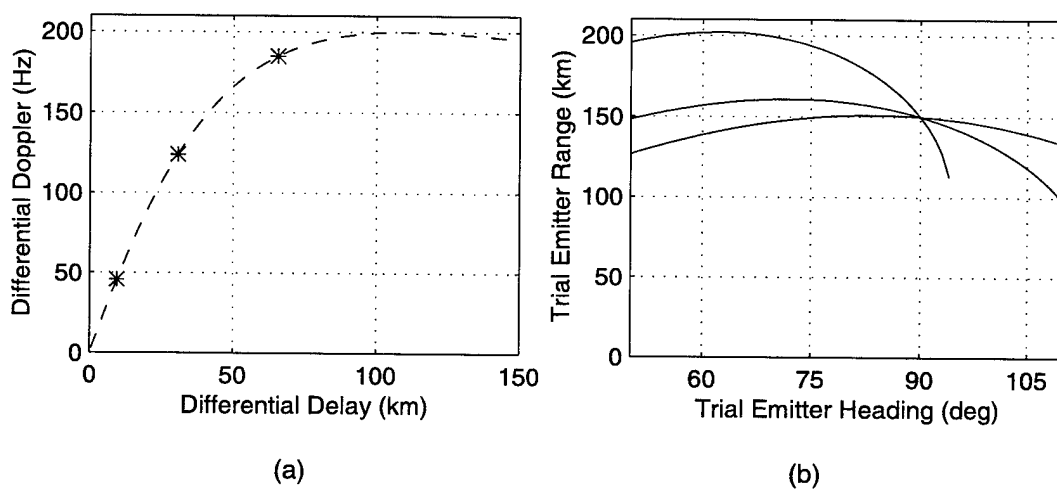


Figure 2.8. (a) Three scatterers located on the delay-Doppler locus and (b) the corresponding Hough transform.



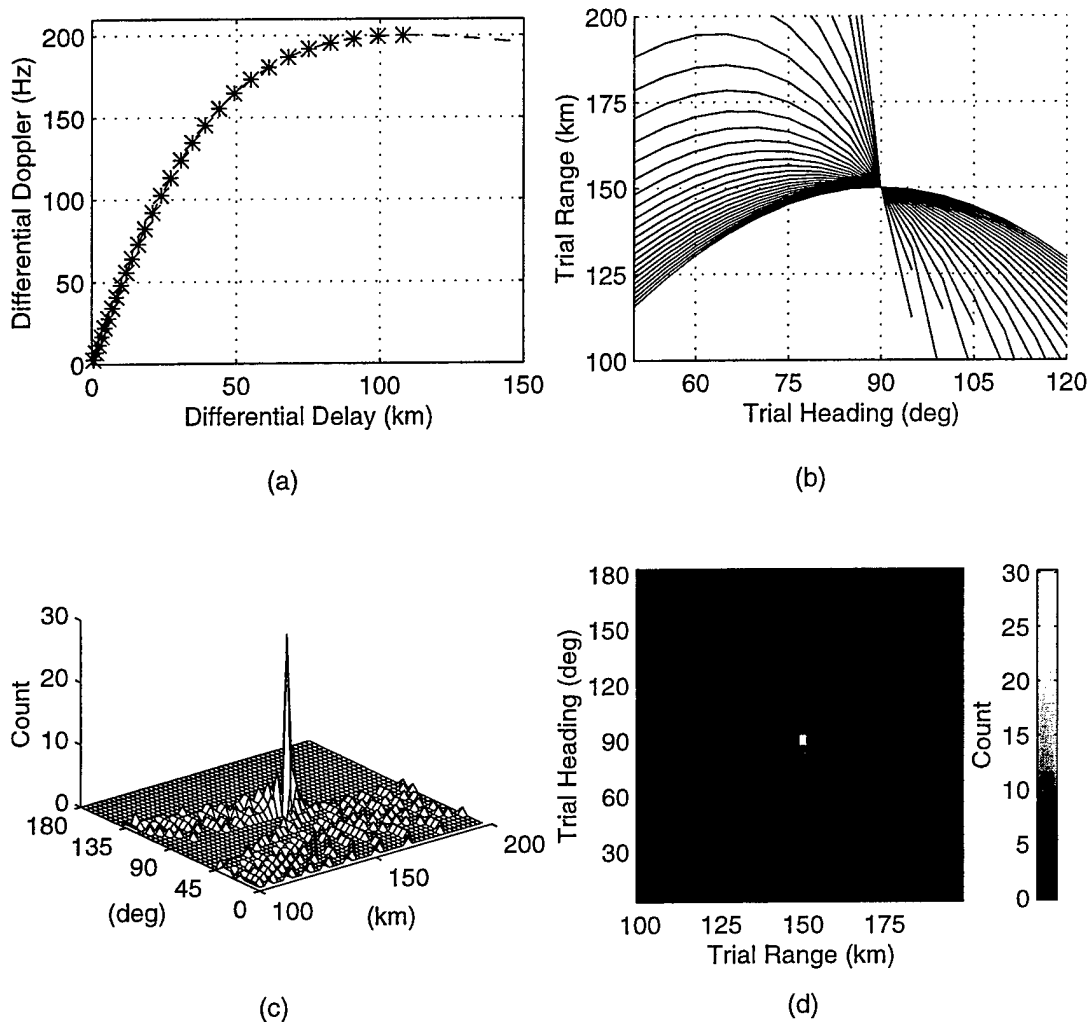


Figure 2.9. Localization using Hough transform. (a) Thirty scatterers on the delay-Doppler ridge are transformed to emitter parameter space (b, c, d). Parts (c) and (d) are views of the parameter space after the curves shown in (b) have been accumulated.

Figure 2.9(b) can be studied from a geometric dilution of precision (GDOP) point of view. GDOP is defined as the ratio of the RMS position errors, e.g., emitter range, and the measurement errors, e.g., differential delay (in km) [62]. A large GDOP means that small measurement errors will produce large parameter errors. For example, consider the HT of the two scatterers at the longest delay. This consists of the two most vertical lines in parameter space which are seen to be nearly parallel in Figure 2.9(b). While these lines intersect at the correct point in parameter space, it is easy to see that a small measurement error in image space resulting in the movement of one of these lines will produce a large error in the parameter space. Similarly, the HT of the two shortest delay scatterers are also parallel curves. However, if we consider the lines due to a short-delay scatter and a long delay scatterer, we can see that these are nearly perpendicular and thus small measurement errors will produce small parameter errors. The effects of measurement errors on parameter estimation errors will be examined in Chapter 5.

### 2.4.3 Uniqueness of Parameter Space Mapping

In the previous section an emitter was localized in the two dimensions of range and heading where the velocity was assumed to be known. The HT was used to perform the localization which generated a single, unambiguous result using only one beam of received scattering data. We now consider the case where all three parameters are unknown and show that multiple beams may be required to generate unique, unambiguous localization results.

The HT was determined for three trial emitter velocities corresponding to maximum Doppler shifts of 160, 200, and 240 Hz. The value of 200 Hz corresponds to the true emitter velocity. We expect a peak at the true velocity corresponding to 200 Hz and small residual terms for the two other trial velocities. The HT for the three cases is shown in Figure 2.10. We see that for the true velocity, the lines converge at a single point that will generate a sharp peak in parameter space. For the other two velocities, the lines do not converge as sharply, suggesting blurred or smeared peaks in parameter space. For this noise-free case, we can claim that the HT has successfully localized this emitter in three dimensions of range, heading, and velocity; however, if noise was present, the true peak could be blurred as well. Hence it may be difficult to select the correct emitter parameter set.

To see why peaks in parameter space occurred for three different parameter sets, we generate delay-Doppler ridges corresponding to each one. The false parameter sets are  $R=116$  km,  $H=76$  deg., and  $V=80\%$  of the true velocity, and are  $R=177$  km,  $H=99.5$  deg., and  $V=120\%$  of the true velocity. The delay-Doppler ridge for the three parameter sets are shown in Figure 2.11. We can see that the three ridges are nearly identical.

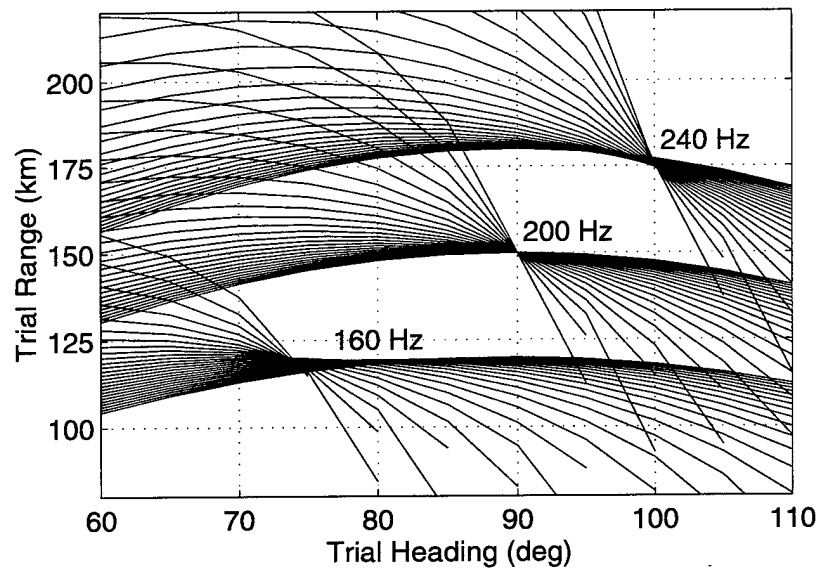


Figure 2.10. Hough transforms of a measured delay-Doppler ridge assuming three different emitter velocities.

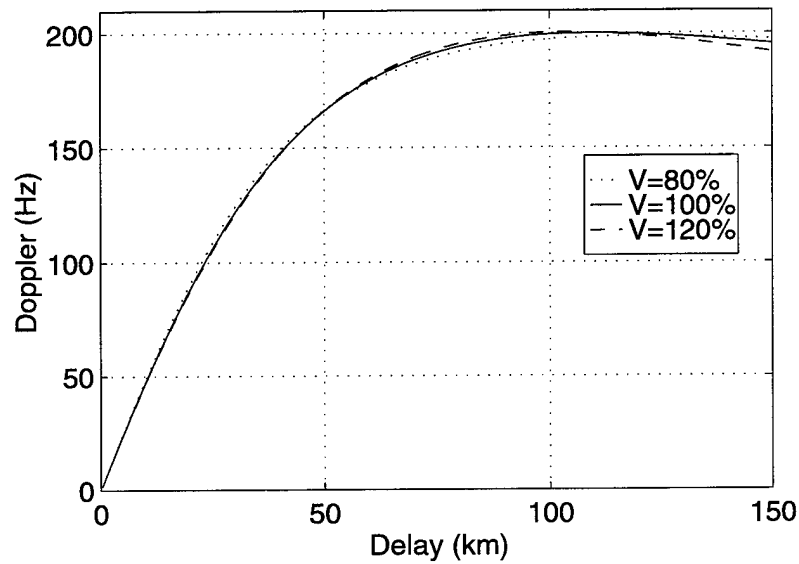


Figure 2.11. Delay-Doppler ridges for the three parameter sets suggested by Figure 2.10. The delay-Doppler ridges are nearly identical.

This result suggests that the localization of this emitter may be difficult because we have shown that three different parameter sets possess nearly identical delay-Doppler ridges. This is an important result because the localization technique relies on the uniqueness of the delay-Doppler ridge to estimate the emitter parameters. However, up to this point we have considered only the contributions from scattering in a single receive beam at 30 degrees. When additional beams are employed, the mismatch between the true parameters and the false peaks will be increased. For example, if we form an additional radar beam, say at  $-30$  degrees, we see in Figure 2.12 that the delay-Doppler ridges for these three parameter sets are no longer similar. Hence only the true peak will be enhanced by the additional beam and the localization result will be unique as expected.

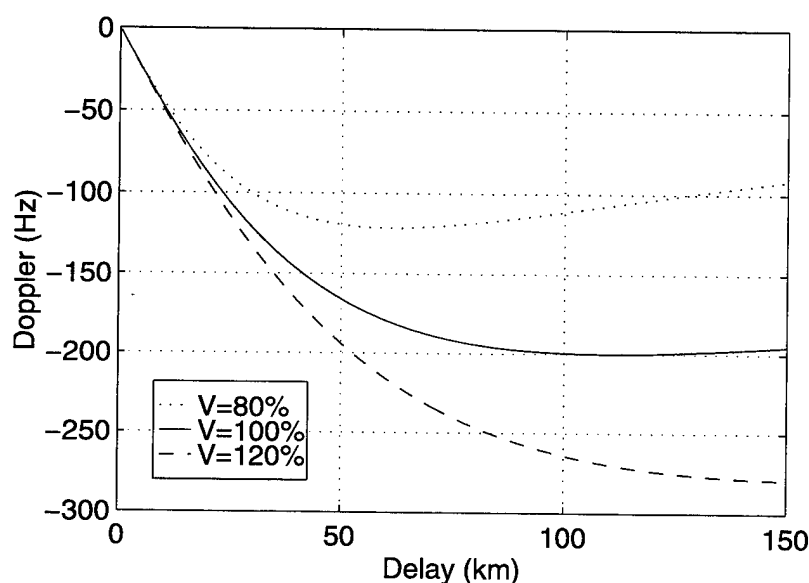


Figure 2.12. Delay-Doppler ridges for the three parameter sets and a  $-30$  degree receive azimuth.

## 2.5 CHAPTER SUMMARY

This section contains the background and introductory information required to develop the estimation techniques described in the following chapters. A discussion of signal and noise models and bistatic scattering is provided. The delay-Doppler ridge is described and the bistatic Hough transform is introduced and used to localize an emitter in an idealized case. This technique is graphical in nature and promotes a better understanding of the localization process. Statistically based solutions are provided in subsequent chapters. The HT is also shown to be useful as a tool for examining potential localization ambiguities. We used it to show that multiple receive beams may be required to perform emitter localization.

### 3. LOCALIZATION IN HOMOGENEOUS CLUTTER

#### 3.1 INTRODUCTION

In this chapter we design an estimator based on an assumption that the bistatic clutter is homogeneous. The homogeneous clutter model will be described along with several assumptions that lead to a simple statistical formulation. The likelihood function and corresponding maximum likelihood estimator (MLE) will be determined. The structure of the estimator is shown to be a time-varying FIR filter with Doppler modulators chosen to match the Doppler shifts in the multipath signals. The optimum solution technique will be described as well as a sub-optimum technique that employs weight thinning.

#### 3.2 BASIC SCATTERING MODEL

The fundamentals of bistatic scattering were introduced in Section 2.3. For the homogeneous scattering model assumption, the average received power for a delay-angle cell was written as

$$P_r = \iint_{\text{area}} \frac{P_t G_t G_r \lambda^2 \sigma_0}{(4\pi)^3 R_t^2 R_r^2} ds, \quad (2.2)$$

where the reflectivity  $\sigma_0$  does not vary much from cell to cell. This describes *area scattering* because the received power depends on the product of the reflectivity and the area of the delay-azimuth cell. This differs from *point scattering* which originates from a discrete scatter with RCS  $\sigma$ . For the homogeneous scattering assumption, we assume that the area scattering is stronger than the discrete scattering. In the following chapter, we treat the inhomogeneous case where we assume that point scattering is stronger than area scattering. These two assumptions are proposed because they permit fairly straightforward estimator designs. In practice, bistatic clutter will exhibit properties of both area and point scattering. The preferred estimator may therefore depend on the scattering characteristics of the specific terrain for any given scenario.

The bistatic reflectivity  $\sigma_0$  in (2.2) is generally a function of the incidence angles and the out-of-plane angle. In the out-of-plane region the simplest bistatic clutter models are based on the constant-gamma model for monostatic clutter [63]

$$\sigma_0^M = \gamma \sin \theta_i, \quad (3.1)$$

where  $\sigma_0^M$  is the monostatic cross section per unit area,  $\theta_i$  is the incidence angle, and  $\gamma$  is an additional scattering parameter that is assumed to be independent of  $\theta_i$ . This may be generalized for bistatic scattering [63] as

$$\sigma_0 = \gamma (\sin \theta_r \sin \theta_i)^{1/2}, \quad (3.2)$$

where  $\theta_r$  and  $\theta_t$  are the receiver incidence angle and transmitter incidence angle, respectively. Values of the reflectivity parameter  $\gamma$  were found to be approximately -20 dB for the Mountaintop system at WSMR [9].

### 3.3 STATISTICAL FORMULATION

The statistical formulation begins with a statement of the clutter model and ends with the likelihood function. In order to write the likelihood function, several further simplifications and approximations are required.

We shall assume that the antenna beamwidth is very narrow and the delay cells are closely spaced. This helps to justify the further assumption that the scattering from each delay-azimuth cell originates from the center of the cell. This permits us to ignore Doppler dispersion (broadening) and is illustrated in the delay-Doppler map shown in Figure 3.1 where the scattering centers in the multipath beam are denoted by dots. The significance of this assumption is that it permits us to treat the differential delay and azimuth for each scattering cell as independent variables. The delay is simply the center of each delay bin while the azimuth is the look direction of the beam. (For the inhomogeneous scattering model described in the next section, this assumption will not be valid. There we will be required to estimate the delay and azimuth for each discrete scatterer separately.)

The very high signal-to-noise ratio of the emitter waveform via the direct propagation path permits additional simplifications. In Section 2.3.1 we saw that the SNR of the direct path was approximately 74 dB for the typical Mountaintop system parameters. The direct-path signal is measured by the reference beam which is pointed directly at the emitter. The SNR of the emitter signal that was scattered by a 100-km<sup>2</sup> patch of ground was approximately -1.5 dB per pulse. The very high SNR for the emitter signal via the direct path facilitates a very accurate sampling of the emitter signal. For the purposes of this section, we will consider this signal to be known exactly. Furthermore, the very high emitter SNR facilitates emitter azimuth estimates that are very accurate. Again, for the purposes of this section, we will assume that azimuth of the emitter is known exactly.

With the above assumptions and simplifications, we are ready to write an expression for the received signal in the multipath beam. We write

$$z_b(n) = \sum_{p=1}^P a_{bp} s(n - D_p) e^{j\omega_{bp}(n - D_p)} + g_b(n) \quad b = 1, 2, 3, \dots, B, \quad (3.3)$$

where  $z_b(n)$  is the  $n^{\text{th}}$  sample from the  $b^{\text{th}}$  beam,  $a_{bp}$  and  $\omega_{bp}$ , respectively, represent the complex amplitude and Doppler frequency in radians per second of the  $p^{\text{th}}$  independent scattering cell for the  $b^{\text{th}}$  independent beam. The differential delay  $D_p$  here is an integer equal to  $p-1$ . The emitter waveform is  $s(n)$  and the zero-mean complex observation noise is denoted by  $g_b(n)$  with covariance matrix  $\mathbf{R}_{gg}$ . The dimension of  $\mathbf{R}_{gg}$  is  $N$  by  $N$  where  $N$  is the total number of samples in the data vector  $\mathbf{z}_b$ . In general, the noise term  $g_b(n)$  contains anything not included in the summation term representing the multipath model. For example, scattered signals that enter via the antenna sidelobes, distant scatter from beyond the

summation length, additional emitter signals, etc., are all included in the noise term. These noise sources are referred to as model noise because they are unwanted signal sources not described by the model. For our purposes in this section, we shall assume that the noise is receiver thermal noise which is white and uncorrelated from beam-to-beam and from sample-to-sample.

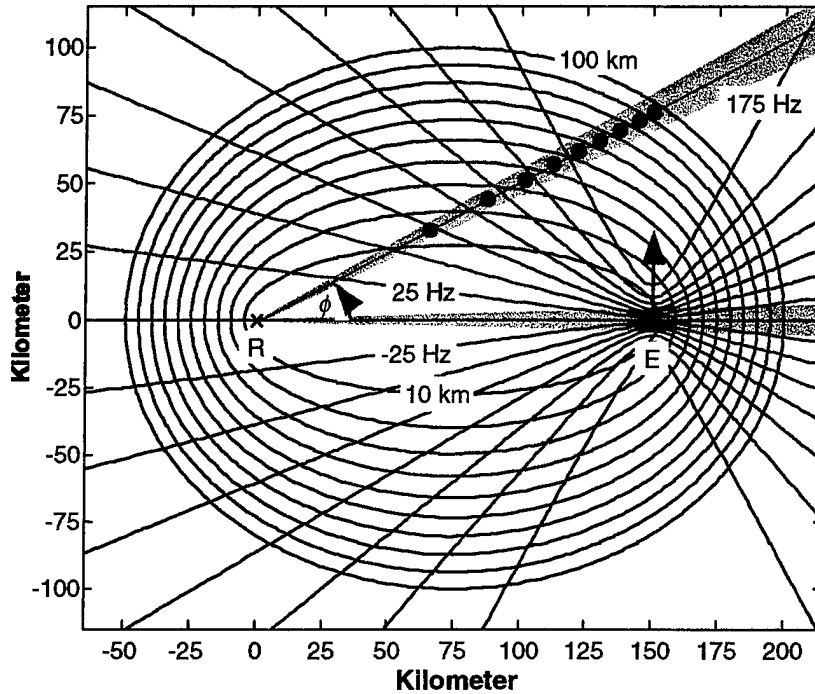


Figure 3.1. Range and Doppler contours for a moving emitter. A reference beam pointed at the emitter directly samples the emitter waveform and a multipath beam collects the attenuated, delayed, and Doppler shifted replicas of the emitter waveform.

We can write (3.3) in vector form as

$$\mathbf{z}_b = \mathbf{m}_b + \mathbf{g}_b, \quad (3.4)$$

where each term is an  $N$  by 1 vector and  $m_b(n)$  is

$$m_b(n) = \sum_{p=1}^P a_{bp} s(n - D_p) e^{j\omega_{bp}(n - D_p)} \quad b = 1, 2, 3, \dots, B. \quad (3.5)$$

That is,  $\mathbf{z}_b$  is equal to  $\mathbf{m}_b$  when the measurement noise  $\mathbf{g}_b$  is equal to zero. The probability density function for the measurements  $z_b(n)$  can be written as a complex Gaussian

$$f_{\mathbf{z}_b}(\mathbf{z}_b) = \left( \frac{1}{\pi^N |\mathbf{R}|} \right) e^{-(\mathbf{z}_b - \mathbf{m}_b)^H \mathbf{R}^{-1} (\mathbf{z}_b - \mathbf{m}_b)} \quad (3.6)$$

for a single beam, and as

$$f_{\mathbf{z}}(\mathbf{z}) = \prod_{b=1}^B \left( \frac{1}{\pi^N |\mathbf{R}|} \right) e^{-(\mathbf{z}_b - \mathbf{m}_b)^H \mathbf{R}^{-1} (\mathbf{z}_b - \mathbf{m}_b)} \quad (3.7)$$

or

$$f_{\mathbf{z}}(\mathbf{z}) = \left( \frac{1}{\pi^{BN} |\mathbf{R}|^B} \right) e^{-\sum_{b=1}^B (\mathbf{z}_b - \mathbf{m}_b)^H \mathbf{R}^{-1} (\mathbf{z}_b - \mathbf{m}_b)} \quad (3.8)$$

for multiple beams where we have assumed that the covariance matrix of the noise,  $\mathbf{R}$ , is the same for each beam. (The  $gg$  subscript in  $\mathbf{R}_{gg}$  has been dropped for convenience.) For the white thermal noise assumption,  $\mathbf{R}$  is of the form  $\mathbf{I}\sigma^2$ , and we can write the PDF of the measured vector for a given beam (3.6) as

$$f_{\mathbf{z}}(\mathbf{z}|\boldsymbol{\theta}) = \left( \frac{1}{\pi^N \sigma^{2N}} \right) e^{-(\mathbf{z} - \mathbf{m}(\boldsymbol{\theta}))^H (\mathbf{z} - \mathbf{m}(\boldsymbol{\theta})) / \sigma^2}, \quad (3.9)$$

where we have dropped the beam subscripts. This may also be written as

$$f_{\mathbf{z}}(\mathbf{z}|\boldsymbol{\theta}) = \left( \frac{1}{\pi^N \sigma^{2N}} \right) e^{-|\mathbf{z} - \mathbf{m}(\boldsymbol{\theta})|^2 / \sigma^2}, \quad (3.10)$$

where  $|\cdot|$  denotes the vector norm. The term  $\mathbf{m}(\boldsymbol{\theta})$  is the  $N \times 1$  vector whose elements for a given beam are given in (3.5) by setting  $n = 1, 2, \dots, N$ . The parameter vector  $\boldsymbol{\theta}$  has been included to remind the reader that this vector is a function of the emitter parameters we want to estimate. Conditional joint probability or likelihood functions of the form of (3.9) or (3.10) will be assumed throughout the rest of this chapter. Note that these are conditional joint probability functions when the parameters  $\boldsymbol{\theta}$  are fixed and the observation vector  $\mathbf{z}$  is variable, and these are likelihood functions when the observation vector  $\mathbf{z}$  is fixed and parameters  $\boldsymbol{\theta}$  are variable. The nature of the dependence of  $f_{\mathbf{z}}(\mathbf{z}|\boldsymbol{\theta})$  on  $\boldsymbol{\theta}$  is in

$$m(n) = \sum_{p=1}^P a_p s(n - D_p) e^{j\omega_p(\boldsymbol{\theta})(n - D_p)}, \quad (3.11)$$

where the only term that depends on  $\boldsymbol{\theta}$  is  $\omega_p(\boldsymbol{\theta})$ , the Doppler frequency shift for each scattering cell. That is a direct consequence of the homogeneous clutter assumption which, as mentioned above, permits us to



treat azimuth and time delay as independent variables. We still need to estimate the complex amplitude,  $a_p$ , for each scattering cell. The scatterer amplitudes are nuisance parameters.

### 3.4 MAXIMUM LIKELIHOOD ESTIMATOR

In this section we determine the maximum likelihood estimator (MLE) of the parameter vector  $\theta$ , based on the model described above. The MLE produces the *most plausible* estimate vector  $\theta$  given a measurement vector  $\mathbf{z}$  by maximizing the likelihood function (3.10). Maximizing this function is equivalent to minimizing the exponent

$$|\mathbf{z} - \mathbf{m}(\theta)|^2 = |\mathbf{g}|^2, \quad (3.12)$$

where the vector  $\mathbf{m}(\theta)$  is the system model from (3.4) and (3.11) and  $\mathbf{z}$  is the measured data vector. The difference between these two terms is the observation error,  $\mathbf{g}$ . We desire to determine the parameter vector  $\theta$ , as well as the scatterer weights  $a_p$ , that yield the minimum error. We will be required to search the parameter space while estimating the nuisance parameters  $a_p$  for the minimum squared error. The parameter set that minimizes the squared error will be chosen as the localization estimate.

We first treat the case where the Doppler terms  $\omega_p$  are zero and then extend the results to handle nonzero case. When the Doppler terms are zero, (3.5) becomes

$$m(n) = \sum_{p=1}^P a_p s(n - D_p). \quad (3.13)$$

Hence this problem reduces to the standard system identification problem [64] depicted in Figure 3.2. The multipath channel is modeled by a discrete-time linear, time-invariant FIR filter with filter coefficients  $a_p$ . The input is the emitter waveform  $s(n)$ , the output of the noisy multipath channel is  $z(n)$ , and the system identification filter output is  $m(n)$ .

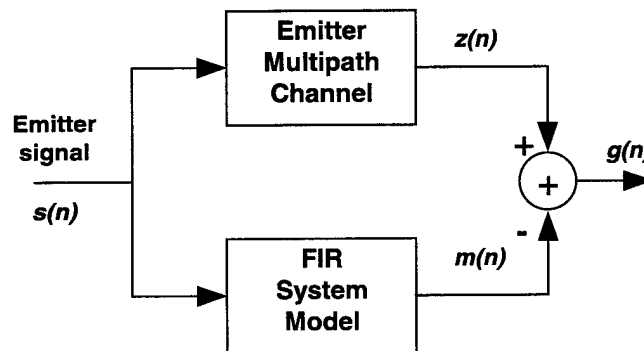


Figure 3.2. Finite impulse response (FIR) model for system identification.

The optimum filter coefficients  $a_p$  (in a least-squares sense) minimize the sum of the square error sequence  $g(n)$ ,

$$\begin{aligned} J &= \sum_{n=P}^N |g(n)|^2 \\ &= \sum_{n=P}^N \left| z(n) - \sum_{p=1}^P a_p s(n - D_p) \right|^2. \end{aligned} \quad (3.14)$$

The summation over  $n$  starts at  $P$  to assure that all the  $P$  filter coefficients have nonzero input data values. To determine the filter coefficients that minimize  $J$ , we differentiate (3.14) with respect to the real and imaginary parts of each filter coefficient  $a_p$  and set the result equal to zero. The optimum filter coefficients are the solutions to

$$\sum_{n=P}^N s^*(n - D_p) g_{\min}(n) = 0, \quad p = 1, 2, \dots, P, \quad (3.15)$$

which is the temporal version of the *principle of orthogonality*. The expression on the left side of (3.15) represents the time average of the cross-correlation between the  $p^{\text{th}}$  tap input  $s(n - D_p)$  and the minimum estimation error  $g_{\min}(n)$  over all values of the time index  $n$  in the interval  $(P, N)$ . The principle of orthogonality states that when the filter coefficients are selected to minimize  $J$ , then the minimum error series  $\{g_{\min}(n)\}$  is orthogonal to input time series  $\{s(n - D_p)\}$  to the  $p^{\text{th}}$  coefficient of the filter of length  $P$ . A good description of the least-squares problem can be found in [65].

To make use of this result, we rewrite (3.3) as

$$g(n) = z(n) - \sum_{p=1}^P a_p s(n - D_p) \quad (3.16)$$

and substitute for  $g(n)$  into (3.15) to yield

$$\sum_{n=P}^N s^*(n - D_k) \left( z(n) - \sum_{p=1}^P a_p s(n - D_p) \right) = 0, \quad k = 1, 2, \dots, P. \quad (3.17)$$

Expanding and rearranging terms yields

$$\sum_{p=1}^P a_p \sum_{n=P}^N s^*(n - D_k) s(n - D_p) = \sum_{n=P}^N s^*(n - D_k) z(n), \quad k = 1, 2, \dots, P, \quad (3.18)$$

where the inner sum on the left is the time-average autocorrelation function of the filter input for lag  $D_p - D_k$  and the sum on the right is the time-average cross-correlation function for lag  $D_k$ . In matrix form, we can write (3.18) as

$$\mathbf{R}_{ss} \mathbf{a} = \mathbf{r}_{sz} \quad (3.19)$$

with solution for the optimum weight vector given by

$$\mathbf{a} = \mathbf{R}_{ss}^{-1} \mathbf{r}_{sz}, \quad (3.20)$$

which is the well-known result. We can compute  $\mathbf{R}_{ss}$  and  $\mathbf{r}_{sz}$  using the  $(N-P+1)$  by  $P$  data matrix

$$\mathbf{S} = \begin{bmatrix} s(P) & s(P-1) & \cdots & s(2) & s(1) \\ & s(P) & \cdots & \cdots & s(2) \\ \vdots & \vdots & \vdots & \vdots & \vdots \\ s(N-1) & s(N-2) & \cdots & & \vdots \\ s(N) & s(N-1) & \cdots & \cdots & s(N-P+1) \end{bmatrix} \quad (3.21)$$

as  $\mathbf{R}_{ss} = \mathbf{S}^H \mathbf{S}$ ,  $\mathbf{r}_{sz} = \mathbf{S}^H \mathbf{z}$ , and  $\mathbf{a} = (\mathbf{S}^H \mathbf{S})^{-1} \mathbf{S}^H \mathbf{z}$ . We select  $(N-P+1) > P$  so that  $\mathbf{S}^H \mathbf{S}$  is invertible.

The above development generated the weight vector  $\mathbf{a}$  that minimized the exponent of the likelihood function derived for Gaussian noise. Hence these are maximum likelihood weights. If the distribution of the observation noise was non-Gaussian, then these weights are optimum in the least-square sense.

How can the above results be extended to handle the time-varying filter suggested by (3.3)? To solve the general time-varying case, we replace

$$s(n - D_p) \text{ by } s(n - D_p) e^{j\omega_p(n - D_p)} \quad (3.22)$$

in (3.15)–(3.21). Thus we have added the differential Doppler term which contains the information necessary to estimate the parameter vector  $\boldsymbol{\theta}$  since  $\omega$  is a function of  $\boldsymbol{\theta}$ . The actual estimation process will require a search over all possible values of  $\boldsymbol{\theta}$  in parameter space.

When we perform the substitution of (3.22), Equation (3.17) becomes

$$\sum_{n=P}^N s^*(n - D_k) e^{-j\omega_k(n - D_k)} \left( z(n) - \sum_{p=1}^P a_p s(n - D_p) e^{j\omega_p(n - D_p)} \right) = 0, \quad k = 1, 2, \dots, P, \quad (3.23)$$

and (3.18) becomes

$$\begin{aligned} & \sum_{p=1}^P a_p \sum_{n=P}^N s^*(n - D_k) e^{-j\omega_k(n - D_k)} s(n - D_p) e^{j\omega_p(n - D_p)} \\ & = \sum_{n=P}^N s^*(n - D_k) e^{-j\omega_k(n - D_k)} z(n) \quad k=1, 2, \dots, P. \end{aligned} \quad (3.24)$$

Thus the individual terms in the autocorrelation function become

$$R_{ss}(k, p) = \sum_{n=P}^N s^*(n - D_k) e^{-j\omega_k(n - D_k)} s(n - D_p) e^{j\omega_p(n - D_p)}, \quad k = 1, 2, \dots, P, \quad p = 1, 2, \dots, P \quad (3.25)$$

and

$$r_{sz}(k) = \sum_{n=P}^N s^*(n - D_k) e^{-j\omega_k(n - D_k)} z(n), \quad k = 1, 2, \dots, P, \quad (3.26)$$

and finally, the optimum weights

$$\mathbf{a} = \hat{\mathbf{R}}_{ss}^{-1} \mathbf{r}_{sz}. \quad (3.27)$$

The structure of this estimator is the time-varying, FIR tapped delay line filter that is illustrated in Figure 3.3. The vector  $\mathbf{a}$  represents the complex filter coefficients or taps of the filter. The differential Doppler terms  $\omega_p$  are shown modulating the delayed replicas of the emitter waveform. A separate Doppler modulator  $\omega_p$  is employed for each tap  $a_p$ .

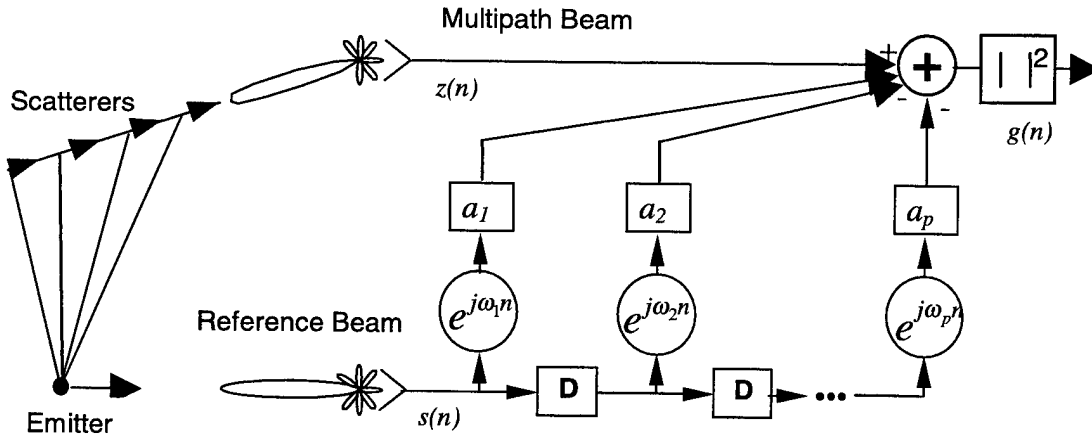


Figure 3.3. Emitter localization filter structure for a single multipath beam. The emitter parameter set that minimizes the output power is the ML estimate.

Note that we are not trying to estimate the Doppler terms  $\omega_p$  directly. Instead, we are computing a deterministic set of modulators  $\omega$  for each trial parameter set  $\theta$ . We then compute the optimum weights  $\mathbf{a}$  for the deterministic modulators and evaluate the error given by (3.14). Since the Doppler modulators will contain some mismatch for all cases except when the trial emitter parameters equal the true emitter

parameters, the error can be large even though the weights are “optimum.” When the trial emitter parameters equal the true parameters, the error is minimized. The minimum error maximizes likelihood function in (3.10) and is hence the maximum likelihood estimator for the emitter parameters  $\theta=(R,H,V)$ .

In Section 2.4.3 we saw that multiple beams may be required to resolve potential ambiguities. The MLE described above can be easily extended for multiple beams as shown in Figure 3.4. This architecture assumes that the individual multipath beams are uncorrelated (i.e., the beams are

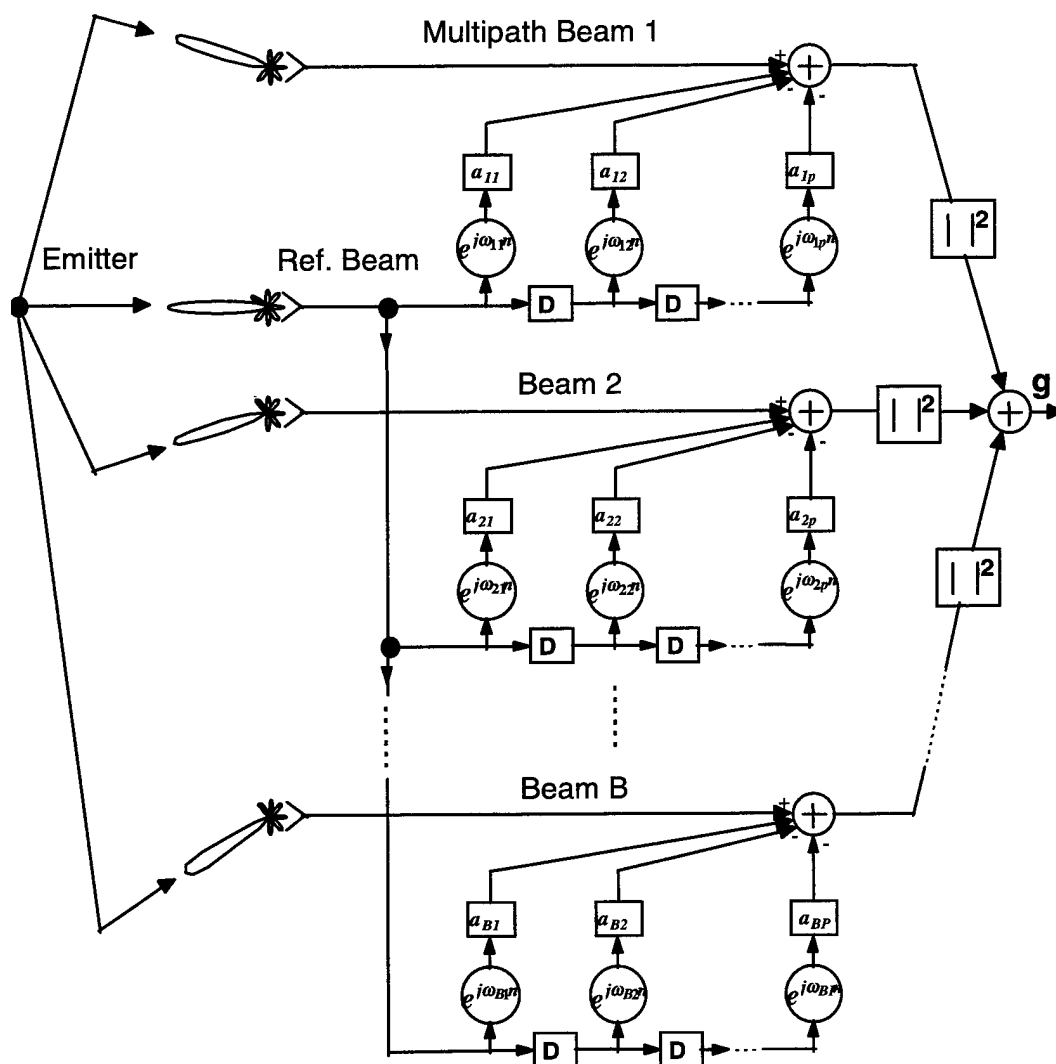


Figure 3.4. Emitter localization filter for multiple beams. The emitter parameter set that minimizes the output power is the ML estimate.

orthogonal). Thus we will be required to solve  $B$  smaller problems of size  $P$  instead of the larger problem of size  $B \times P$ , where  $B$  is the number of beams and  $P$  is the number of taps.

The single beam structure of Figure 3.3 has been used in the past [9] for jammer multipath mitigation where the Doppler modulators were used to improve mitigation performance. There the error vector was the target beam with the emitter multipath energy removed. It is re-introduced here as the MLE for emitter localization. The fundamental difference is that in [9] the Doppler modulators were estimated independently and used to improve jammer multipath mitigation performance. For localization, the modulators are computed separately for each parameter set and the set with the lowest error (corresponding to the best mitigation) is selected as the MLE. Thus we see that jammer multipath mitigation and emitter localization are very closely related.

The only thing left to specify in this estimator is how to compute the Doppler modulators. These are given by

$$\omega_p(R, H, V) = \frac{2\pi V}{\lambda} \left[ \cos H - \cos \left( H + \sin^{-1} \left( \frac{(D_p^2 + 2RD_p) \sin \phi}{D_p^2 + 2(R^2 + RD_p)(1 - \cos \phi)} \right) \right) \right], \quad (3.28)$$

which is a function of the emitter parameters  $(R, H, V)$ , the differential delay for each filter tap  $D_p$ , the angle of the multipath beam  $\phi$ , and the emitter wavelength  $\lambda$ . This was derived based on a two-dimensional approximation that ignores the altitude of the emitter: the details are contained in Appendix A. An expression based on a three-dimensional approximation is derived in Appendix B and the exact three-dimensional solution is contained in Appendix C.

### 3.5 SOLUTION TECHNIQUE

The fundamental method of solution is the dense multidimensional search over the emitter parameter space. Hence we are solving this inverse problem by solving an “infinite” number of forward solutions and selecting the one that maximizes the likelihood function. Such dense searches are very costly especially for three or four dimensions. In practice, we shall first perform a coarse three-dimensional search over emitter range, heading, and velocity. The peak of the coarse search is used as the starting point for an iterative procedure, such as the Newton-Raphson method. The iterative procedure is carried out in all four dimensions of range, heading, velocity, and altitude. Generally, if the starting point is close to the global maximum, the iteration will converge to it [67]. Thus, the initial coarse search must be sufficiently fine to assure that the iterative procedure does not converge to a local maximum.

#### 3.5.1 Sub-optimal Technique

The coarse parameter search and iterative procedure described above can be computationally expensive for long filter lengths. If the filter is of length  $P$ , each step in the parameter search will require the estimation and inversion of a  $P$  by  $P$  covariance matrix. The computational cost in terms of complex

multiplications is on the order of  $P^3$ . Thus anything that can be done to reduce  $P$  will result in substantial computational savings.

One method to reduce the effective filter size is weight pruning [66]. This is a process whereby only the largest weights in the filter are included in the matrix inversion and subsequent computations. The basic idea is to include the taps which correspond to strong scattering while neglecting the taps corresponding to weak scattering. To determine which taps to include, one would apply (3.20) without any Doppler terms to a very short sequence of multipath data and retain some number of the largest taps. For data sequences on the order of 1-3 ms, the data may be considered stationary since the differential Doppler frequencies are relatively small. The relative amplitude of the taps obtained in this manner will be close to the amplitude of the taps in the full configuration when the correct Doppler terms are applied to the filter. If the number of taps can be reduced from, for example, 100 to 10, the computation savings will be on the order of  $10^3$ , which is considerable.

### **3.6 CHAPTER SUMMARY**

This chapter contains the design of the ML estimator based on an assumption that the bistatic clutter is homogeneous. The structure of the estimator was shown to be a time-varying FIR filter with Doppler modulators to match the Doppler shifts in the multipath signals. The performance of this estimator will be studied in Chapter 5. The optimum solution requires a dense multidimensional search over emitter parameter space. A sub-optimum technique that employs weight thinning has been suggested. This technique retains only the taps corresponding to the strongest scattering cells. This concept leads naturally to the estimator based on an inhomogeneous clutter model that will be described in the next chapter.

## 4. LOCALIZATION IN INHOMOGENEOUS CLUTTER

### 4.1 INTRODUCTION

In this chapter an estimator is designed that is based on the assumption that the bistatic clutter is inhomogeneous and dominated by a number of discrete scatterers. This is a two-part estimation procedure. The receiver first measures the scattering parameters of relative time delay,  $D$ , differential Doppler,  $f$ , azimuth,  $\phi$ , and amplitude,  $a$ , for some or all the dominant discrete scattering points. The scattering parameter estimates are then used to estimate the emitter parameters through a set of nonlinear bistatic localization equations. These nonlinear equations are linearized using a truncated Taylor series expansion that retains only the terms less than second order. This permits the use of linear estimation techniques such as *best linear unbiased estimator* (BLUE) [67]. This estimator will be shown to be the MLE when the observation noise is Gaussian. As with the estimator in the previous chapter, application of this estimator requires a coarse search followed by an iterative procedure.

### 4.2 BASIC MODEL FOR INHOMOGENEOUS SCATTERING

The fundamentals of bistatic scattering were introduced in Section 2.3 and a homogeneous clutter model was described in Section 3.2. We consider in this section a clutter model that is inhomogeneous. This model assumes that the bistatic clutter is dominated by a number of discrete scatterers, and that the emitter multipath signals are primarily due to these scatterers. The received power for a discrete scatterer was given as

$$P_r = \frac{P_t G_t G_r \lambda^2 \sigma}{(4\pi)^3 R_t^2 R_r^2} , \quad (2.3)$$

where  $\sigma$  is the RCS of the point scatterer. Sources for discrete scattering can be man-made, such as water towers, buildings, etc., or natural terrain features, such as mountains, cliffs, etc. An example of a discrete scattering scenario is shown in Figure 4.1.

The RCS of the discrete scatterers varies from scatterer to scatterer with small scatterers being more frequent than large scatterers. A model commonly used for higher frequencies is shown in Table 4.1 [56]. The densities in this table are higher than those observed by the Mountaintop system at WSMR, where the density is closer to 0.026 40-dBm<sup>2</sup> scatterers per square kilometer.



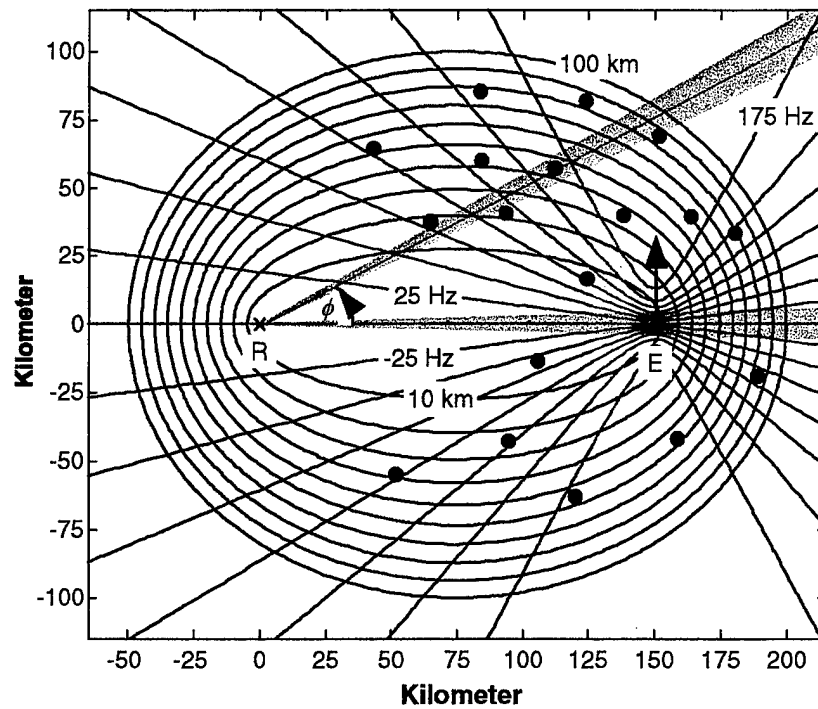


Figure 4.1. Range and Doppler contours for a moving emitter. A reference beam pointed at the emitter directly samples the emitter waveform, and multipath beams collect attenuated, delayed, and Doppler-shifted replicas scattered by the discrete scatterers.

TABLE 4.1  
Discrete Clutter Model [56]

Radar cross section	Density, per square kilometer
60 dBm <sup>2</sup>	0.026
50 dBm <sup>2</sup>	0.26
40 dBm <sup>2</sup>	2.6

### 4.3 STATISTICAL FORMULATION

The statistical formulation and design of the estimator consists of two parts. The first part consists of estimating the parameters of relative time delay,  $D$ , differential Doppler,  $\omega$ , azimuth,  $\phi$ , and amplitude,  $a$ , for a given number of dominant scatterers. This is described in Section 4.3.1 below. The second part consists of using the scattering parameters to estimate the emitter parameters of range,  $R$ , heading,  $H$ , velocity,  $V$ , and altitude,  $A$ . This will be described in Section 4.3.2.

#### 4.3.1 Part 1: Estimation of Scattering Parameters

Each discrete scatterer that reflects the emitter signal is described by four parameters that must be estimated. The necessary parameters are scatterer delay, Doppler, azimuth, and amplitude which, for the  $i^{\text{th}}$  scatterer, are written as  $[D_i, \omega_i, \phi_i, a_i]$ .

An estimator based on cross-correlation is shown in Figure 4.2 for a single scatterer. This structure is the maximum likelihood estimator for narrowband signals where both the signal and the additive noise are white. We search over the *independent* parameters of  $[D, \omega, \phi]$  for the maximum cross-correlation  $|R_{sz}|$ . The joint estimation of differential time delay and differential Doppler shift was shown to be uncorrelated in [43] when the observation time is sufficiently long and the signal-to-noise ratios are sufficiently high. Under these assumptions the joint estimator is efficient in the sense that it is unbiased and achieves the Cramer-Rao lower bound. We assume that these conditions hold here. The amplitude estimate,  $a$ , can be derived from the cross-correlation,  $r_{sz}$ , as  $a_i = r_{sz}(i) / r_{ss}(0)$ .

If there are  $P$  scatterers in the data, there will be  $P$  peaks in the delay-Doppler-azimuth space covered by the estimator. We choose the parameters at these peaks to be our scatterer estimates. To simplify the analysis of the scatterer estimates, we assume that each scatterer can be treated as a separate estimation problem with no interaction between neighboring scatterers. This may be justified somewhat by the fact that there are three factors working to decorrelate the scattered signals: delay, Doppler, and azimuth.

With the above assumptions, the variances of the scatterer parameter estimates for this estimator are taken directly from the Cramer-Rao lower bounds (CRLB) for point targets. We are assuming that discrete scatterers have the same bounds as conventional radar point targets. The CRLB for delay, Doppler, angle, and amplitude will be given in Chapter 5.

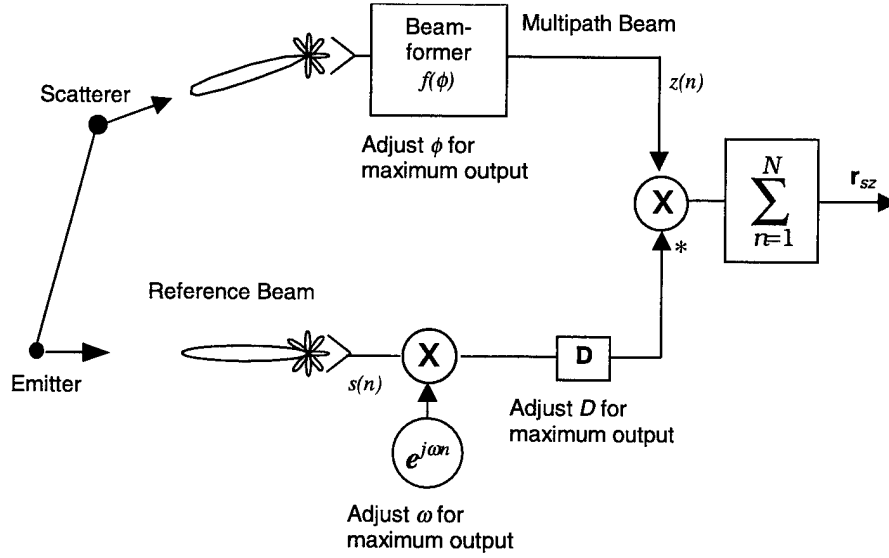


Figure 4.2. Maximum likelihood estimator for independent scattering parameters  $[D, \omega, \phi]$ .

#### 4.3.2 Part 2: Estimation of Emitter Parameters

In this section we design an estimator for emitter parameters  $\theta = [R, H, V, A]$  based on the scatterer parameter vectors  $[\hat{D}, \hat{\phi}, \hat{\omega}, \hat{a}]$  that were determined above. We begin by writing the measured Doppler shift for the  $i^{\text{th}}$  scatterer as a function  $g$  of the *true* emitter parameters  $\theta$  and the remaining *true* scattering parameters  $\alpha_i = [D_i, \phi_i]$  as

$$\hat{\omega}_i = g(\theta, \alpha_i) + e_{\omega_i}, \quad (4.1)$$

where  $e_{\omega_i}$  is the error in the  $i^{\text{th}}$  Doppler frequency estimate. The function  $g$  is a highly nonlinear function that is described in Appendices A, B, and C for different geometrical approximations. We do not know the true scatterer parameters  $\alpha_i$ , so we expand (4.1) in a truncated Taylor series about the estimates  $\hat{\alpha}_i$  as

$$\hat{\omega}_i \cong g(\theta, \hat{\alpha}_i) + \delta_{\alpha_{i1}} g'_{\alpha_{i1}}(\theta, \hat{\alpha}_i) + \delta_{\alpha_{i2}} g'_{\alpha_{i2}}(\theta, \hat{\alpha}_i) + e_{\omega_i}, \quad (4.2)$$

where  $\hat{\alpha}_{i1}$  and  $\hat{\alpha}_{i2}$  denote the  $i^{\text{th}}$  delay and azimuth estimates, respectively. We are assuming that the errors in scattering parameters are small and have retained only the zero- and first-order terms. This linear truncation of the Taylor series permits the use of a *best linear unbiased estimator* BLUE [67] approach. Note that  $\delta_{\alpha} = \alpha - \hat{\alpha}_i$  and  $g'_{\alpha_{i1}}$  denotes the partial derivative of  $g$  with respect to the variable  $\alpha_{i1}$ .

We next assume that we have an initial guess that is close to the true emitter parameters which are written as  $\theta = \{\theta_1, \theta_2, \theta_3, \theta_4\} = \{R, H, V, A\}$ . This starting point is denoted as  $\theta_0$  and will initially be obtained using a coarse least-squares search. This will be discussed in more detail in Section 4.3.4 below. We further expand (4.2) in a Taylor series about  $\theta_0$  as

$$\hat{\omega}_i \equiv g(\theta_0, \hat{\alpha}_i) + \delta_{\theta_1} g'_{\theta_1}(\theta_0, \hat{\alpha}_i) + \delta_{\theta_2} g'_{\theta_2}(\theta_0, \hat{\alpha}_i) + \delta_{\theta_3} g'_{\theta_3}(\theta_0, \hat{\alpha}_i) + \delta_{\theta_4} g'_{\theta_4}(\theta_0, \hat{\alpha}_i) + \left[ \delta_{\alpha_{i1}} g'_{\alpha_{i1}}(\theta_0, \hat{\alpha}_i) + \delta_{\alpha_{i2}} g'_{\alpha_{i2}}(\theta_0, \hat{\alpha}_i) + e_{\omega_i} \right], \quad (4.3)$$

which linearizes the problem in  $\delta_\theta$ . The term in square brackets denotes the noise caused by errors in estimating the scatterer delay, azimuth, and Doppler, and will be referred to as observation noise

$$n_i = \delta_{\alpha_{i1}} g'_{\alpha_{i1}}(\theta_0, \hat{\alpha}_i) + \delta_{\alpha_{i2}} g'_{\alpha_{i2}}(\theta_0, \hat{\alpha}_i) + e_{\omega_i}. \quad (4.4)$$

To determine  $\delta_\theta$  we rewrite (4.3) as

$$\delta_{\theta_1} g'_{\theta_1}(\theta_0, \hat{\alpha}_i) + \delta_{\theta_2} g'_{\theta_2}(\theta_0, \hat{\alpha}_i) + \delta_{\theta_3} g'_{\theta_3}(\theta_0, \hat{\alpha}_i) + \delta_{\theta_4} g'_{\theta_4}(\theta_0, \hat{\alpha}_i) = \hat{\omega}_i - g(\theta_0, \hat{\alpha}_i) - n_i, \quad (4.5)$$

which can be written in vector form as

$$\mathbf{A} \delta = \mathbf{z} - \mathbf{n}, \quad (4.6)$$

with

$$\mathbf{A} = \begin{bmatrix} g'_{\theta_1}(\theta_0, \hat{\alpha}_1) & g'_{\theta_2}(\theta_0, \hat{\alpha}_1) & g'_{\theta_3}(\theta_0, \hat{\alpha}_1) & g'_{\theta_4}(\theta_0, \hat{\alpha}_1) \\ g'_{\theta_1}(\theta_0, \hat{\alpha}_2) & g'_{\theta_2}(\theta_0, \hat{\alpha}_2) & g'_{\theta_3}(\theta_0, \hat{\alpha}_2) & g'_{\theta_4}(\theta_0, \hat{\alpha}_2) \\ \vdots & \vdots & \vdots & \vdots \\ g'_{\theta_1}(\theta_0, \hat{\alpha}_P) & g'_{\theta_2}(\theta_0, \hat{\alpha}_P) & g'_{\theta_3}(\theta_0, \hat{\alpha}_P) & g'_{\theta_4}(\theta_0, \hat{\alpha}_P) \end{bmatrix} \quad \delta = \begin{bmatrix} \delta_{\theta_1} \\ \delta_{\theta_2} \\ \delta_{\theta_3} \\ \delta_{\theta_4} \end{bmatrix}$$

and

$$\mathbf{z} = \begin{bmatrix} \hat{\omega}_1 - g(\theta_0, \hat{\alpha}_1) \\ \hat{\omega}_2 - g(\theta_0, \hat{\alpha}_2) \\ \vdots \\ \hat{\omega}_P - g(\theta_0, \hat{\alpha}_P) \end{bmatrix} \quad \mathbf{n} = \begin{bmatrix} \delta_{\alpha_{11}} g'_{\alpha_{11}}(\theta_0, \hat{\alpha}_1) + \delta_{\alpha_{21}} g'_{\alpha_{21}}(\theta_0, \hat{\alpha}_1) + e_{\omega_1} \\ \delta_{\alpha_{12}} g'_{\alpha_{12}}(\theta_0, \hat{\alpha}_2) + \delta_{\alpha_{22}} g'_{\alpha_{22}}(\theta_0, \hat{\alpha}_2) + e_{\omega_2} \\ \vdots \\ \delta_{\alpha_{1P}} g'_{\alpha_{1P}}(\theta_0, \hat{\alpha}_P) + \delta_{\alpha_{2P}} g'_{\alpha_{2P}}(\theta_0, \hat{\alpha}_P) + e_{\omega_P} \end{bmatrix}.$$

Equation (4.6) is in the form of a BLUE (best linear unbiased estimator), which is solved for  $\delta$  as

$$\delta = [\mathbf{A}^T \mathbf{R}_n^{-1} \mathbf{A}]^{-1} \mathbf{A}^T \mathbf{R}_n^{-1} \mathbf{z}, \quad (4.7)$$

which has minimum variance of

$$\text{var}(\hat{\theta}_i) = \text{var}(\hat{\delta}_i) = [(\mathbf{A}^T \mathbf{R}_n^{-1} \mathbf{A})^{-1}]_{ii} \quad (4.8)$$

and a parameter covariance matrix of

$$\mathbf{R}_{\hat{\theta}} = (\mathbf{A}^T \mathbf{R}_n^{-1} \mathbf{A})^{-1} . \quad (4.9)$$

The covariance matrix of the observation noise  $\mathbf{R}_n$  is

$$\mathbf{R}_n = \mathbf{R}_\omega + \mathbf{H}^T \mathbf{R}_\alpha \mathbf{H} \quad (4.10)$$

with

$$\mathbf{R}_\alpha = \begin{bmatrix} \mathbf{R}_D & \mathbf{0} \\ \mathbf{0} & \mathbf{R}_\phi \end{bmatrix} \quad (4.11)$$

and

$$\mathbf{H}^T = \begin{bmatrix} g'_D(\theta_0, \hat{D}_1) & & \mathbf{0} & g'_\phi(\theta_0, \hat{\phi}_1) & & \mathbf{0} \\ & \ddots & & & \ddots & \\ \mathbf{0} & & g'_D(\theta_0, \hat{D}_P) & \mathbf{0} & & g'_\phi(\theta_0, \hat{\phi}_P) \end{bmatrix} \quad (4.12)$$

The covariances for the individual scattering estimates are

$$\mathbf{R}_\omega = \begin{bmatrix} \sigma_{\omega_1}^2 & & & \\ & \sigma_{\omega_2}^2 & \mathbf{0} & \\ & \mathbf{0} & \ddots & \\ & & & \sigma_{\omega_P}^2 \end{bmatrix} \quad (4.13)$$

$$\mathbf{R}_D = \begin{bmatrix} \sigma_{D_1}^2 & & & \\ & \sigma_{D_2}^2 & \mathbf{0} & \\ & \mathbf{0} & \ddots & \\ & & & \sigma_{D_P}^2 \end{bmatrix} \quad (4.14)$$

$$\mathbf{R}_\phi = \begin{bmatrix} \sigma_{\phi_1}^2 & & & \\ & \sigma_{\phi_2}^2 & \mathbf{0} & \\ & \mathbf{0} & \ddots & \\ & & & \sigma_{\phi_P}^2 \end{bmatrix} \quad (4.15)$$

which are assumed to be known *a priori* for this development. This assumption is standard for localization problems [22]. When we apply this technique to Mountaintop data in Section 6.3, we will

use the CRLB expressions that will be given in Chapter 5, Equations (5.14)–(5.16), along with estimates of SNR for each scatterer, to determine the variance of the scatterer parameters.

Note that the PDF of the measurement errors was not included in any of the above development, only the covariance. This is a property of the BLUE estimator. When the PDF of the measurement errors is Gaussian, this estimator is also the MVU (minimum variance unbiased) estimator as well as the ML (maximum likelihood) estimator.

### 4.3.3 Physical Interpretation

We note the similarity between the BLUE estimator described by (4.7) and the weighted least squares estimator (LSE) [67] which can be written as

$$\boldsymbol{\delta} = [\mathbf{A}^T \mathbf{W} \mathbf{A}]^{-1} \mathbf{A}^T \mathbf{W} \mathbf{z}. \quad (4.16)$$

The weighting matrix  $\mathbf{W}$  is equal to the inverse of measurement error covariance matrix  $\mathbf{R}_n$ , described by (4.10)

$$\mathbf{W} = \mathbf{R}_n^{-1}. \quad (4.17)$$

With the weighted LSE interpretation, we can examine (4.16) in more detail to see what intuition can be gained for the localization problem at hand. The measurement error covariance matrix  $\mathbf{R}_n$  is the sum of the covariance matrix for the Doppler measurement  $\mathbf{R}_\omega$  and the product  $\mathbf{H}^T \mathbf{R}_\alpha \mathbf{H}$ . The matrix  $\mathbf{H}$  is a matrix of gradients, and  $\mathbf{R}_\alpha$  contains the covariance matrices of the time delay measurements  $\mathbf{R}_D$  and the angle measurements  $\mathbf{R}_\phi$ .

Consider the contribution from both a strong scatterer and a weak scatterer. The high SNR for the strong scatterer results in smaller measurement errors than that of the weak scatterer. Consequently, the weighting matrix  $\mathbf{W}$  will have a large weight corresponding to strong scatterer and a smaller weight corresponding to the weak scatterer. This is a fundamental property of weighted LS estimation.

The influence of the two matrices of gradients,  $\mathbf{H}$  and  $\mathbf{A}$ , is not immediately obvious, however. Consider two scatterers with equal signal-to-noise ratios but unequal gradient terms in  $\mathbf{H}$ . The scatterer possessing the smaller gradient will be weighted more heavily in the weighting matrix  $\mathbf{W}$ . The interpretation is that the smaller gradient means that a given measurement error will produce a smaller change in the desired parameters  $\boldsymbol{\delta}$ . The opposite is true for the gradient matrix  $\mathbf{A}$  that describes changes in scatterer differential Doppler as a function of the desired emitter parameters. If two scatterers are otherwise equal but one of them possesses a larger gradient in  $\mathbf{A}$ , then the contribution of that scatterer will be weighted more heavily. Such a scatterer can be thought of as possessing more information about the emitter parameters. This effect will sometimes allow weaker, distant scatterers to count more heavily in the solution than strong close-range scatterers.

#### 4.3.4 Solution Technique

The estimation procedure begins by first estimating the differential delay, Doppler, and azimuth of  $P$  dominant scatterers as described in Section 4.3.1. With the scatterer parameters available, we proceed with the development in Section 4.3.2, which requires an initial guess at the emitter parameters  $\theta_0$ . This can be obtained by performing a coarse multidimensional least-squares search over the parameter space of  $\theta$ , which can be written as

$$J = \sum_{i=1}^P |\hat{\omega}_i - g(\theta, \hat{\alpha}_i)|^2. \quad (4.18)$$

As with the estimator developed in the previous chapter, we can omit emitter altitude from the coarse search if desired. Any nominal altitude will be close enough to start the iterative procedure required for the final estimates.

We denote the result of the coarse search as  $\theta_0$  and determine  $\delta$  using (4.7). We then replace

$$\theta_0 \leftarrow \theta_0 + \delta \quad (4.19)$$

and repeat the computation. We repeat the iterations until the norm of  $\delta$  is sufficiently small. When this occurs, the error in the emitter parameters is described by (4.8) above.

#### 4.4 CHAPTER SUMMARY

A two-part estimator has been designed that is based on an inhomogeneous clutter assumption. The scatterer parameters of relative time delay, differential Doppler, azimuth, and amplitude were estimated first. These scatterer estimates were then used to estimate the desired emitter parameters of range, heading, velocity, and altitude. The estimator was shown to be the MVU and ML estimator when the PDF of the measurement noise is Gaussian. The covariance of the emitter parameters was also determined. This estimator will be used to localize emitters using simulations in Chapter 5 and using Mountaintop field data in Chapter 6.

## 5. ESTIMATOR PERFORMANCE

### 5.1 INTRODUCTION

The theoretical performance of the estimators designed in Chapters 3 and 4 is considered in this chapter via the Cramer-Rao lower bounds (CRLB). The CRLB describe the minimum variance for parameter estimates that an unbiased estimator can achieve. The CRLB will be determined for each estimator and evaluated for a number of localization scenarios. The effect of varying the emitter parameters of range, heading, velocity, altitude, and power, as well as the receiver parameters of bandwidth, beamwidth, steering direction, integration time, etc., will be studied. We also consider the consequences of some of the simplifying assumptions that were used to design the estimators and how these assumptions could lead to optimistic performance calculations when applied to experimental field data. The estimator based on the homogeneous clutter model is discussed in Section 5.2 and the estimator based on the inhomogeneous clutter model is discussed in Section 5.3. Monte-Carlo simulations are performed for each estimator to validate both the bounds calculations and the overall implementation of the estimators.

### 5.2 ESTIMATOR FOR THE HOMOGENEOUS CLUTTER MODEL

#### 5.2.1 Determination of the Cramer-Rao Lower Bounds

The covariance of the emitter parameter estimates is equal to the inverse of the Fisher information matrix [68],[69]. The diagonal elements of the inverted matrix are equal to the CRLB. The elements of the Fisher information matrix are defined by

$$F_{ij} = E \left\{ \left( \frac{\partial}{\partial \theta_i} \ln f_z(\mathbf{z}|\boldsymbol{\theta}) \right) \left( \frac{\partial}{\partial \theta_j} \ln f_z(\mathbf{z}|\boldsymbol{\theta}) \right) \right\} = - E \left\{ \frac{\partial^2}{\partial \theta_i \partial \theta_j} \ln f_z(\mathbf{z}|\boldsymbol{\theta}) \right\} , \quad (5.1)$$

where  $f_z(\mathbf{z}|\boldsymbol{\theta})$  is the likelihood function that was developed in Chapter 3 for the homogeneous clutter model. The log likelihood function is written as

$$\ln f_z(\mathbf{z}|\boldsymbol{\theta}) = \ln \left( \frac{1}{\pi^N \sigma^{2N}} \right) - \left( (\mathbf{z} - \mathbf{m}(\boldsymbol{\theta}))^H (\mathbf{z} - \mathbf{m}(\boldsymbol{\theta})) / \sigma^2 \right) . \quad (5.2)$$

Using the right side of (5.1) we write

$$F_{ij} = - E \left\{ \frac{\partial}{\partial \theta_i \partial \theta_j} \ln f_z(\mathbf{z}|\boldsymbol{\theta}) \right\} = E \left\{ \frac{\partial}{\partial \theta_i \partial \theta_j} \left[ (\mathbf{z} - \mathbf{m}(\boldsymbol{\theta}))^H (\mathbf{z} - \mathbf{m}(\boldsymbol{\theta})) / \sigma^2 \right] \right\} . \quad (5.3)$$

The product in square brackets can be written as



$$|\mathbf{z}|^2 + |\mathbf{m}(\boldsymbol{\theta})|^2 - \mathbf{m}(\boldsymbol{\theta})^H \mathbf{z} - \mathbf{z}^H \mathbf{m}(\boldsymbol{\theta}) , \quad (5.4)$$

which can be expanded in terms of the real and imaginary parts of  $\mathbf{m}$  and  $\mathbf{z}$  as

$$\sum_{n=1}^N \left( z_r^2(n) + z_i^2(n) + m_r^2(n) + m_i^2(n) - 2(m_r(n)z_r(n) + m_i(n)z_i(n)) \right) . \quad (5.5)$$

We insert (5.5) into (5.3) to obtain the elements of the Fisher information matrix,

$$\begin{aligned} F_{ij} &= \frac{1}{\sigma^2} E \left\{ \frac{\partial^2}{\partial \theta_i \partial \theta_j} \left( \sum_n \left( z_r^2 + z_i^2 + m_r^2 + m_i^2 - 2(m_r z_r + m_i z_i) \right) \right) \right\} \\ &= \frac{1}{\sigma^2} E \left\{ \left( \sum_{n=1}^N \frac{\partial}{\partial \theta_i} \left( 2m_r \frac{\partial m_r}{\partial \theta_j} + 2m_i \frac{\partial m_i}{\partial \theta_j} - 2z_r \frac{\partial m_r}{\partial \theta_j} - 2z_i \frac{\partial m_i}{\partial \theta_j} \right) \right) \right\} \\ &= \frac{2}{\sigma^2} E \left\{ \left( \sum_{n=1}^N \left( \frac{\partial m_r}{\partial \theta_i} \frac{\partial m_r}{\partial \theta_j} + \frac{\partial m_i}{\partial \theta_i} \frac{\partial m_i}{\partial \theta_j} + m_r \frac{\partial^2 m_r}{\partial \theta_i \partial \theta_j} + m_i \frac{\partial^2 m_i}{\partial \theta_i \partial \theta_j} - z_r \frac{\partial^2 m_r}{\partial \theta_i \partial \theta_j} - z_i \frac{\partial^2 m_i}{\partial \theta_i \partial \theta_j} \right) \right) \right\} \\ &= \frac{2}{\sigma^2} \sum_{n=1}^N \left( \frac{\partial m_r}{\partial \theta_i} \frac{\partial m_r}{\partial \theta_j} + \frac{\partial m_i}{\partial \theta_i} \frac{\partial m_i}{\partial \theta_j} \right) . \end{aligned} \quad (5.6)$$

The last simplification made use of the fact that  $E\{z\} = m$ . (The sample index  $n$  has been omitted from each term for convenience but we note that the sum is over  $N$ , the entire length of the data vector.) This result is similar to the results for frequency estimation described elsewhere [70]. Equation (5.6) can also be written in vector form

$$\frac{2}{\sigma^2} \text{Re} \left[ \frac{\partial \mathbf{m}(\boldsymbol{\theta})^H}{\partial \theta_i} \frac{\partial \mathbf{m}(\boldsymbol{\theta})}{\partial \theta_j} \right] .$$

To make use of this result in (5.6), we rewrite

$$m(n) = \sum_{p=1}^P a_p s(n - D_p) e^{j\omega_p(n - D_p)} \quad (5.7)$$

as

$$\begin{aligned} m(n) &= m_r(n) + jm_i(n) = \sum_{p=1}^P |a_p| |s(n - D_p)| \cos(\omega_p(n - D_p) + \varphi_{s(n - D_p)} + \varphi_{a_p}) \\ &\quad + j \sum_{p=1}^P |a_p| |s(n - D_p)| \sin(\omega_p(n - D_p) + \varphi_{s(n - D_p)} + \varphi_{a_p}) , \end{aligned} \quad (5.8)$$

which uses an amplitude-phase representation for the complex filter coefficients  $a_p$  and emitter waveform  $s(n)$ . To compute the Fisher information matrix we use (5.8) in (5.6) and differentiate with respect to the desired parameters. (Note that the emitter waveform  $s(n)$  is included in the bound calculation.) The three

parameters we are mainly interested in are emitter range  $R$ , heading  $H$ , and velocity  $V$ . However, we see from (5.8) that each emitter multipath beam will contain  $2P$  nuisance parameters corresponding to the amplitude and phase of each filter coefficient. Thus the Fisher information matrix will be a square matrix with  $2BP+3$  rows and columns where  $B$  is the number of beams. The emitter parameters of  $(R, H, V)$  are contained in the  $\omega_p$  term which is given by

$$\omega_p(R, H, V) = \frac{2\pi V}{\lambda} \left[ \cos H - \cos \left( H + \sin^{-1} \left( \frac{(D_p^2 + 2RD_p) \sin \phi}{D_p^2 + 2(R^2 + RD_p)(1 - \cos \phi)} \right) \right) \right] \quad (5.9)$$

for the two-dimensional approximation that ignores altitude. This equation is derived in Appendix A.

The details of the calculation of the Fisher information matrix are relegated to Appendix D; however, the form of the matrix is interesting and worth a few comments. If we write  $F_{ij} = \frac{\partial^2(\cdot)}{\partial \theta_i \partial \theta_j}$ , then, after we perform the differentiation and expectation operations, we are left with a matrix (for a single beam) of the form

$$\mathbf{F} = - \begin{bmatrix} \frac{\partial^2(\cdot)}{\partial R^2} & \frac{\partial^2(\cdot)}{\partial R \partial H} & \frac{\partial^2(\cdot)}{\partial R \partial V} & \frac{\partial^2(\cdot)}{\partial R \partial \phi_1} & \frac{\partial^2(\cdot)}{\partial R \partial \phi_2} & \dots & \frac{\partial^2(\cdot)}{\partial R \partial \phi_P} & 0 & 0 & \dots & 0 \\ \frac{\partial^2(\cdot)}{\partial H \partial R} & \frac{\partial^2(\cdot)}{\partial H^2} & \frac{\partial^2(\cdot)}{\partial H \partial V} & \frac{\partial^2(\cdot)}{\partial H \partial \phi_1} & \frac{\partial^2(\cdot)}{\partial H \partial \phi_2} & \dots & \frac{\partial^2(\cdot)}{\partial H \partial \phi_P} & 0 & 0 & \dots & 0 \\ \frac{\partial^2(\cdot)}{\partial V \partial R} & \frac{\partial^2(\cdot)}{\partial V \partial H} & \frac{\partial^2(\cdot)}{\partial V^2} & \frac{\partial^2(\cdot)}{\partial V \partial \phi_1} & \frac{\partial^2(\cdot)}{\partial V \partial \phi_2} & \dots & \frac{\partial^2(\cdot)}{\partial V \partial \phi_P} & 0 & 0 & \dots & 0 \\ \frac{\partial^2(\cdot)}{\partial \phi_1 \partial R} & \frac{\partial^2(\cdot)}{\partial \phi_1 \partial H} & \frac{\partial^2(\cdot)}{\partial \phi_1 \partial V} & \frac{\partial^2(\cdot)}{\partial \phi_1^2} & 0 & 0 & 0 & 0 & 0 & \dots & 0 \\ \frac{\partial^2(\cdot)}{\partial \phi_2 \partial R} & \frac{\partial^2(\cdot)}{\partial \phi_2 \partial H} & \frac{\partial^2(\cdot)}{\partial \phi_2 \partial V} & 0 & \frac{\partial^2(\cdot)}{\partial \phi_2^2} & 0 & 0 & 0 & 0 & \dots & 0 \\ \vdots & \vdots & \vdots & 0 & \dots & \ddots & \vdots & \vdots & \vdots & \dots & \vdots \\ \frac{\partial^2(\cdot)}{\partial \phi_P \partial R} & \frac{\partial^2(\cdot)}{\partial \phi_P \partial H} & \frac{\partial^2(\cdot)}{\partial \phi_P \partial V} & 0 & \dots & 0 & \frac{\partial^2(\cdot)}{\partial \phi_P^2} & 0 & 0 & \dots & 0 \\ 0 & 0 & 0 & 0 & \dots & 0 & 0 & \frac{\partial^2(\cdot)}{\partial a_1^2} & 0 & \dots & 0 \\ 0 & 0 & 0 & 0 & \dots & 0 & 0 & 0 & \frac{\partial^2(\cdot)}{\partial a_2^2} & \dots & 0 \\ \vdots & \vdots & \vdots & \vdots & \vdots & \vdots & \vdots & \vdots & \vdots & \ddots & \vdots \\ 0 & 0 & 0 & 0 & \dots & 0 & 0 & 0 & 0 & \dots & \frac{\partial^2(\cdot)}{\partial a_P^2} \end{bmatrix} \quad (5.10)$$

for the case of the filter delays spaced equal to or greater than the correlation length of the emitter waveform  $s(n)$ . The zeros in the matrix indicate a lack of coupling between parameter estimates, i.e.,

uncertainty in one parameter estimate does not affect the variance that can be achieved for the other parameter estimate. For this problem, we can see that the amplitude estimates are uncoupled from each other and from all other parameters. However, the phase estimates are coupled with the desired parameters and the desired parameters are coupled with each other. This means, for example, that our ability to measure emitter range when the emitter velocity is unknown will be degraded from the case when the emitter velocity is known.

Due to the block structure of the Fisher information matrix, it will not be necessary to invert the whole  $2P+3$  matrix. We can write

$$\mathbf{F} = \begin{bmatrix} \mathbf{A} & \mathbf{0} \\ \mathbf{0} & \mathbf{B} \end{bmatrix}, \quad (5.11)$$

where  $\mathbf{B}$  is the  $P$  by  $P$  diagonal matrix of derivatives with respect to the scatterer amplitudes. Hence the inverse of the information matrix is

$$\mathbf{F}^{-1} = \begin{bmatrix} \mathbf{A}^{-1} & \mathbf{0} \\ \mathbf{0} & \mathbf{B}^{-1} \end{bmatrix}, \quad (5.12)$$

and we need only to evaluate  $\mathbf{A}^{-1}$ . For the variance of the emitter parameters, the only terms of interest are the first three diagonal elements of  $\mathbf{A}^{-1}$ .

If we want to estimate the emitter altitude as well as range, velocity, and heading, then the size of the information matrix will be  $2BP+4$ . A three-dimensional approximation for the Doppler terms that includes the emitter altitude is

$$\omega_p(R, H, V, A) \cong \frac{2\pi V}{\lambda} \left[ \cos H - \left( 1 - \frac{A^2}{R_{es}^2} \right) \cos \left( H + \sin^{-1} \left( \frac{(D_p^2 + 2RD_p) \sin \phi}{D_p^2 + 2(R^2 + RD_p)(1 - \cos \phi)} \right) \right) \right], \quad (5.13)$$

where  $A$  is the emitter altitude and  $R_{es}$  is the range from the emitter to the scattering patch. This equation is derived in Appendix B. It reduces to (5.9) when the emitter altitude is set to zero.

In the remainder of the section we shall compute the CRLB for several engagement scenarios. We shall also perform Monte-Carlo simulations which serve to validate the bounds calculations and simulations.

## 5.2.2 CRLB Calculations and Behavior

The performance of these estimators is scenario dependent. The CRLB depend on both the emitter parameters and the receiver parameters. In this section we study the behavior of the bounds while varying several of these parameters. The emitter parameters that we shall consider include power, range, heading,

velocity, and altitude. For the receiver, we consider bandwidth, beamwidth, steering direction, number of beams, integration time, etc. While this section focuses on the estimator for the homogeneous clutter model, most of these results are directly applicable to the estimator for the inhomogeneous clutter model that is covered in Section 5.3.

Once the localization scenario and filter parameters are specified, the CRLB are determined by inverting (5.10). The initial localization scenario is shown in Figure 5.1 with the corresponding delay and Doppler contours spaced by  $25 \mu\text{s}$  and  $50 \text{ Hz}$ , respectively. The emitter range is  $100 \text{ km}$ , the altitude is  $7 \text{ km}$ , and the velocity is  $150 \text{ m/s}$  with a heading of  $90$  degrees. The nominal receiver azimuth is  $30$  degrees and the other receiver parameters were taken from Table 2.1. The nominal emitter power is  $500 \text{ Watts}$  spread over the  $200 \text{ kHz}$  bandwidth of the receiver.

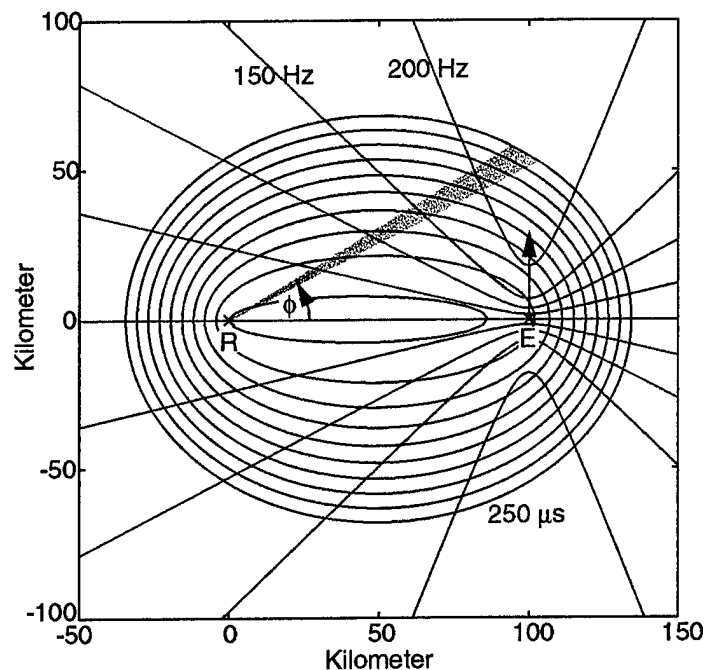


Figure 5.1. Basic localization scenario for CRLB analysis.

The tapped-delay-line architecture of the localization filter was shown in Figure 3.3. For the bounds calculations, the filter employs 50 coefficients (or taps) spaced  $5 \mu\text{s}$  apart for a total delay extent of  $250 \text{ ms}$  (or equivalently,  $75 \text{ km}$ ). The magnitude of the filter coefficients is determined using the constant-gamma scattering model of Equation (3.2) with a gamma of  $-20 \text{ dB}$ . Figure 5.2(a) shows a map of the bistatic reflectivity in the  $8$ -degree receive beam. The average value is about  $-45 \text{ dB}$  meters per

square meter. Figure 5.2(b) shows the receive power per square meter of terrain. The corresponding emitter signal-to-noise ratio, versus delay and Doppler, is shown in Figure 5.2(c) for an integration period of 40 ms. This interval corresponds to 16 PRIs of recorded Mountaintop data. The amplitude of the filter coefficients is shown in Figure 5.2(d). This is the ratio between the scattered power and the direct-path power and is hence independent of the emitter transmit or receiver noise power.

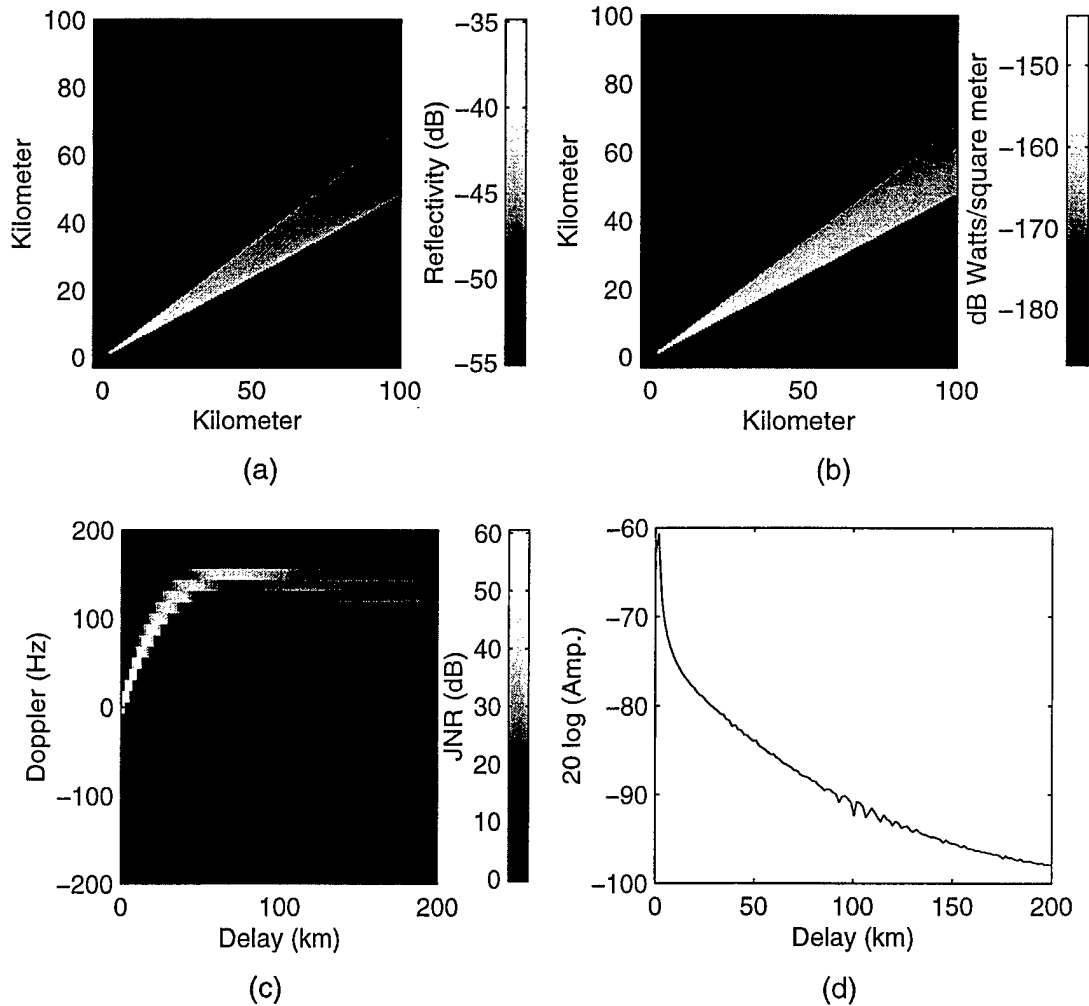


Figure 5.2. Outputs from scattering model include (a) reflectivity map, (b) scattered power map, (c) delay-Doppler map, and (d) filter coefficient amplitude for an 8-degree beam at 30 degrees azimuth.

The first parameter we shall consider is the emitter velocity. Figure 5.3(a)–(d) illustrates the RMS error (or standard deviation) calculations for the four localization parameters of range, heading, velocity, and altitude as a function of emitter velocity. We are showing the square root of the emitter variance given by the Cramer Rao lower bounds. We see from the figure that the emitter range, heading, and altitude estimates are inversely proportional to emitter velocity. When the emitter velocity is zero, the range, heading, and velocity errors are infinite and this localization technique fails. (Hence the inclusion of the word “moving” in the report title.) Note that the RMS velocity errors are independent of the velocity of the emitter. A similar result occurs in tone estimation problems, i.e., the ability to estimate the frequency of a tone is generally independent of the tone’s frequency.

We next compute the CRLB as a function of emitter altitude. The results are shown in Figure 5.4. The Doppler expressions were taken from the three-dimensional approximation described in Appendix B. We see that the ability to estimate the emitter parameters of range, heading, and velocity is essentially independent of emitter altitude, but that the RMS altitude error is inversely proportional to the emitter altitude. This behavior can be understood in terms of conical angles versus azimuthal angles. As the emitter altitude increases, the conical angles depart more quickly from the azimuthal angles and this facilitates better altitude estimation. Another point is that the RMS errors for the other parameters can be seen to increase slightly as the altitude increases. This behavior is explained by the fact that as the altitude increases, the Doppler shift at each patch on the ground decreases slightly. The decrease in Doppler is equivalent to a decrease in emitter velocity which, from Figure 5.3, was shown to increase parameter errors.

The CRLB versus receiver azimuth is shown in Figure 5.5 and the CRLB versus emitter heading is shown in Figure 5.6. The behavior of the bounds in these figures is more difficult to interpret without looking at the individual expressions for the elements in the Fisher information matrix. One generalization that can be made is that the more Doppler spread across the length of the filter, the better the estimator will perform.

There are several additional parameters upon which the localization performance will depend. These include the scattered SNR, integration time, number of receive beams, receiver bandwidth, beamwidth, etc. Some of the relations may be observed by examining the expressions for the CRLB or be obtained by evaluating the bounds directly. Many of these additional parameters will be discussed in the remainder of this subsection. Some of the relations cannot be determined fully from the CRLB described here due to assumptions and simplifications made in the statistical formulation of the likelihood function. Examples of this are the effect of changing the receive bandwidth or beamwidth and these will be described below as well.

The variance of the emitter parameter estimates is inversely proportional to SNR or, alternatively, the RMS error is inversely proportional to the square root of the SNR. The SNR of the scattered signals is proportional to the product of emitter power and the terrain reflectivity as well as the area of the delay-azimuth cell. The SNR is (approximately) inversely proportional to the square of the emitter range.

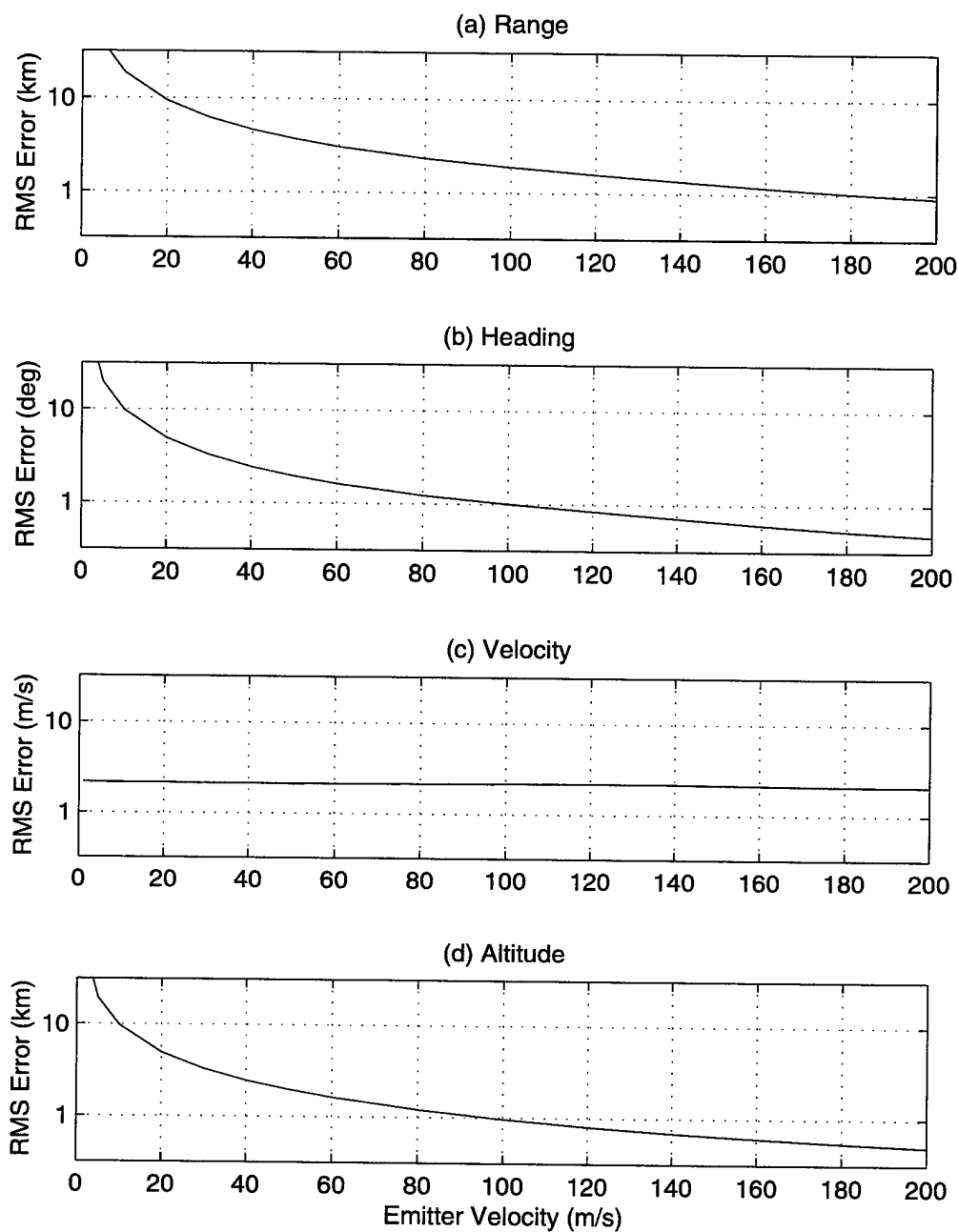


Figure 5.3. CRLB for the emitter parameters of (a) range, (b) heading, (c) velocity, and (d) altitude all as a function of emitter velocity.

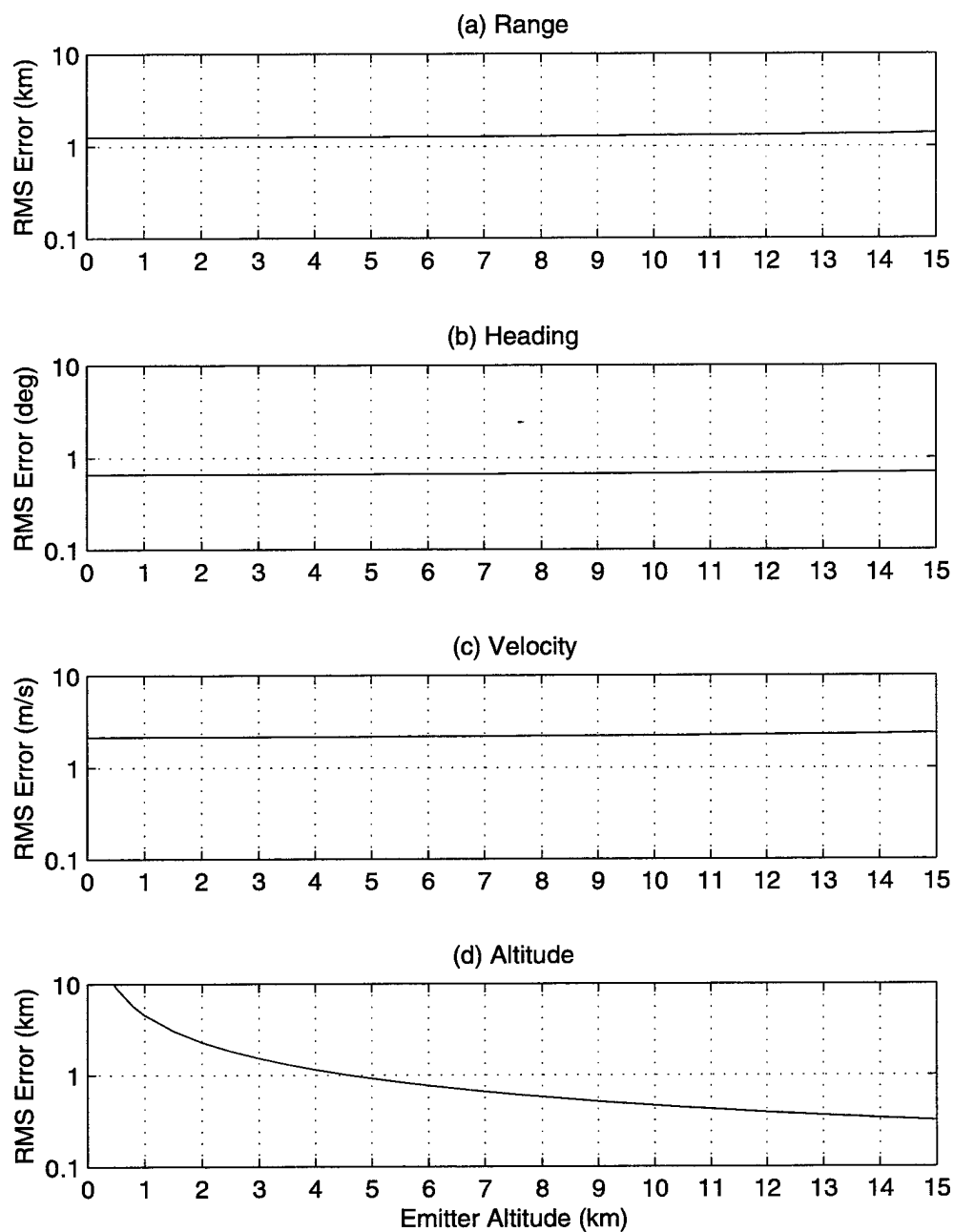


Figure 5.4. CRLB for the emitter parameters of (a) range, (b) heading, (c) velocity, and (d) altitude all as a function of emitter altitude.



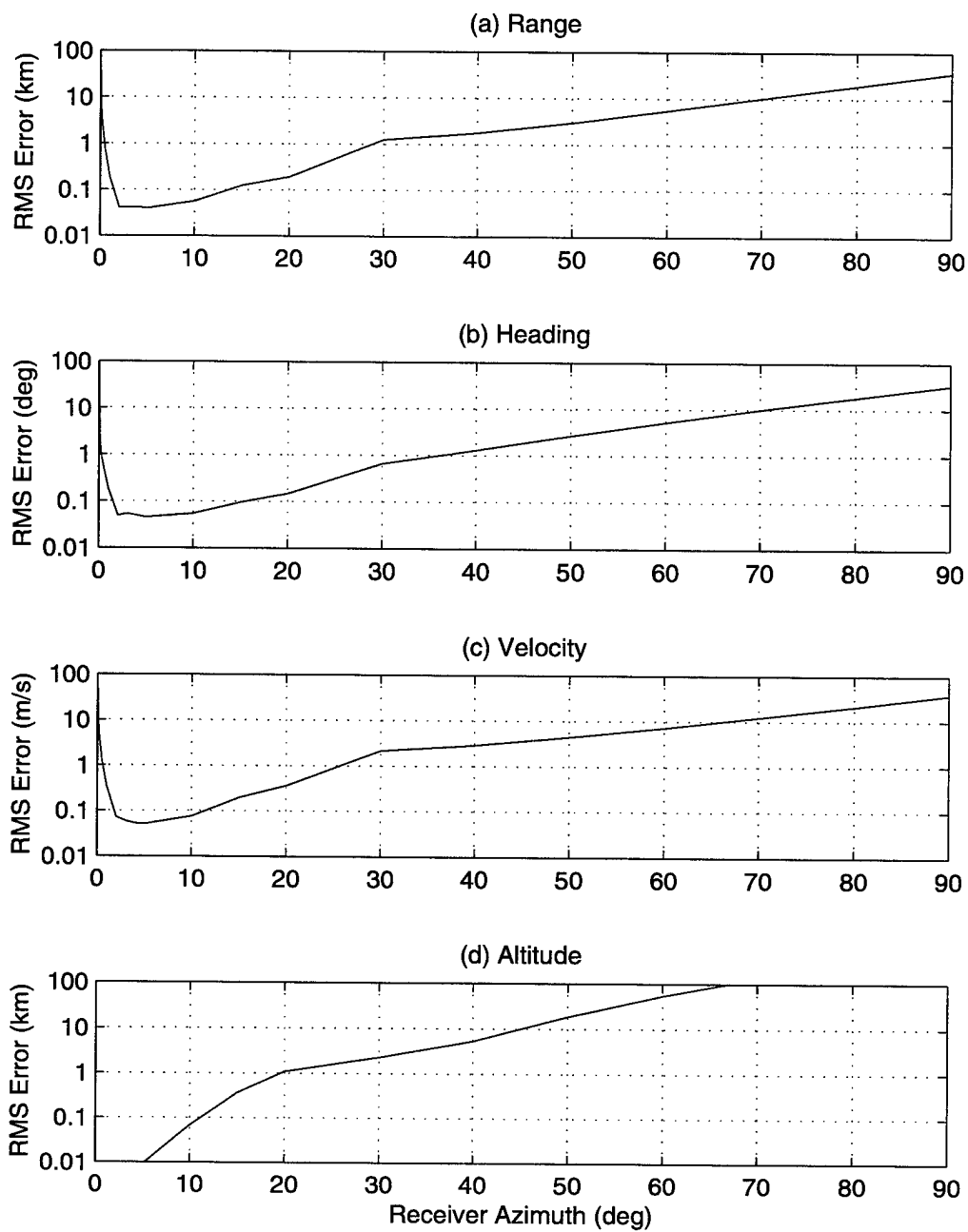


Figure 5.5. CRLB for the emitter parameters of (a) range, (b) heading, (c) velocity, and (d) altitude all as a function of receive azimuth.

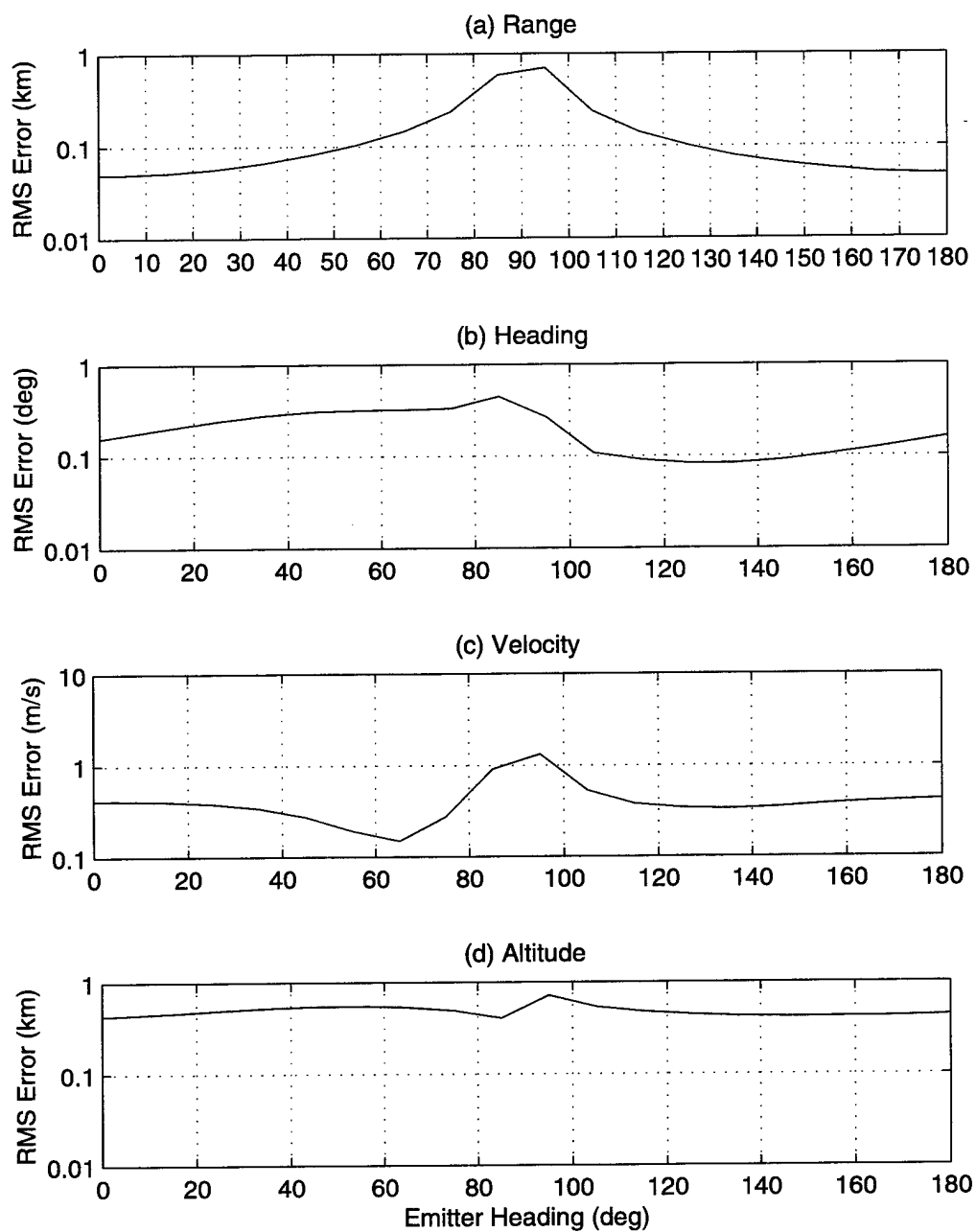


Figure 5.6. CRLB for the emitter parameters of (a) range, (b) heading, (c) velocity, and (d) altitude all as a function of emitter heading.

The variance of the parameter estimates is inversely proportional to the sample length (or integration time) to the third power. This is similar to tone estimation problems [70] where the variance of the frequency estimates is inversely proportional to  $N^3$ . However, as integration times become very lengthy, Doppler dispersion may be an important factor. That is, the assumption that all of the scattering in a single delay-azimuth cell will occur at the same Doppler frequency may not be valid. This could be circumvented by expanding the localization filter to include multiple Doppler modulators per delay tap.

Estimation performance improves when more beams are included. If we use two very close beams at, say 30 and 30.1 degrees, the parameter variance is reduced by a factor of two. If, however, we use two widely spaced beams at +30 and -30 degrees, the variance was found to drop by a factor of 100. For the first case, very little new information is provided by the second beam at 30.1 degrees. The factor-of-two improvement is due to an increased gain against noise. However, for the second case, the -30 degree beam provides a "different look" at the emitter, and the two beams combined provide a significant performance enhancement over either single beam individually. This behavior is related to GDOP which was described in Section 2.4.2.

We next consider the bandwidth of the receiver. The reciprocal of the receiver bandwidth was used to specify tap spacing in the localization filter. However, if we reduced the bandwidth and corresponding number of taps by a factor of two, the performance remains unchanged because the size of the delay-azimuth cell (and corresponding scattered SNR) increases by a factor of two. The net effect, based on the statistical formulation presented herein, is no change in performance. There is a hidden cost to a reduction in bandwidth however. As the area of the delay-azimuth cell increases, the amount of Doppler dispersion in a given cell will increase. As was the case with increased integration times, multiple Doppler modulators may be required to cope with the increase in Doppler dispersion.

The same effect occurs for an increase in the receive beamwidth. If the receive antenna beamwidth increases, its gain will drop but the product of gain and the beamwidth is constant. Thus there will be no change in the CRLB as calculated above, but again the increased cell area means increased Doppler dispersion. The effect of Doppler dispersion on the bounds will be discussed further in Section 5.4.

We next present the results of some Monte-Carlo simulations and follow with a discussion of the performance of the estimator that is based on an inhomogeneous clutter model. That estimator has more concrete ties to receiver bandwidth, beamwidth, and integration time.

### 5.2.3 Monte-Carlo Simulations

Monte-Carlo simulations were performed to assure that the estimates generated by the ML estimator described in Chapter 3 achieve the CRLB determined in this chapter. The simulations consisted of generating data vectors using Equation (3.3) for many different realizations of the emitter waveform and noise, applying the localization filter of Figure 3.3 while keeping track of the statistics of the estimates. This provides a good check on the derivation and implementation of the model, estimator, and CRLB calculations. However, the simulations do not necessarily describe how well the model will match

field data collected by an actual receiver over real terrain. Application of the CRLB to real data will be considered further in Section 5.4.

Before proceeding, we first review the properties of maximum likelihood estimators (taken from [17]):

1. *The MLE is asymptotically unbiased.* This means that as the number of observations increase, the bias tends to zero.
2. *The MLE is consistent.* This means that the mean-squared estimation error tends to zero as the number of observations increases.
3. *The MLE is asymptotically efficient.* An efficient estimator is one that achieves the CRLB.
4. *Asymptotically, the maximum likelihood estimate is, in general, distributed as a Gaussian random variable.*

This section examines properties 1, 3, and 4. (Property 2 was addressed in the previous section where we noted that the CRLB was inversely proportional to the third power of the number of observations.) These properties state that if we perform enough independent simulations, we should obtain parameter estimates that are Gaussian distributed (*property 4*) with means equal to the true parameters (*property 1*) and variances equal to the CRLB (*property 3*).

The radar-emitter scenario for the Monte-Carlo simulations is the same as that used in Section 5.2.2. The CRLB versus emitter-to-noise ratio was computed, and over 100 simulations were performed for each of four different emitter power levels. The results are shown in Figure 5.7. The asterisks represent the RMS estimation error for the independent simulations. We see from the figure that the estimator achieves the CRLB as expected. (Some statistical fluctuation around the CRLB can also be expected.)

Another way to view the simulation results is to plot the density functions of the parameter estimates. As noted above, the estimates should be Gaussian random variables with variances described by the CRLB. Figure 5.8 shows the density of the emitter range and heading estimates as histograms along with normalized Gaussian PDFs shown for reference. The normalized Gaussian PDFs use the true parameters of range or heading for the mean and the CRLB for the variance. The two figures show that Monte-Carlo estimates fit the Gaussian distributions well.

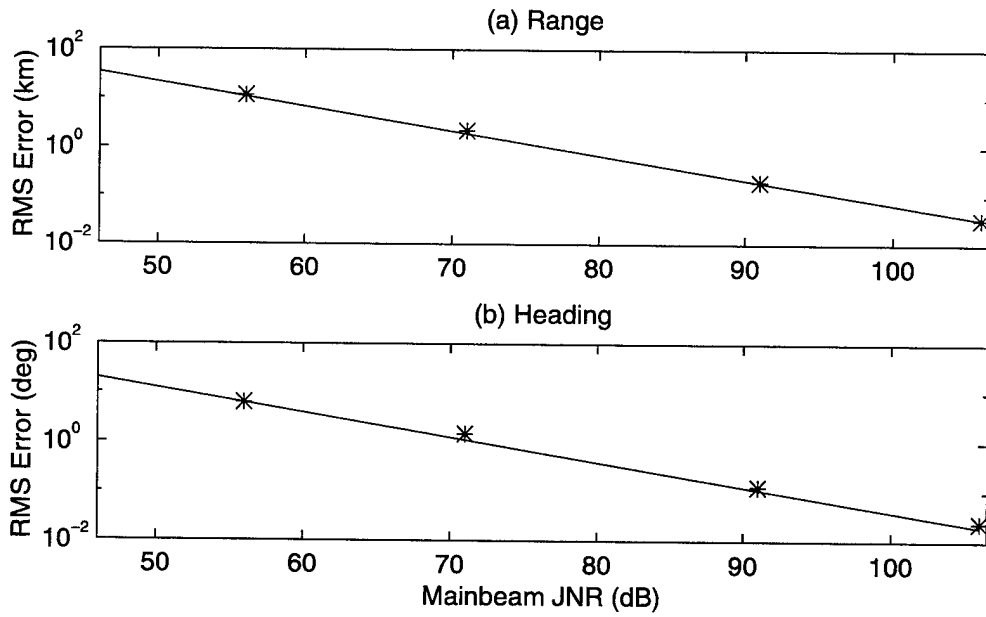


Figure 5.7. Comparison of Monte-Carlo simulations (\*) to CRLB calculations for (a) range and (b) heading.

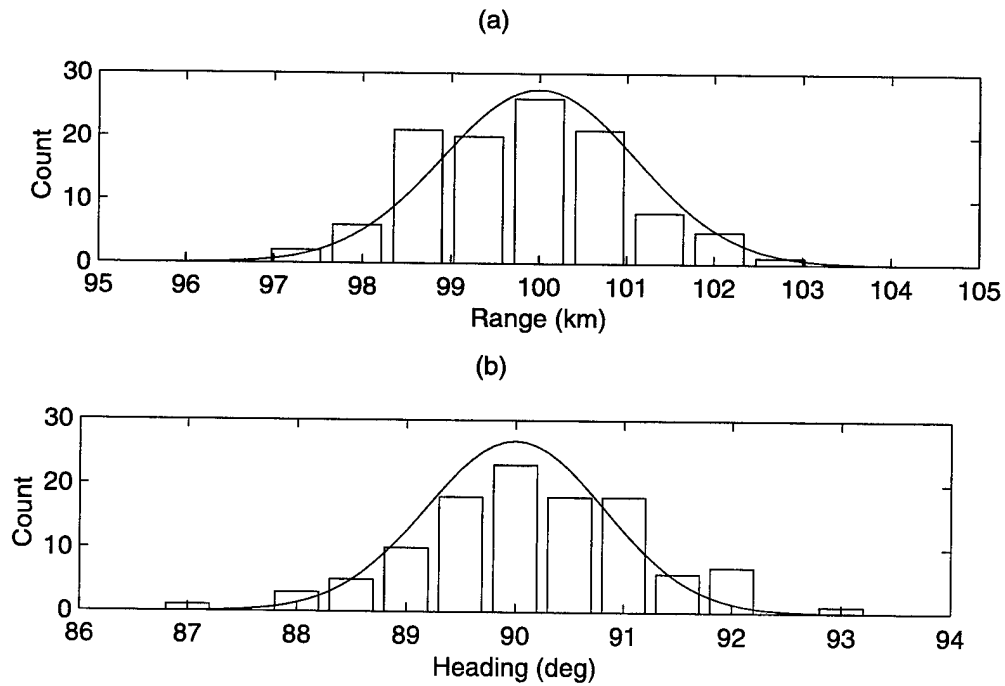


Figure 5.8. (a) Emitter range and (b) heading histograms for 110 simulations. The mean range was 99.85 and the mean heading was 90.16. The solid curve represents the theoretical PDF based on the CRLB calculations.

### 5.3 ESTIMATOR FOR THE INHOMOGENEOUS CLUTTER MODEL

The covariance of the emitter parameters for the estimator based in an inhomogeneous clutter model was specified in Chapter 4 by Equations (4.9)–(4.15). These expressions relate the localization errors to the errors present in the scatterer delay, Doppler, and azimuth estimates through the gradient matrices  $\mathbf{A}$  and  $\mathbf{H}$ . Since these matrices were already specified in Chapter 4, all we need specify to complete the bounds calculations is the variance of the scattering parameters.

The variance of the scattering parameters will be taken from the CRLB for point targets. Hence we are assuming that the discrete scatterers present in the inhomogeneous clutter have the same bounds as conventional point targets. The bounds depend on SNR as well as characteristics of the receiver including bandwidth, beamwidth, and integration time. The CRLB for delay  $D$ , Doppler  $f$ , angle  $\phi$ , and amplitude  $a$  can be shown to be, respectively [67],[71]

$$\text{var}(\hat{D}) \geq \frac{12}{(2\pi)^2(\eta N)B} \quad , \quad (5.14)$$

$$\text{var}(\hat{f}) \geq \frac{12}{(2\pi)^2(\eta N)(N^2 - 1)} \quad , \quad (5.15)$$

$$\text{var}(\hat{\phi}) \geq \frac{12}{(2\pi)^2(\eta N)M^2 \frac{\sin^2(\phi)}{4}} \quad , \quad (5.16)$$

$$\text{var}(\hat{a}) \geq \frac{\sigma_g^2}{N} \quad , \quad (5.17)$$

where  $\eta = a^2 \sigma_s^2 / \sigma_g^2$  is the mainbeam SNR per sample,  $B$  is the signal bandwidth,  $T$  is the signal duration,  $M$  is the number of elements in the array, and  $\phi$  is the angle to the scatterer measured from boresight. The product  $\eta N$  represents the SNR at the output of the correlator which has been increased by a factor of  $N$  over the per-sample value. Note that the SNR  $\eta$  is actually an estimate  $\hat{\eta} = \hat{a}^2 \sigma_s^2 / \sigma_g^2$  because it contains the amplitude estimate  $\hat{a}$ . The variance of the additive thermal noise  $\sigma_g^2$  is assumed to be known. Typical values for the Mountaintop system for a point scatterer with an SNR of 10 dB are  $\sigma_D=0.26$  km,  $\sigma_\omega=21.4$  rad/s, and  $\sigma_\phi=0.71$  deg. In general, the emitter localization errors for the Mountaintop system will be dominated by the Doppler errors which are larger in magnitude than the delay or angle terms.

#### 5.3.1 Parameter Covariance Calculations

The localization parameter covariances can be determined once the scatterer SNR and scatterer spatial distribution have been specified. For a general simulation, we would select scatterers from a

uniform distribution as suggested in Section 2.2.1. However, we begin here by selecting a scatterer SNR and distribution that matches the scattering levels for the homogeneous case discussed in Section 5.2.2. That is, we locate 50 scatterers on the 30-degree receive beam, evenly spaced in bistatic delay, with SNR levels corresponding to the levels present for the homogeneous case. This facilitates a direct comparison between the parameter variances for the inhomogeneous case and the parameter variances for the homogeneous case when the scattering levels are assumed to be equivalent.

As expected, the result for the two calculations are essentially identical as can be seen in Figure 5.9. Although both estimators use the data differently, we achieve the same result because both ML estimators minimize the variance of the emitter parameters. The first estimator chooses the set of emitter parameters that deterministically produces the set of Doppler modulators that best match the received data, while the second estimator selects emitter parameters that best match the set of discrete scatterer parameters. The likelihood function for the homogeneous case deals directly with the measured data while the likelihood function for the inhomogeneous case is in terms of the scatterer estimates.

The small differences apparent in Figure 5.9 are probably due to the different approximations made during the statistical formulation for each case. For example, the first estimator treated time delay and azimuth as known independent variables while the second estimator treated these as noisy estimates. Conversely, the second estimator treats the scattering SNR as if it were known exactly, while the first estimator treats scattering amplitudes as nuisance parameters. The likelihood function for the inhomogeneous estimator can be written in terms of the Doppler measurement vector  $\tilde{\omega}$  and the emitter parameters  $\theta$  as

$$f_{\tilde{\omega}}(\tilde{\omega}|\theta) = \left( \frac{1}{\pi^P |\mathbf{R}_{\omega}|} \right) e^{-\left( \tilde{\omega} - \omega(\theta) \right)^H \mathbf{R}_{\omega}^{-1} \left( \tilde{\omega} - \omega(\theta) \right)} \quad (5.18)$$

for the simplified case where the time-delay and azimuth errors can be ignored.

The fact that the two estimators can be shown to be identical when the scattering is the same underscores the fact that most of the observations that were made in Section 5.2.2 also apply for this estimator. That is, this estimator will show the same dependence on emitter velocity, SNR, etc., as the estimator for the homogeneous clutter model did.

For the second example, we use the same scatterer SNR and delay as the previous example, but select the azimuth of the scatterers from a uniform random distribution between  $\pm 45$  degrees. The result is shown in Figure 5.10 and exhibits considerable improvement over the previous case. This performance improvement is also related to GDOP. That is, if we consider each scatterer to be a virtual sensor, then better performance is achieved by spreading the sensors over the terrain than by combining them to a line at a particular azimuthal angle.

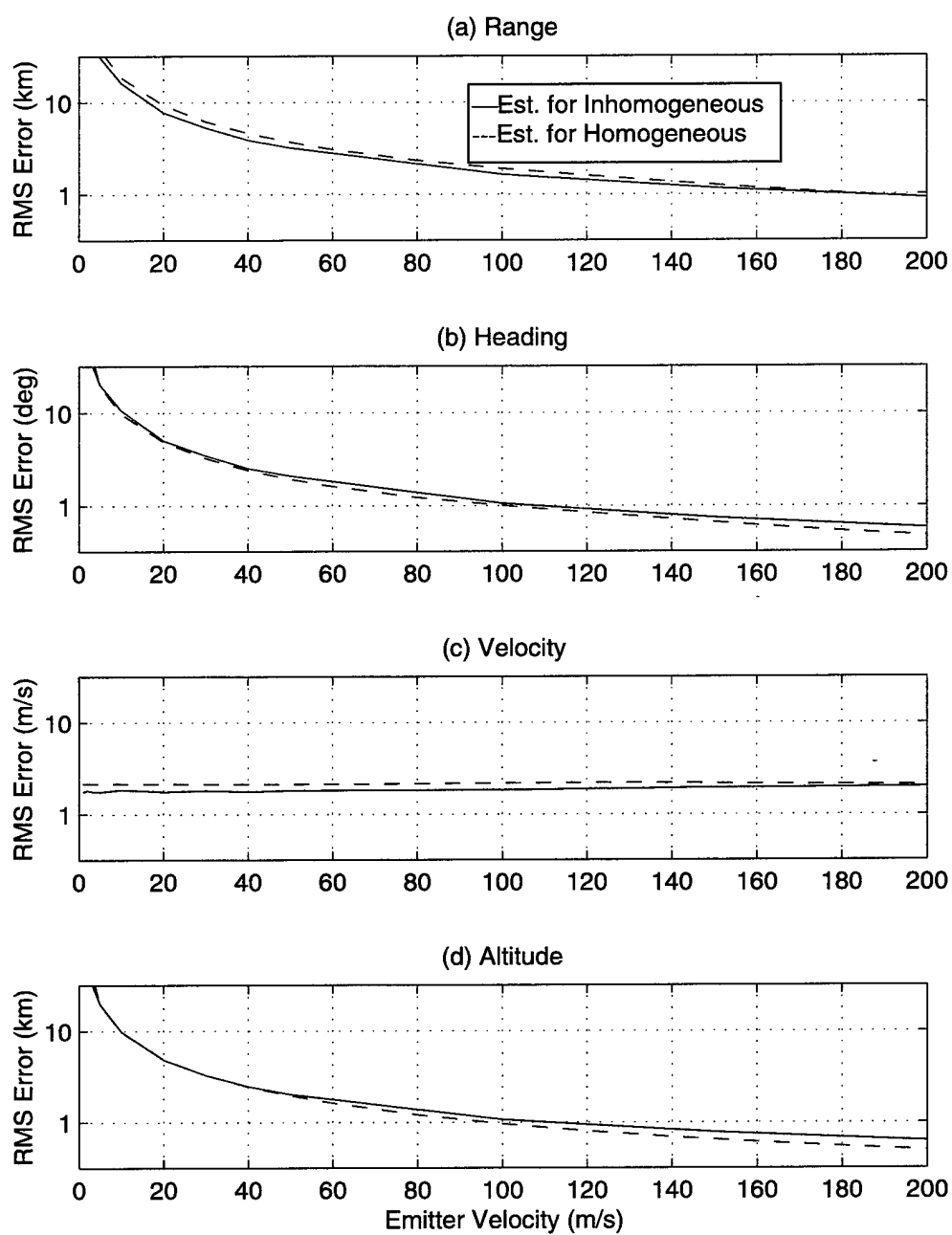


Figure 5.9. CRLB for the two estimators are equivalent for the same scattering scenario.



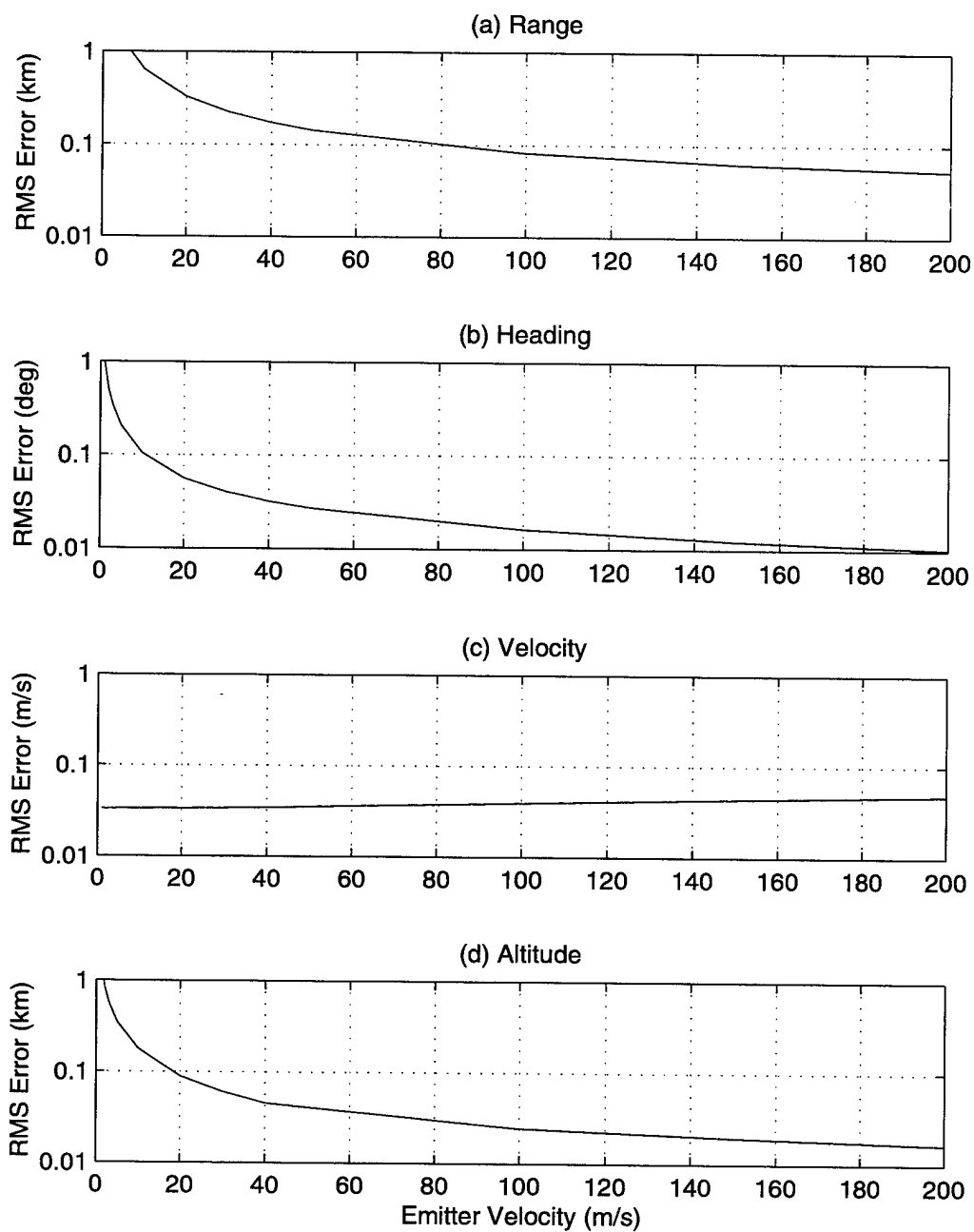


Figure 5.10. CRLB versus velocity for 50 scatterers speed in azimuth from  $-45$  to  $+45$ .

### 5.3.2 Monte-Carlo Simulation

A Monte-Carlo simulation was performed for the previous example where the scatterer azimuth was selected from a uniform distribution. The scatterer parameters of delay, Doppler, and azimuth were corrupted from their true values by additive noise with variance equal to the CRLB expressions of (5.14)–(5.16). The results are shown in Figure 5.11. As expected, the estimates are unbiased and match the theoretical variances.

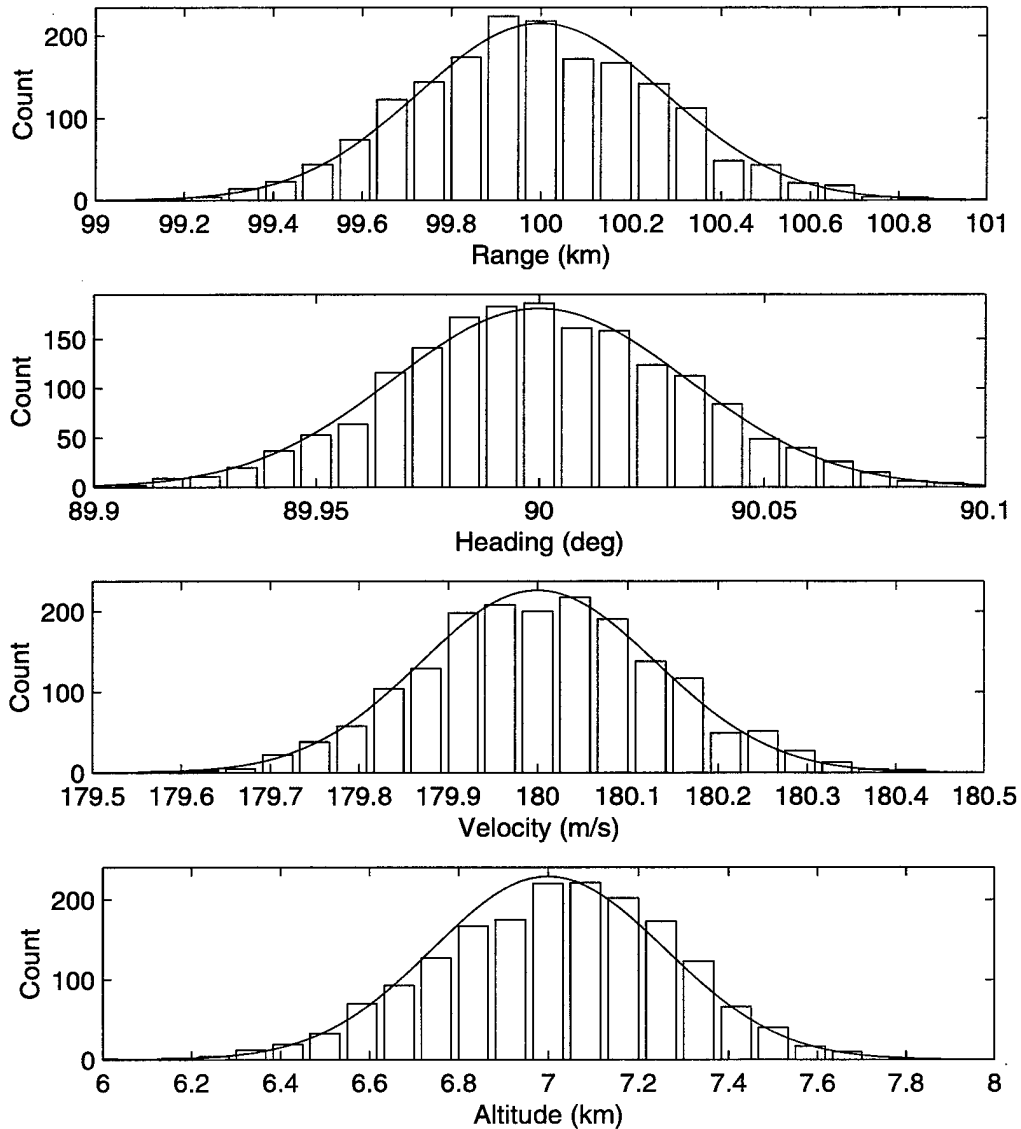


Figure 5.11. Histograms for 1700 simulations. The mean of the simulations equal 99.991 km, 90.000 deg., 180.005 m/s, 7.015 km for range, heading, velocity, and altitude, respectively. The solid curve represents the theoretical PDF based on the CRLB calculations.

## 5.4 APPLICATION OF CRLB TO REAL DATA

Sections 5.2 and 5.3 contained theoretical bounds calculations based on homogeneous and inhomogeneous clutter assumptions. An important question is whether or not these bounds apply to parameter estimates obtained using experimental field data. The answer depends on the capabilities of the receiver and the scattering properties of the terrain. We now consider the two estimators separately.

The statistical formulation used for the estimator for homogenous clutter assumed narrow receive beams and closely spaced delay cells. This permitted the use of a single Doppler term to describe the scattered signal from each delay-azimuth cell. For nonzero beamwidth and delay cells, some Doppler dispersion will be present and this will reduce the performance of the estimator from the theoretical results. Another factor that could reduce performance of this estimator is the clutter itself. If the clutter is not homogeneous, but instead contains large clutter discretely, emitter energy could enter the filter via the beam edges and sidelobes. The effect of this energy would be to increase the apparent noise floor and thereby reduce the performance of the estimator.

The key assumption for the inhomogeneous clutter estimator is that the clutter behaves as a collection of independent discrete scatterers. We assumed that we could estimate the scatterer parameters as well as we can estimate point radar targets. This model will be violated somewhat by clutter that is more homogeneous in nature. In that case, the dominant scatterers could possess more spatial extent and be spread in any combination of delay, azimuth, or Doppler. The parameter estimates for extended scatterers will have larger errors than point scatterers with equivalent SNR.

The factors described above can be thought of as modeling error. That is, our models do not describe the physical problem completely. The signal components resulting from modeling error is considered model noise. Thus the total noise  $g$  is the sum of the receiver thermal noise  $g_r$  and the model noise  $g_m$ . This will be discussed further in Chapter 6 where we shall see that the model noise for the Mountaintop system parameters is 10-20 dB for the homogeneous model and less than 10 dB for the inhomogeneous model. The difference in the levels of model noise for these two models suggests that the WSMR terrain is more inhomogeneous than homogeneous. Nevertheless, we shall see in the next chapter that both estimators will successfully localize real emitters contained in Mountaintop data collected at WSMR.

## 5.5 CHAPTER SUMMARY

The theoretical performance of the two estimators designed in Chapters 3 and 4 was determined in this chapter. The behavior of the bounds was considered for a number of localization scenarios. The two estimators were demonstrated to be equivalent for identical scattering scenarios. Monte-Carlo simulations were provided to substantiate the localization and bounds calculations. In the next chapter we will utilize these techniques with Mountaintop field data.

## 6. APPLICATION TO MOUNTAINTOP DATA

### 6.1 INTRODUCTION

In this chapter we use the estimators developed thus far to localize several airborne emitters contained in Mountaintop field data. This data was collected at White Sands Missile Range (WSMR) where the terrain is a mixture of desert and mountains. Both the estimator for homogeneous clutter and the estimator for inhomogeneous clutter will be used. Estimation errors obtained with real data will be compared to the CRLB when appropriate. This chapter will serve to demonstrate the techniques presented in the previous three chapters.

The Mountaintop system was described briefly in Chapter 2. A photograph of the antenna and the airborne emitter is shown in Figure 6.1. For the localization work presented here, the antenna was rotated 90 degrees to the horizontal polarization mode referred to as RSTER-90. In this mode, the antenna supports adaptability in the azimuthal dimension. Thus, once the data for each element have been recorded, receive beams can be formed in any or all directions simultaneously. The emitter contains dipole antennas



*Figure 6.1. Photograph of Mountaintop installation and Lear jet emitter at North Oscura Peak, NM.*

in the nose and tail portions of the airplane. The radiation patterns for these dipole antennas are fairly broad. The nose antenna is used when the emitter is flying inbound toward the receiver and the tail is used when flying outbound away from the receiver. The location of the receiver and the emitter for several data sets is shown in Figure 6.2. The emitter's ranges vary from 78.3 km for HOT-6161 to 212 km for HOT-6132. Additional information on the Mountaintop system and experiments can be found in [6],[7],[9].

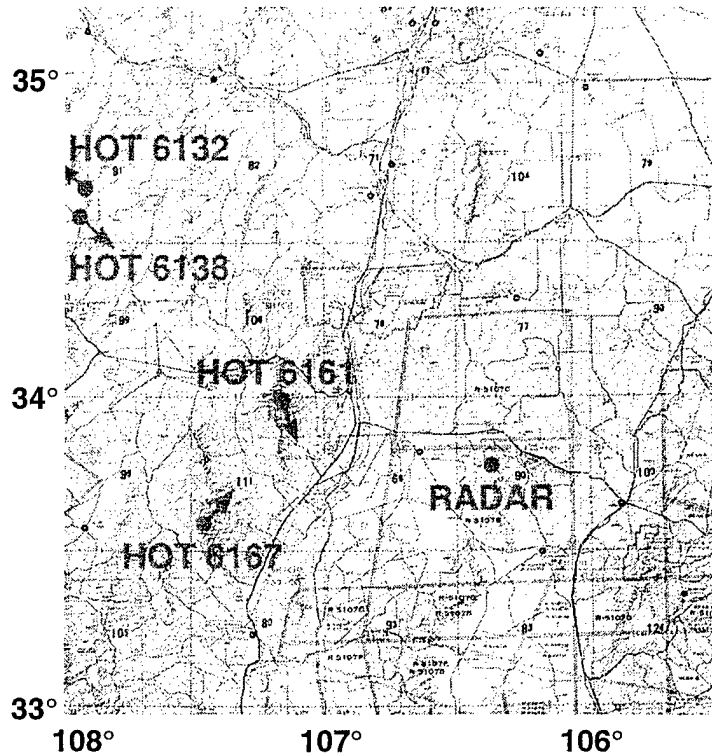


Figure 6.2. Map showing Mountaintop radar site and location of emitters.

Three emitters will be localized using the two estimators. The data sets are referred to as HOT-6067, HOT-6161, and HOT-6132 and were collected on April 6, 1994 for the purposes of studying terrain scattered interference [72]. The estimator for homogeneous clutter will be employed in Section 6.2 and the estimator for inhomogeneous clutter will be employed in Section 6.3. In Section 6.4 we consider the case of reduced emitter power and bandwidth. We summarize the results of this chapter in Section 6.5.

## 6.2 RESULTS USING THE ESTIMATOR FOR HOMOGENEOUS CLUTTER

### 6.2.1 Data Set HOT-6067

The first real emitter to be localized using out-of-plane multipath was that of data set HOT-6067. This emitter was located 101.7 km west of RSTER traveling northeast at a velocity of 184.5 m/s. The engagement geometry is shown in Figures 6.2 and 6.3. The true emitter parameters were obtained from a GPS receiver located on board the Lear jet. The emitter azimuth was determined by selecting the peak of a conventional (nonadaptive) beamformer and found to be within about 0.1 degrees of that indicated by the GPS. The coordinate system used to describe emitter position in this chapter is shown in Figure 6.4. This coordinate system measures angles relative to the receiver boresight. The full three-dimensional coordinate system, including emitter altitude, is shown in Appendix C.

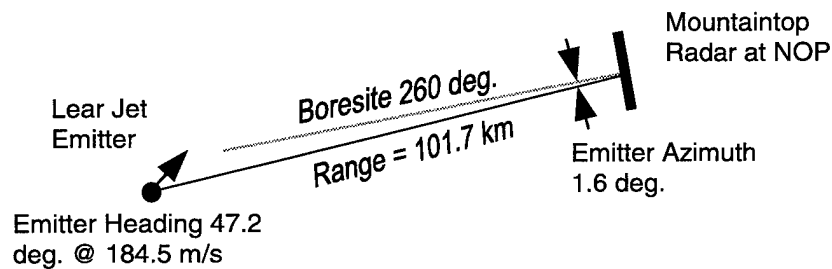


Figure 6.3. Geometry for data set HOT-6067. Emitter heading and Mountaintop boresight are given in degrees relative to true north.

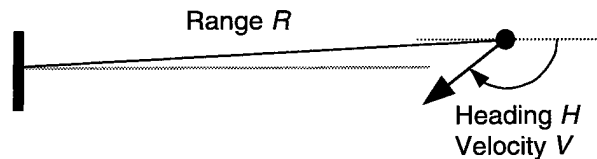


Figure 6.4. Emitter parameter estimates of heading and velocity are determined relative to the receive antenna boresight.

The general estimator described in Chapter 3 specifies that multiple receive beams be used to localize an emitter. However, for this case, a single beam was all that was required. (This is a function of the emitter parameters, in particular, the emitter heading.) The localization filter used 75 taps spaced by 4

$\mu$ s with data selected from a 75 ms coherent processing interval (CPI). The receive beam was pointed to  $-42$  degrees which is out in front of the emitter. A four-dimensional grid search was performed over the emitter parameters of range, heading, velocity, and altitude. Prior to performing the grid search, the data are first passed through a 3-tap version of the filter to cancel the emitter signal entering the receive beam via the antenna sidelobes. Strictly speaking, only one tap should be required for such a sidelobe canceller. The additional taps are used to cancel the strong multipath signals that originate from the glistening surface and from scatterers very close to the receiver.

The output of the four-dimension search is the four-dimensional log-likelihood function (with coordinates of range, heading, velocity, and altitude) that we desire to maximize. To visualize this surface, we show several cuts or slices through it. The range-heading-velocity cut is shown in Figure 6.5. For this cut, the altitude estimate was fixed at 7.7 km which corresponds to the peak of the likelihood function. We see a single dominant peak near the true emitter parameters and some smaller peaks and other structure throughout. A range-altitude slice through the likelihood function is shown in Figure 6.6. The emitter heading and velocity were fixed at the values corresponding to the likelihood peak. The one-dimensional cuts through the peak are shown in Figure 6.7 (a)–(d), respectively, for range, heading, velocity, and altitude. The dashed lines denote the true emitter parameters.

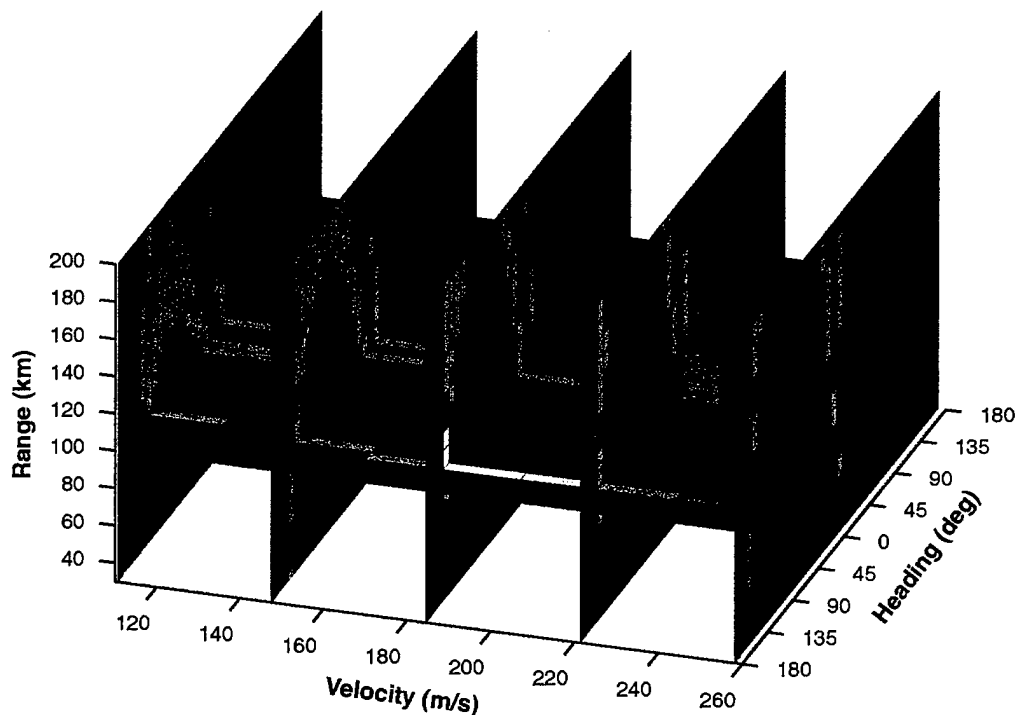


Figure 6.5. 3-D log-likelihood function for HOT-6067 at a fixed altitude.

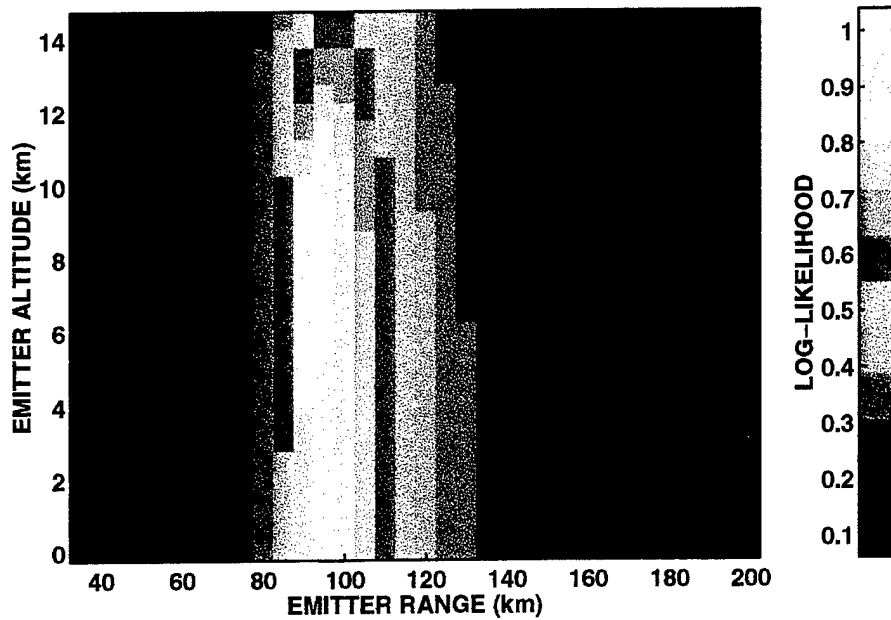


Figure 6.6. Range-altitude slice for fixed heading and velocity.

The localization results are listed in Table 6.1 along with the true parameter values and the estimation errors. The errors are listed by their actual value and in terms of the CRLB derived in Chapter 5. One can argue that if the estimation errors are less than  $4-5 \sigma$ , then we are operating close to the CRLB. Hence, for this example, we have far exceeded the CRLB for range and heading estimates. However, we had pointed out in Section 5.4 that the CRLB was developed based on the assumption that the data match the model perfectly. That is, the clutter is homogenous (without clutter discreties) and described by a constant gamma clutter model. Different values of gamma will produce different CRLB. We also assumed that the energy scattered by each delay-azimuth cell is modulated by a single Doppler shift term. The presence of clutter discreties in the beam edges, or Doppler dispersion due to the extended nature of the scattering cells, will produce model noise. We will see in Section 6.4 that it is possible to determine the amount of model noise present by observing the residual noise level at the output of the localization filter when it is operating with the correct emitter parameters. For this data set, the model noise was found to be 20 dB above the receiver thermal noise. A 20-dB increase in noise increases the CRLB RMS error calculations by 10 dB and thus all the estimates are within  $3\sigma$  of the true values.



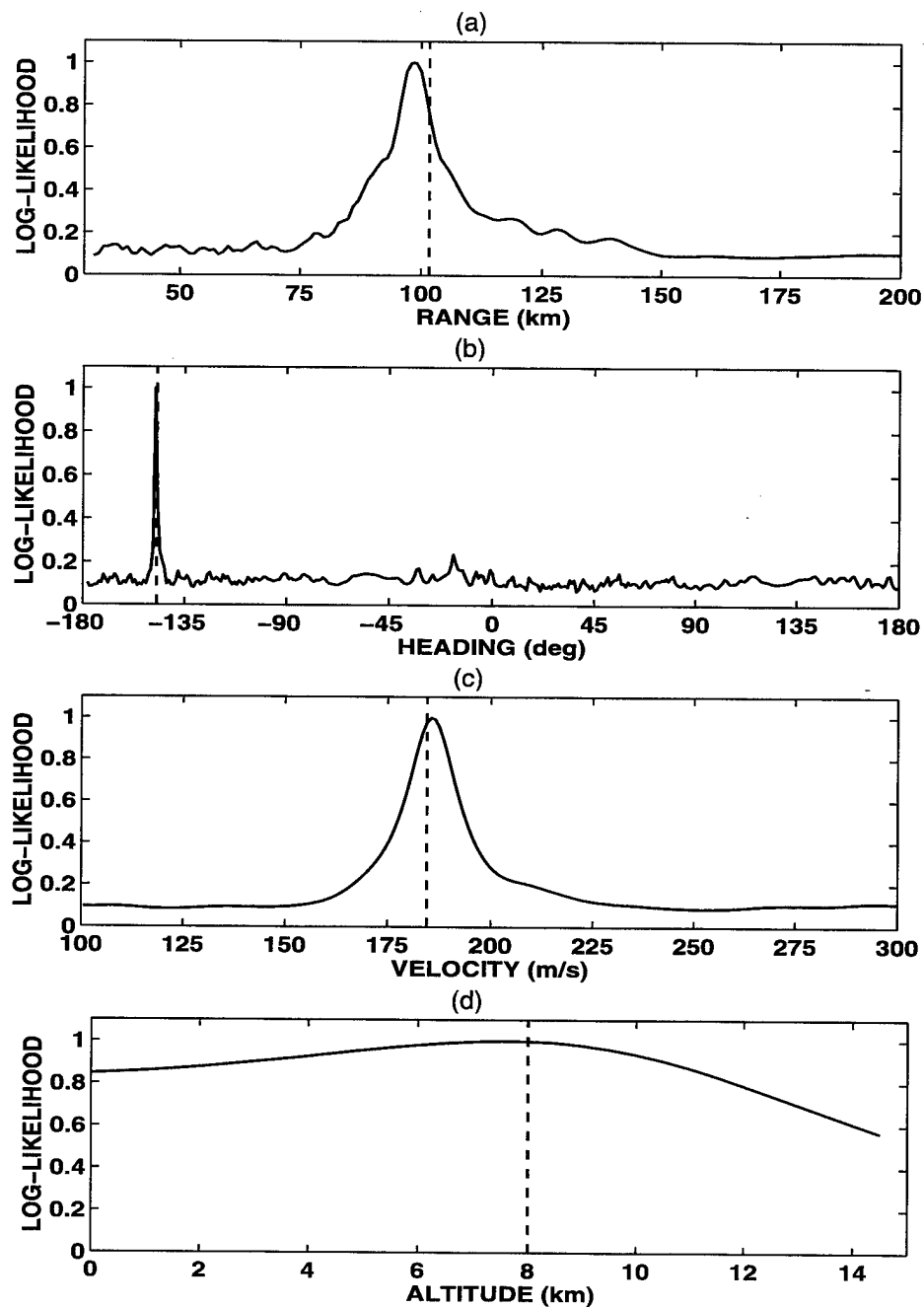


Figure 6.7. Slices through the four-dimensional log-likelihood function at the emitter (a) range, (b) heading, (c) velocity, and (d) altitude. The dashed lines denote the true parameter values obtained via GPS.

**TABLE 6.1**  
**Estimation Results for Data Set HOT-6067**

Emitter Parameter	True Value	Estimated Value	Error		CRLB $\sigma$
			Value	CRLB	
Range (km)	101.7	97	4.7	$22\sigma$	0.21
Heading (deg)	-147.2	-149.5	2.3	$29\sigma$	0.078
Velocity (m/s)	184.5	185.5	1.1	$2.2\sigma$	0.5
Altitude (km)	8	7.7	.3	$2.7\sigma$	0.11

### 6.2.2 Data Set HOT-6161

The next data set we will examine is HOT-6161. The position of the emitter was shown in Figure 6.2. For this data set, the emitter was flying very low through an area known as Milligan Gulch. The point of the Milligan Gulch experiment was to try to deny the receiver the direct-path line-of-sight signal in order to stress TSI mitigation algorithms that rely on the direct path signal. The emitter altitude varied from 500 to 1000 feet above the ground but the direct-path signal was not severely attenuated (probably due to diffraction).

For this data set, we use several beams to perform the localization. The emitter power versus azimuth is shown in Figure 6.8. The conventional nonadaptive beamformer and MVDR (*minimum variance distortionless response*) [4],[73] beamformer are both used. The conventional beamformer is useful for measuring the SNR of the emitter direct path signal but fails to measure the emitter multipath power at other angles due to the high sidelobes. Conversely, the MVDR spectrum captures the multipath signal versus angle but fails to measure the power in the emitter direct path. The later point is probably due to small system calibration errors or the correlation in the multipath signals or some combination of both of these effects.

Five receive beams were formed to collect emitter multipath energy. The beam azimuths are given by the vertical lines in the figure. These beams were selected because they correspond to higher than average emitter multipath. Cuts through the likelihood functions for each beam are shown in Figure 6.9(a) and (b) for altitude and range, respectively. The altitude cuts have been normalized for unity peak in the likelihood function while the relative magnitude of the range cuts has been preserved. The largest peak is from the 62-degree beam while the shortest peak is from the 20-degree beam. Part (b) of the figure shows that all beams produce peaks near the correct emitter range. In part (a) we see that all beams produce a peak (albeit broad) near the true emitter altitude.

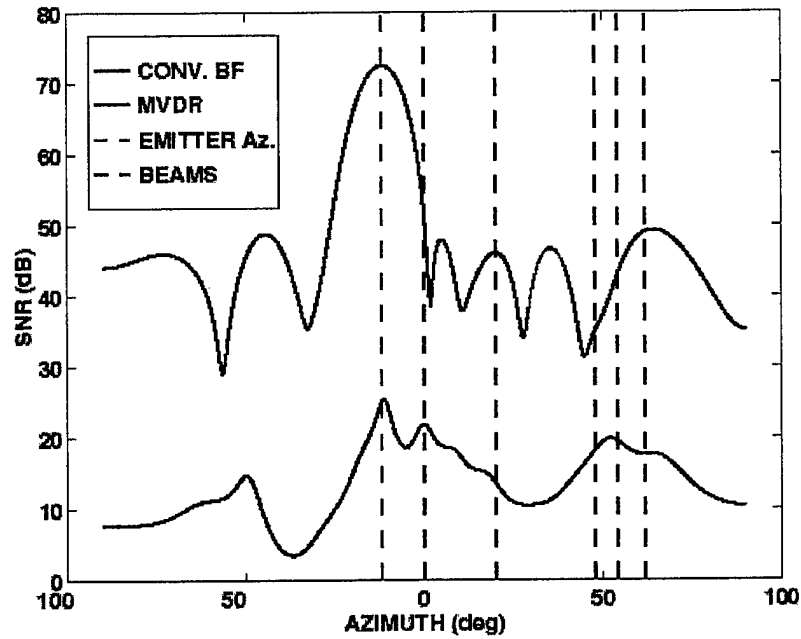


Figure 6.8. Emitter SNR versus receiver azimuth for HOT-6161 using conventional and MVDR beamformers. Emitter and beam azimuthal angles are shown as vertical lines.

The final estimates are taken by forming the sum (or mean) of the individual likelihood functions for the five beams. The emitter range-heading slice is shown in Figure 6.10 and the estimated quantities and estimation errors are listed in Table 6.2.

**TABLE 6.2**  
**Estimation Results for Data Set HOT-6161**

Emitter Parameter	True Value	Estimated Value	Error	
			Value	%
Range (km)	78.3	83.0	4.7	6%
Heading (deg)	121.8	122.1	0.3	0.25%
Velocity (m/s)	134.3	139	4.6	3.6%
Altitude (km)	0.5	0	0.5	—

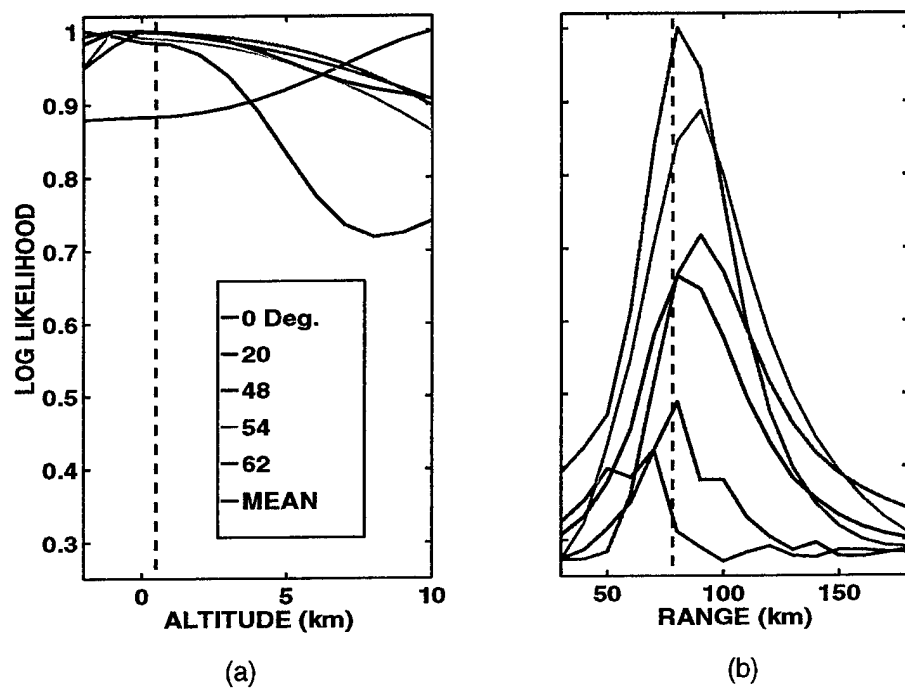


Figure 6.9. (a) Altitude and (b) range cuts through the log-likelihood functions for five multiple beams. (Data set HOT-6161.)

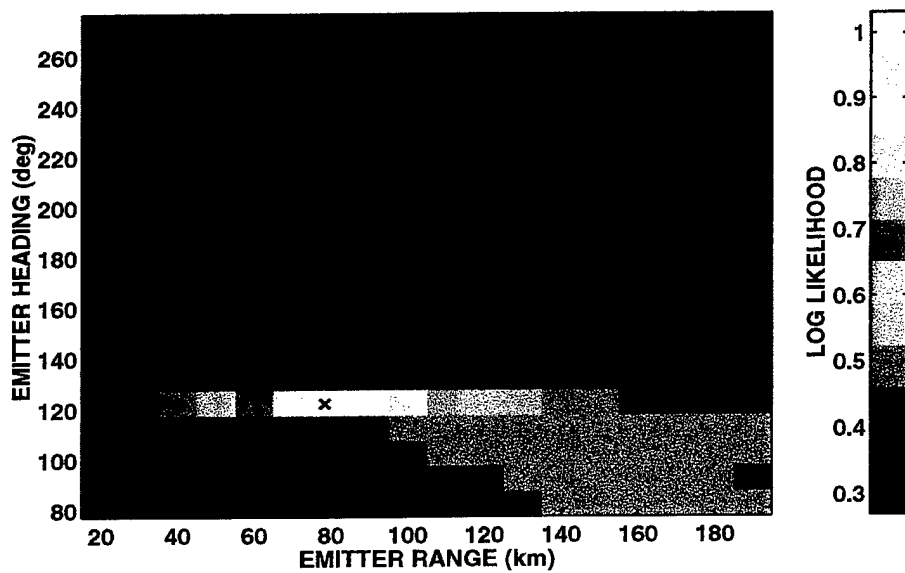


Figure 6.10. Range-heading slice through four-dimensional log-likelihood function for HOT-6161.

### 6.2.3 Data Set HOT-6132

Several additional data sets were localized with results similar to the previous two sections. The third data set discussed in this chapter is HOT-6132. This set is of particular interest because the estimator successfully used above fails to localize this emitter. The range for this emitter is 212 km and the geometry was shown in Figure 6.2.

Ten evenly spaced receive beams were formed covering from  $-60$  to  $+60$  degrees of azimuth. The range cuts for the ten beams are shown in Figure 6.11. We can see four or five peaks close to the true emitter range but no consensus between the results and hence this localization technique has failed in this case.

The principal cause for this failure is evident in the delay-Doppler map shown in Figure 6.12. The solid line represents the delay-Doppler ridge for the  $-60$  degree beam and the dashed lines denote the  $\frac{1}{2}$  power points. For this case, there is clearly a great deal of Doppler spread across the beam at any given delay. For example, at  $200 \mu\text{s}$ , the spread covers over 100 Hz while the Doppler resolution is only 6.5-19.5 Hz depending upon the length of the coherent processing interval (CPI). Multipath signals originating off the ridge by more than one half the reciprocal of the integration time will essentially be decorrelated from the Doppler modulator in the filter and will not produce a peak in the likelihood function. Instead, these signals manifest themselves as increases in the noise level. Also evident in the figure is the general inhomogeneous nature of the bistatic clutter for this beam. While some of the energy is confined to the delay-Doppler ridge, there is some strong scattering outside of the ridge that is picked up by the beam edges. (The null-to-null beamwidth of this beam is close to 40 degrees.) There is also a very strong scatterer located at  $15 \mu\text{s}$  that produces significant delay sidelobes. All of these factors reduce the effectiveness of this filter to the point where it did not produce the correct estimate.

There are several possible ways one could try to improve this situation. One approach would be to build an antenna with a narrower beamwidth. If, for example, a 1-2 degree wide beam could be formed, this narrow beam would act to confine the energy to the Doppler ridge and reduce Doppler dispersion. Another approach to capture the Doppler spread is to add several Doppler modulators per delay cell. This would increase the dimensions of the filter and thereby increase the computational burden. Another possible approach could be to reduce the integration time and thereby decrease the Doppler resolution. However, we saw in Chapter 5 that localization performance is proportional to the cube of the integration time.

Instead of trying to fix this estimator that was designed to work in homogeneous clutter, we now switch to the estimator designed for inhomogeneous clutter. The clutter inhomogeneities that caused problems for the estimator used in this section will promote more accurate results for the estimator used in the next section.

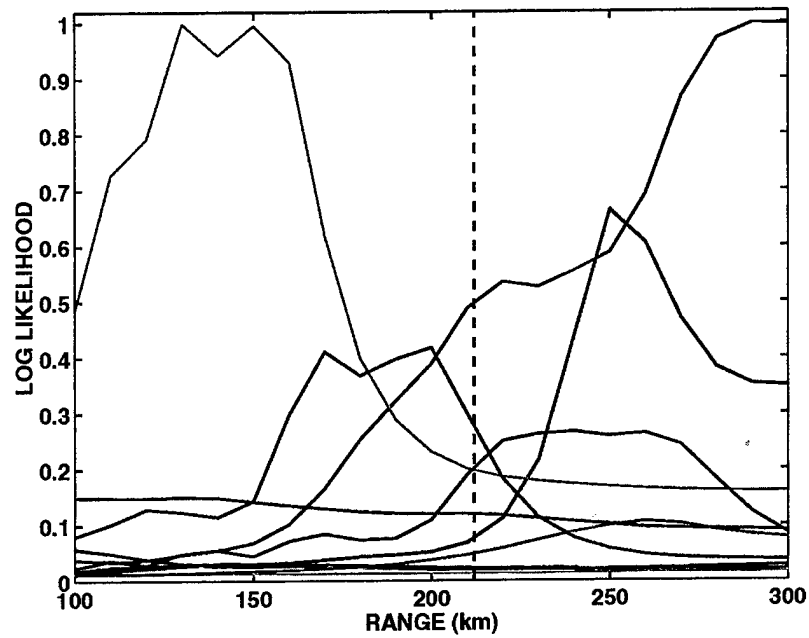


Figure 6.11. Multiple range cuts through log-likelihood function for HOT-6132. Localization is unsuccessful.

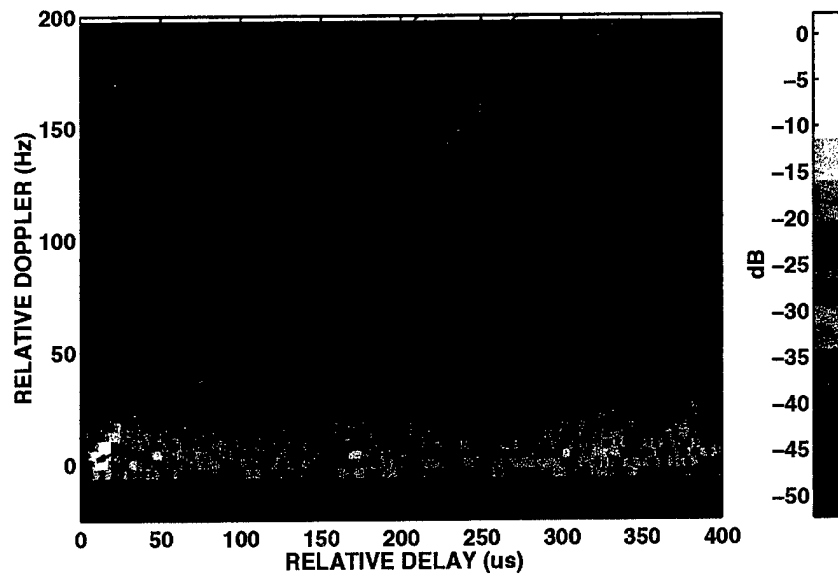


Figure 6.12. Delay-Doppler map shows wide Doppler spread across (-60 deg) beam.

### 6.3 RESULTS USING THE ESTIMATOR FOR INHOMOGENEOUS CLUTTER

In this section we demonstrate the estimator that was designed for inhomogeneous clutter using the same three data sets examined in the previous section. We shall see that this estimator performs better than the estimator described above. This is probably due to the general inhomogeneous nature of the bistatic clutter at WSMR.

The estimator designed for inhomogeneous clutter is a two-part procedure where first the scatterer parameters are estimated and then the emitter parameters are estimated. The basic ML estimator for scatterer parameters was shown in Figure 4.2. This structure requires that we search for scatterers over all angles, delays, and Doppler bins. The practical implementation of this scatterer parameter estimator is shown in Figure 6.13. Cross-correlations were performed for the direct path and thirty-three beams ranging from  $-64$  to  $64$  degrees. In this manner, a three-dimensional cube of scattered energy versus delay, Doppler, and azimuth is formed. These correlation cubes have been generated in the past by Gabel [66]. The cube is passed to the "Select and Centroid Scatterers" box which applies a threshold and centroids the results to a set of discrete scatterer parameter vectors  $\hat{\mathbf{D}}$ ,  $\hat{\omega}$ ,  $\hat{\phi}$ , and  $\hat{\mathbf{S}}/\hat{\mathbf{N}}$ . The threshold is set significantly high so that false alarms are essentially nonexistent.

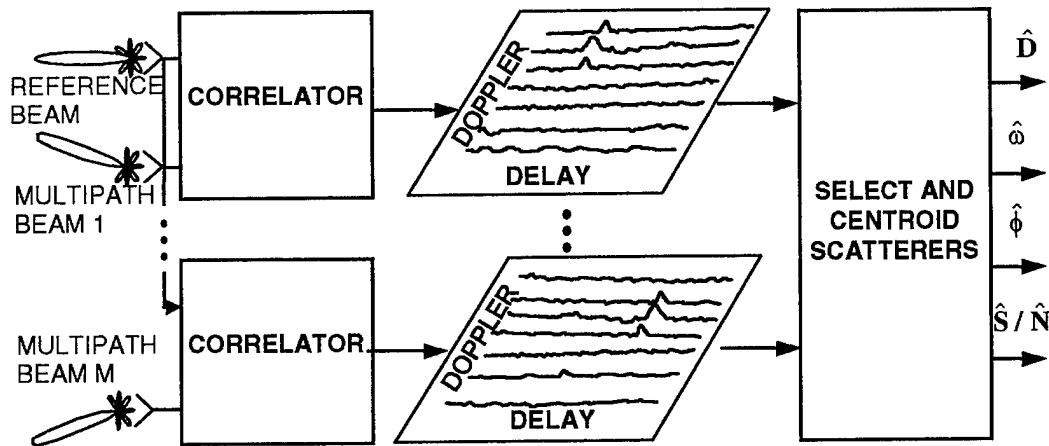


Figure 6.13. Estimator for scatterer parameters of delay, Doppler, azimuth, and SNR.

Some of the problems the "Select and Centroid Scatterers" box has to contend with are depicted in Figure 6.14. This figure shows a delay-Doppler map for a typical multipath beam. In the map one can see sidelobes in all three dimensions of delay, Doppler, and azimuth. This box rejects sidelobes by selecting only the largest scatterer for each delay, Doppler, and azimuth dimension.

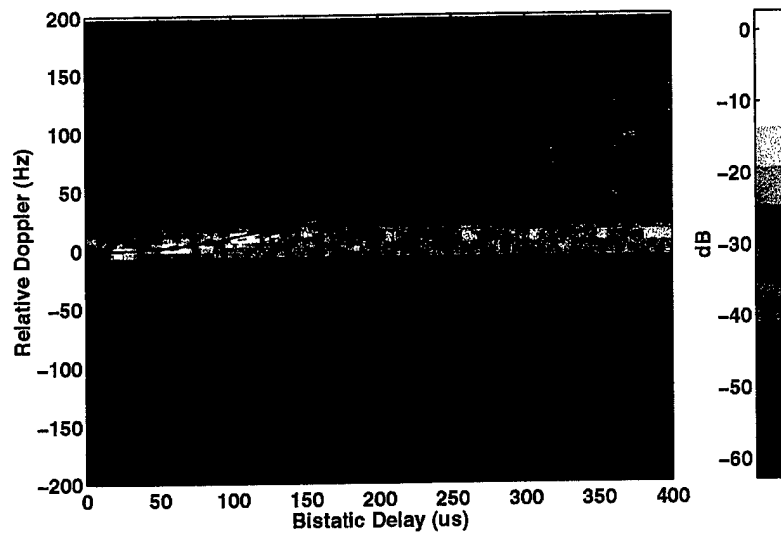


Figure 6.14. Delay-Doppler map showing energy in the delay, Doppler, and azimuth sidelobes. The delay sidelobes are the horizontal bands of energy and the Doppler sidelobes are vertical bands. Scatterers outside of the dashed lines are off of the delay-Doppler ridge and are therefore in the beam's edges or sidelobes.

Another potential problem is that estimates for closely spaced discrete scatterers that are not separated by several resolution cells in delay, Doppler, or azimuth, may be biased due to coherent interference. This is depicted graphically in Figure 6.15 and is independent of SNR. Scatterer parameter errors of this nature are not accounted for in the scatterer CRLB computations and therefore the bounds calculations will be optimistic. However, as we shall see below, this estimator produces fairly accurate parameter estimates that are close to the CRLB in several cases.



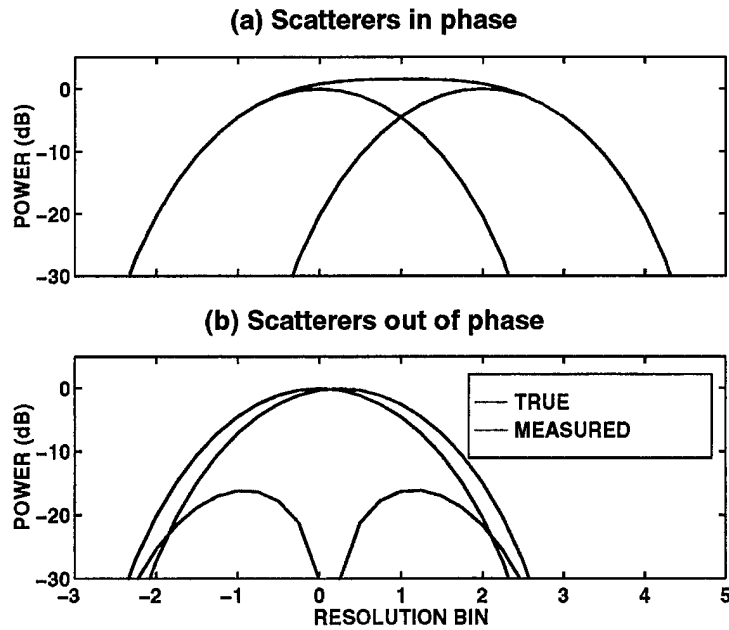


Figure 6.15. Examples of errors produced by closely spaced scatterers. True system responses and measured responses for (a) in-phase and (b) out-of-phase combinations are shown. The two in-phase scatterers merge into a single extended scatterer while the out-of-phase scatterers seem to “repel” each other.

### 6.3.1 Data Set HOT-6067

The scatterer estimates for HOT-6067 are shown in Figure 6.16. The three-dimensional cube is collapsed to azimuth-delay in part (a) and azimuth-Doppler in part (b). The location of each scatterer or scattering center is denoted by an ‘x’. Short-delay scatterers ( $< 10 \mu\text{s}$ ) and scatterers within a beamwidth or so of the emitter azimuth are not used. These are believed to be biased by the strong direct path signal. The total number of scatterers used for the localization of this data set is 67.

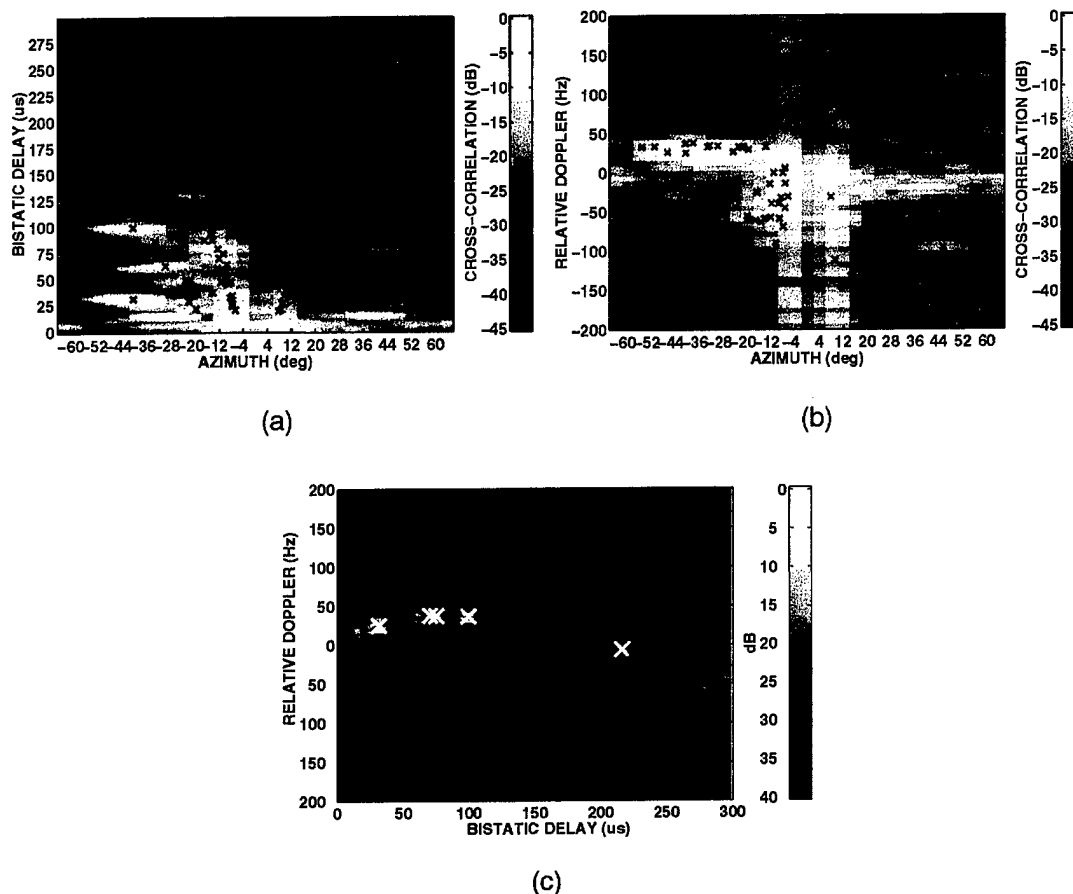


Figure 6.16. Cross-correlation plots for HOT-6067. Part (a) shows correlation vs. time, part (b) shows correlation vs. Doppler, and part (c) shows correlation vs. delay and Doppler for a single beam at  $-40$  degrees. The position of each scatterer is denoted by an "x."

With the scatterer parameters estimated, we are now ready to estimate the emitter parameters. A coarse least-squares search using Equation (4.18) is performed over emitter range, heading, and velocity for a nominal fixed altitude. The range-heading slice is shown in Figure 6.17. The coarse search is performed to provide an initial guess at the emitter parameters. This initial guess is used as the starting point for the iterative procedure described in Section 4.3.4. We found that it was not necessary to include emitter altitude in the coarse search. The iterative procedure converged to the same point regardless of the initial starting altitude.

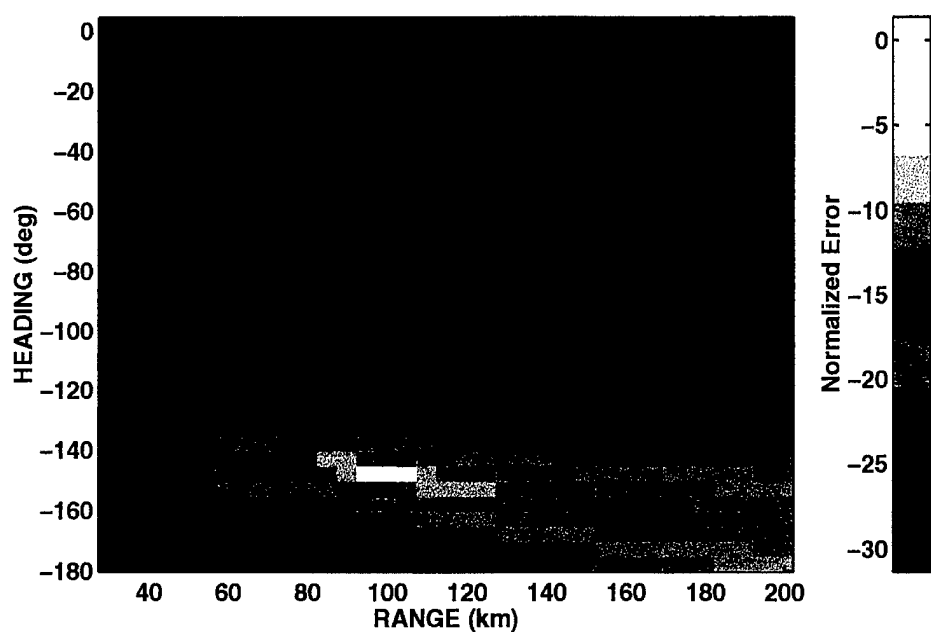


Figure 6.17. Least-squares search through parameter space for HOT-6067.

The iterative procedure converged rapidly to the estimates listed in Table 6.3. Only five iteration steps were required. The results are excellent and are fairly close to the CRLB for all parameters except the emitter velocity. The range error is only 0.7 km and the heading error is only 0.2 degrees.

**TABLE 6.3**  
**Results for Data Set HOT-6067**

Emitter Parameter	True Value	Estimated Value	Error		CRLB $\sigma$
			Value	CRLB	
Range (km)	101.7	101.0	-0.7	$2.3\sigma$	0.31
Heading (deg)	-147.2	-147.0	0.2	$4\sigma$	0.05
Velocity (m/s)	184.5	179.3	5.2	$11.1\sigma$	0.47
Altitude (km)	8	9.4	1.4	$4.5\sigma$	0.31

### 6.3.2 Data Set HOT-6161

The same approach was used for data set HOT-6161 with the same excellent results. The number of scatterers used in the localization was 61 and the localization results are listed in Table 6.4. As with the previous case, these estimates are reasonably close to the CRLB. This fact suggests the inhomogeneous model contains less model noise and/or estimation biases than the homogeneous model when applied to WSMR terrain. Model noise will be discussed further in Section 6.4.

**TABLE 6.4**  
**Results for Data Set HOT-6161**

Emitter Parameter	True Value	Estimated Value	Error Value CRLB		CRLB $\sigma$
Range (km)	78.3	78.1	0.2	$0.8\sigma$	0.24
Heading (deg)	121.8	121.9	0.1	$3.3\sigma$	0.03
Velocity (m/s)	134.3	134.9	0.6	$3.5\sigma$	0.17
Altitude (km)	0.5	-0.24	-0.74	$1.6\sigma$	0.46

### 6.3.3 Data Set HOT-6132

Data set HOT-6132 is of particular interest because the estimator for homogeneous clutter failed to localize the emitter. One of the reasons this estimator failed is the inhomogeneous nature of the clutter in this data set. Hence we expect the performance of the estimator of inhomogeneous clutter to exceed that of the estimator for homogeneous clutter for this case.

Eighty scatterers were used for the localization of this data set. The results of the coarse search are shown in Figure 6.18. A single, well-defined peak is present in the figure. Hence this estimator has successfully localized this emitter and the results are listed in Table 6.5. The CRLB for this case are small because of the large number of strong scatterers used for the localization. The estimation errors in terms of CRLB are quite large compared to the previous two examples. With the exception of altitude, the localization errors themselves are not very large, however. For example, the range error is only 3% but the 18.4-km (60,000 feet) altitude estimate is off by more than 10 km.

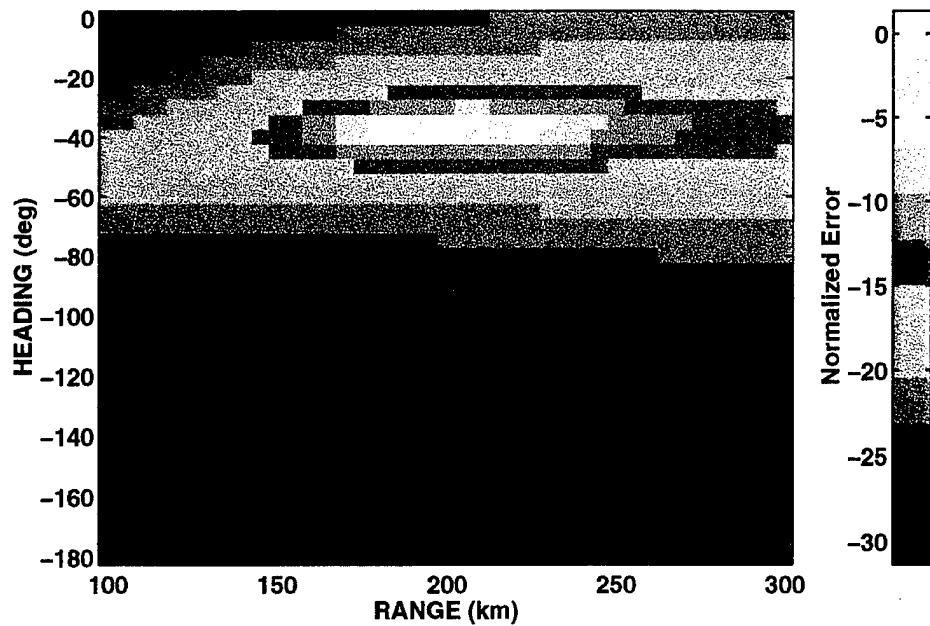


Figure 6.18. Least-squares search through range-heading parameter space for HOT-6132.

**TABLE 6.5**  
**Results for Data Set HOT-6132**

Emitter Parameter	True Value	Estimated Value	Error		CRLB $\sigma$
			Value	CRLB	
Range (km)	211.9	218.6	6.7	$29\sigma$	0.23
Heading (deg)	-36.2	-36.7	-0.5	$70\sigma$	0.007
Velocity (m/s)	142.1	150.5	8.4	$42\sigma$	0.2
Altitude (km)	8	18.4	10.4	$42\sigma$	0.25

In an attempt to reduce the estimation errors for this data set, the localization was repeated for one fewer scatterer. The localization was performed 80 times while the contribution of each of the 80 scatterers was omitted one at a time. The set of 79 scatterers that resulted in the lowest altitude estimate was selected as the new estimate. The idea was that perhaps one of the scatterer estimates was severely biased by the coherent interference effect that was shown in Figure 6.15, and that omitting the scatterers, one at

a time, would isolate the bad scatterer. The new estimates are shown in Table 6.6. The range estimate is now within the CRLB and the remaining parameter estimates have improved as well. The scatterer that was removed had an SNR of 44 dB which was the tenth largest. The errors are still larger than for the previous two data sets, however.

Another possible explanation for the increased errors in this example could be that the flat-earth assumption is being stressed for this longer range case. Also, perhaps more than one scatterer estimate is biased by the coherent interference effect.

**TABLE 6.6**  
**Results for Data Set HOT-6132 With One Scatterer Removed**

Emitter Parameter	True Value	Estimated Value	Error		CRLB $\sigma$
			Value	CRLB	
Range (km)	211.9	212.3	0.4	$1.7\sigma$	0.23
Heading (deg)	-36.2	-36.6	-0.4	$56\sigma$	0.007
Velocity (m/s)	142.1	145.6	3.5	$17.5\sigma$	0.2
Altitude (km)	8	12.0	4	$16\sigma$	0.25

#### 6.4 RESULTS FOR REDUCED EMITTER POWER AND BANDWIDTH

We have demonstrated thus far the ability to localize a strong 700 W emitter<sup>1</sup> in a fairly strong clutter environment. What about low-power emitters or weaker clutter? The results presented in Chapter 5 suggest that it should be possible to localize emitters with much lower signal-to-noise ratios. To investigate this further we have computed the theoretical performance limits as a function of both emitter power and clutter strength. We considered a geometry similar to the HOT-6067 data set and assumed that all the energy scattered from the shaded portion of Figure 6.19 could be collected and processed optimally. The result is shown as two lines in Figure 6.20. These are loci of constant performance as a function of emitter SNR and average scattering strength.

Mountaintop parameters are indicated as a point in Figure 6.20. This is the theoretical point which assumes that the models are perfect. In practice, the model error will slide this point to the right somewhat. Nevertheless, there is plenty of room for the localization of much weaker emitters.

<sup>1</sup> The emitter power is 2 kW over 600 kHz but only 700 W is in the receiver passband of 200 kHz.

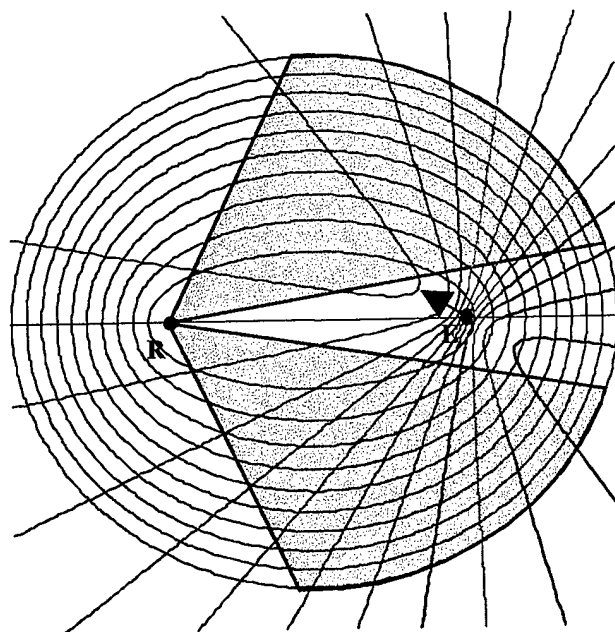


Figure 6.19. Delay-Doppler contours for the multiple-beam bounds calculation. The area that is shaded is included in the CRLB calculation.

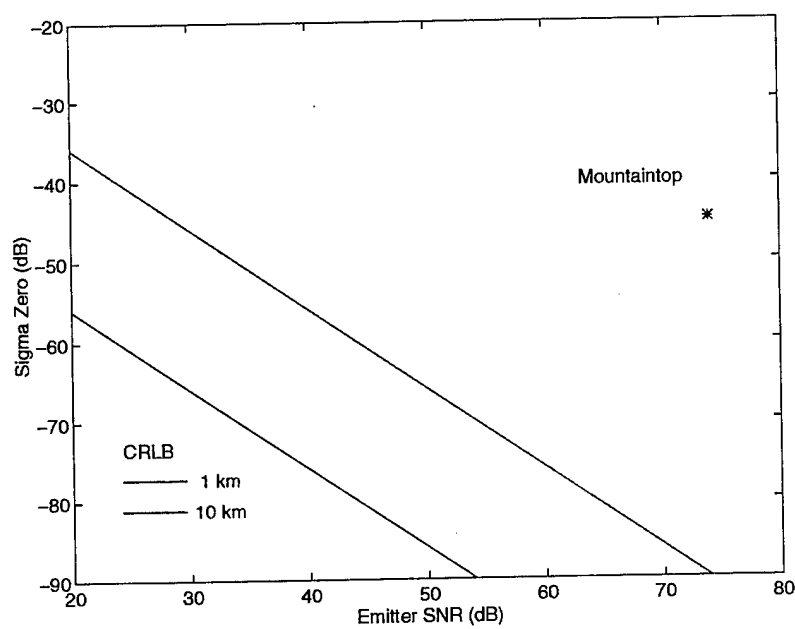


Figure 6.20. Loci of constant performance versus emitter SNR and average bistatic clutter strength.

We can investigate localization performance versus SNR with Mountaintop data by artificially increasing the noise floor of the receiver. This is accomplished by the addition of independent noise sources at the terminals of the receiver as shown in Figure 6.21. This is equivalent to reducing either the power of the emitter or the reflectivity of the terrain. Lowpass filters have also been added to investigate localization performance as a function of emitter bandwidth.

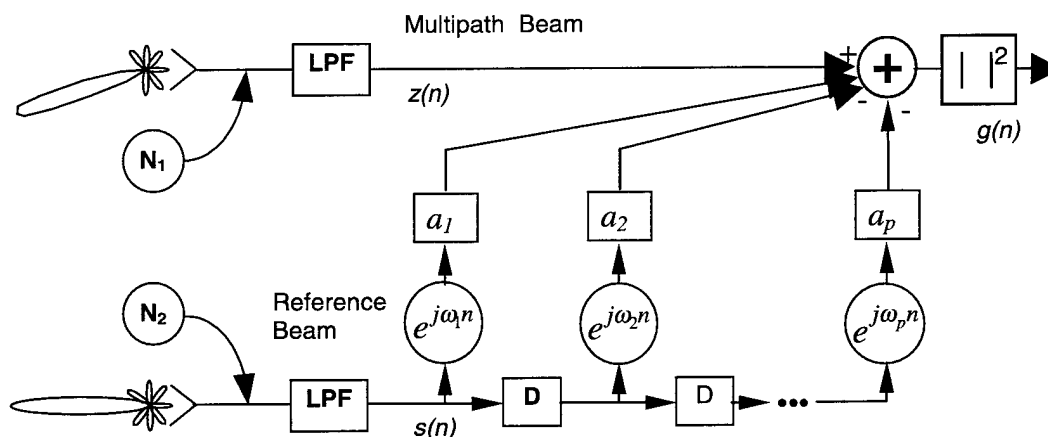


Figure 6.21. Emitter localization filter for showing injected noise and lowpass filtering operations.

Emitter localization was performed for HOT-6067 with noise added in 10 dB increments from 0 to 50 dB. This corresponds to emitter signal-to-noise ratios of 60-10 dB per antenna element or 71.5-21.5 dB in the main beam. The range cuts that result are shown in Figure 6.22. The ordinate axis has been changed from log-likelihood to cancellation ratio ( $|z|/|g|$ ) to facilitate an estimation of the model noise which is discussed below. In the figure we see peaks near the correct range for emitter SNR extending all the way down to 20 dB per element. The full range-heading slice is shown in Figure 6.23 for both the full-power case and the 30-dB SNR case. The 30-dB SNR case corresponds to an emitter power of only 0.350 Watts.

We can infer the level of model noise for this scenario by considering the TSI cancellation properties of the localization filter and the results shown in Figure 6.22. We see in the figure that the 10-dB increase in receiver noise that reduced the SNR from 60 to 50 dB produced a negligible change in cancellation ratio. This is a clear indication that the cancellation performance of this filter is not limited by receiver noise but by model noise. The second 10-dB increase in noise dropped the cancellation performance by about 3 dB from the starting point. The 3-dB drop in cancellation indicates that this is the point where the model noise and the receiver noise are equal in power. Hence the model noise for this scenario is about 20 dB above the receiver noise. This suggests that the theoretical Mountaintop point on Figure 6.20 should be moved to the left by 20 dB for the terrain at WSMR.



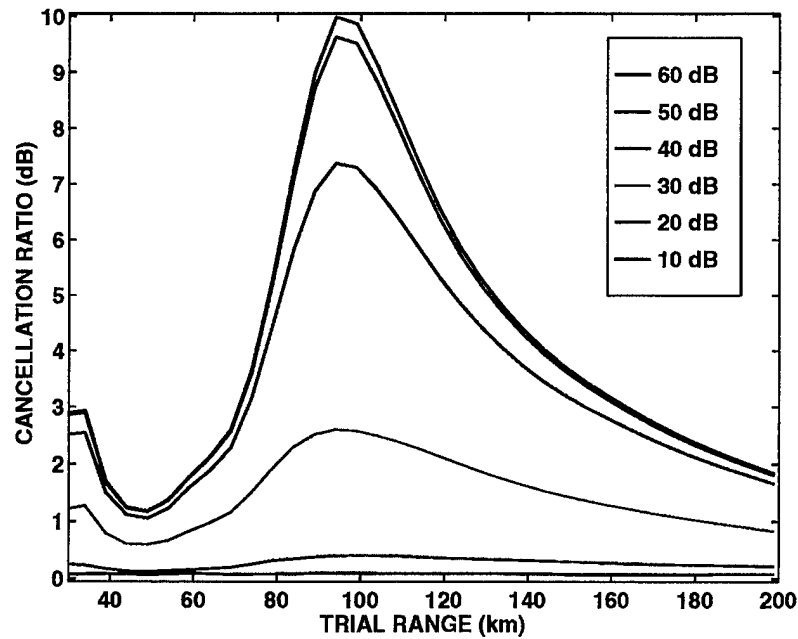


Figure 6.22. Cancellation ratio of localization filter versus range cut for emitter SNR ranging from 60 down to 10 dB.

The effect of reducing the emitter bandwidth *and* power is shown in Figure 6.23. Part (a) shows the full-power, full-bandwidth case, and part (b) shows the 30 dB per element SNR case filtered to 10-kHz bandwidth. The 10-kHz bandwidth was chosen because it is commensurate with the bandwidth of a voice communications channel. The peak of the likelihood function is spread somewhat but it clearly identifies the emitter very near the true range and heading. The number and spacing of the localization filter coefficients was not changed for the reduced bandwidth case.

The performance of the estimator for inhomogeneous clutter was also studied as a function of emitter power and bandwidth. The results are listed in Table 6.7. The first column shows the results presented above for the full power and full bandwidth case. The middle column shows the results for a reduction in power of 43 dB. The number of scatterers available has dropped from 67 to 36 but the localization results are still reasonable. For the final column, the emitter power was dropped by 33 dB and the bandwidth reduced to 20 kHz. A three-dimensional estimate was made that may still be useful. For this final case, the number of scatterers available was reduced to six. Further reductions in SNR or bandwidth caused this estimator to fail completely. Thus it appears that the estimator for homogenous clutter may be better for lower bandwidth signals than the estimator for inhomogeneous clutter for this data set.

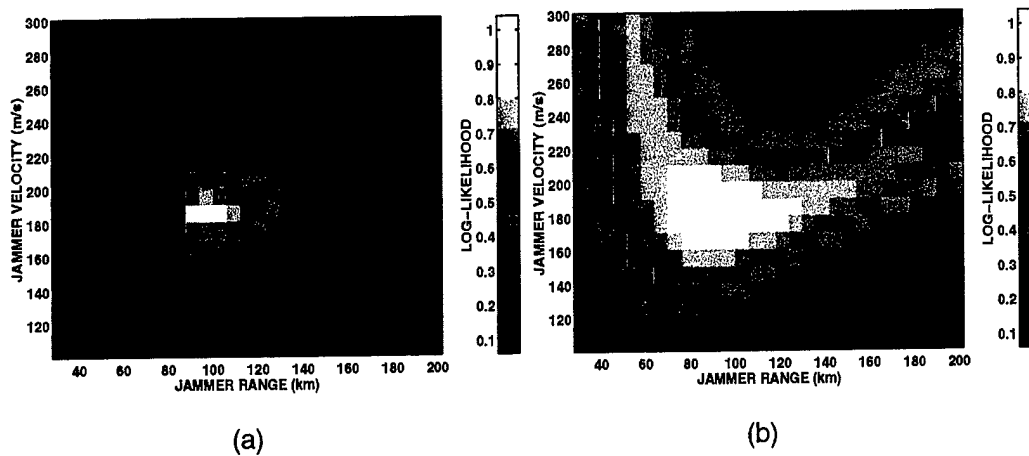


Figure 6.23. Range-velocity slices of the log-likelihood function for (a) 700W/200 kHz and (b) 0.35W/10 kHz cases.

TABLE 6.7

Results for Reduced Emitter Power and Bandwidth Using the Estimator for Inhomogeneous Clutter

Emitter Parameter	True Value	700 W Power 200 kHz BW		0.035 W Power 200 kHz BW		0.35 W Power 20 kHz BW	
		Est.	CRLB $\sigma$	Est.	CRLB $\sigma$	Est.	CRLB $\sigma$
Range (km)	101.7	101.0	0.31	94.0	2.1	78.8	14
Heading (deg)	-147.2	-147.0	0.05	-146	0.46	-141	4.3
Velocity (m/s)	184.5	179.3	0.47	175	3.4	130	26.8
Altitude (km)	8	9.4	0.31	10.9	0.35	—	—
# Scatterers		67		36		6	

## 6.5 CHAPTER SUMMARY

This chapter contains a demonstration of the localization techniques designed in this report using Mountaintop field data. The localization estimators were found to perform very well with performance

reasonably close to the theoretical performance predicted in Chapter 5. Localization performance for lower power and bandwidth emitters was also considered by artificially reducing the emitter power and bandwidth. We are very pleased with these results and feel that we have fully validated the estimators designed in Chapters 3 and 4. We consider some basic extensions to these results in the next chapter.

## 7. EXTENSIONS TO THE BASIC RESULTS

### 7.1 INTRODUCTION

In this chapter we indicate how the basic results of Chapters 3-6 may be extended to include a broader range of localization scenarios and class of emitter signals. Examples and demonstrations are provided using Mountaintop data where appropriate. We discuss how to incorporate Doppler modulation generated by a moving receiver as well as that generated by the moving emitter. We also consider the localization of multiple emitters. In addition, various emitter waveforms are examined including pulsed, periodic, and self-correlated waveforms. These waveforms often cause problems for localization schemes because multiple peaks arise in auto- and cross-correlation functions. The multiple peaks may generate false emitter locations or ghosts. However, we shall see that our out-of-plane multipath technique offers some immunity to these problems because it uses FDOA (frequency difference of arrival) as well as TDOA information in the multipath signals.

### 7.2 MOVING RECEIVER AND EMITTER

If the receiver is also moving, the Doppler shifts due to receiver motion must be considered when determining the FDOA. The total Doppler shift for a terrain-scattered signal will be the sum of the Doppler shift due to each moving platform. This is illustrated in Figure 7.1 which shows isodoppler contours for the moving receiver, the moving emitter, and the moving receiver and emitter. We will show that the addition of receiver motion to the moving emitter localization problem requires only a simple Doppler correction when the receiver velocity and heading are assumed to be known.

In Appendix C the differential Doppler was shown to be

$$\begin{aligned} f &= f_s - f_{dp} \\ &= \mathbf{V}_t \cdot \hat{\mathbf{R}}_t - \mathbf{V}_t \cdot \hat{\mathbf{R}}_{tr} \end{aligned} \quad (7.1)$$

where  $\hat{\mathbf{R}}_{tr}$  is the unit vector along  $R$ , directed toward the receiver, and  $\hat{\mathbf{R}}_t$  is the unit vector along  $R_t$  directed toward the scatterer. The terms  $f_s$  and  $f_{dp}$  denote the Doppler shifts for the scattered and direct-path signal, respectively. The bistatic triangle is shown in Figure 7.2.

The additional Doppler shift caused by the receiver motion can be included in (7.1) as

$$\begin{aligned} f &= f_s - f_{dp} \\ &= (\mathbf{V}_t \cdot \hat{\mathbf{R}}_t - \mathbf{V}_t \cdot \hat{\mathbf{R}}_{tr}) + \{\mathbf{V}_r \cdot \hat{\mathbf{R}}_r - \mathbf{V}_r \cdot \hat{\mathbf{R}}_{rt}\} \end{aligned} \quad (7.2)$$

where the term in parentheses is the original expression and the term in brackets is the contribution due to receiver motion. The latter term is known completely since the receiver heading and velocity are

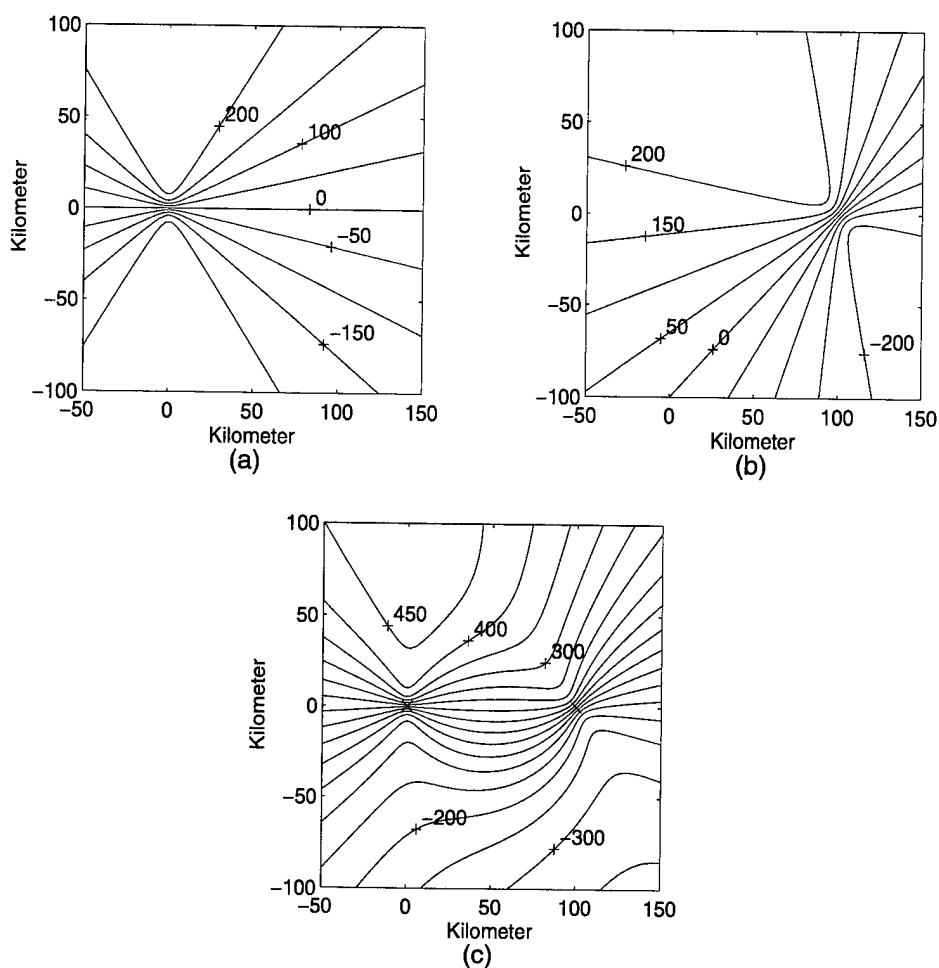


Figure 7.1. Doppler contours for (a) moving receiver, (b) moving emitter, and (c) moving receiver and emitter.

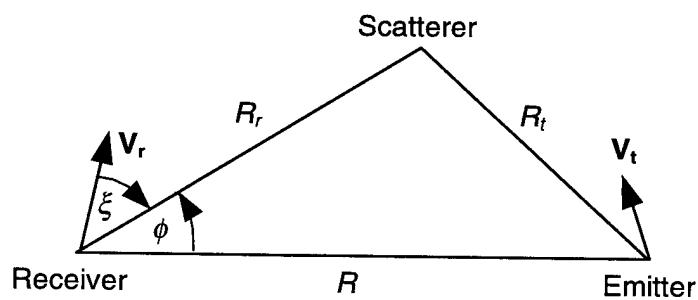


Figure 7.2. Bistatic triangle formed by the receiver, emitter, and scatterer.

assumed to be known, and the scatterer and emitter azimuthal angles are measured. Hence, the results of Chapters 3-5 can be directly extended to the moving emitter case. We note that for a specific receive beam, this term will be constant since the Doppler shift due to the receiver is given by  $V_r/\lambda \cos \xi$ .

### 7.3 PULSED EMITTER WAVEFORM

In this subsection we localize a periodic, pulsed emitter using the estimator designed for inhomogeneous clutter. Up to this point, the emitter waveforms were assumed to be white. The pulsed emitter was an airborne radar transmitter used to collect bistatic clutter data for reflectivity measurements. Thus, localizing this emitter is essentially equivalent to localizing passively an airborne radar system. Data set HOT-6138 will be used, and the location of this emitter was shown in Figure 6.2.

The transmitter waveform is pulsed CW with a pulse width of 13  $\mu$ s, a PRF of 300 Hz, and a peak power of 2 kW. The duty cycle of this waveform is 0.39 percent and the average power is only 7.8 Watts. The signal in the direct-path beam and two multipath receive beams is shown in Figure 7.3. The strongest signal present in the multipath beams is the emitter signal that is present in the sidelobes; however, scattered energy is evident out to about 200  $\mu$ s.

The scatterer parameters of delay, Doppler, azimuth, and SNR were estimated using the same structure that was used for the CW waveforms. That structure was shown in Figure 6.13. The number of scatterers detected was 40, and the location of the scatterers is shown in Figure 7.4. This is one half the number detected for HOT-6132 which has nearly the same geometry. This reduction in the number of scatterers is probably due to the reduction in average power and loss of resolution for the pulsed waveform. The localization results are listed in Table 7.1. The error in the range estimates is 16 percent which is much larger than the examples in Chapter 6. If the true emitter altitude of 8 km is supplied to the estimator so that only range, heading, and velocity are estimated, then the results are 188.6 km, 143.2, and 207.5, respectively. The range error reduces from 16 percent to only 3 percent. It is interesting that such a small change in altitude (from 11.8 to 8 km) produced such a large change in range estimate. Some possible explanations for this behavior were given in Section 6.3.3.

**TABLE 7.1**  
**Results for Data Set HOT-6138**

Emitter Parameter	True Value	Estimated Value	Error Value CRLB		CRLB $\sigma$
Range (km)	183.3	153.2	30.1	23 $\sigma$	1.3
Heading (deg)	143.5	141.9	1.6	1.0 $\sigma$	1.5
Velocity (m/s)	191.5	149.5	42	49 $\sigma$	0.85
Altitude (km)	8	11.8	3.8	2.2 $\sigma$	1.7

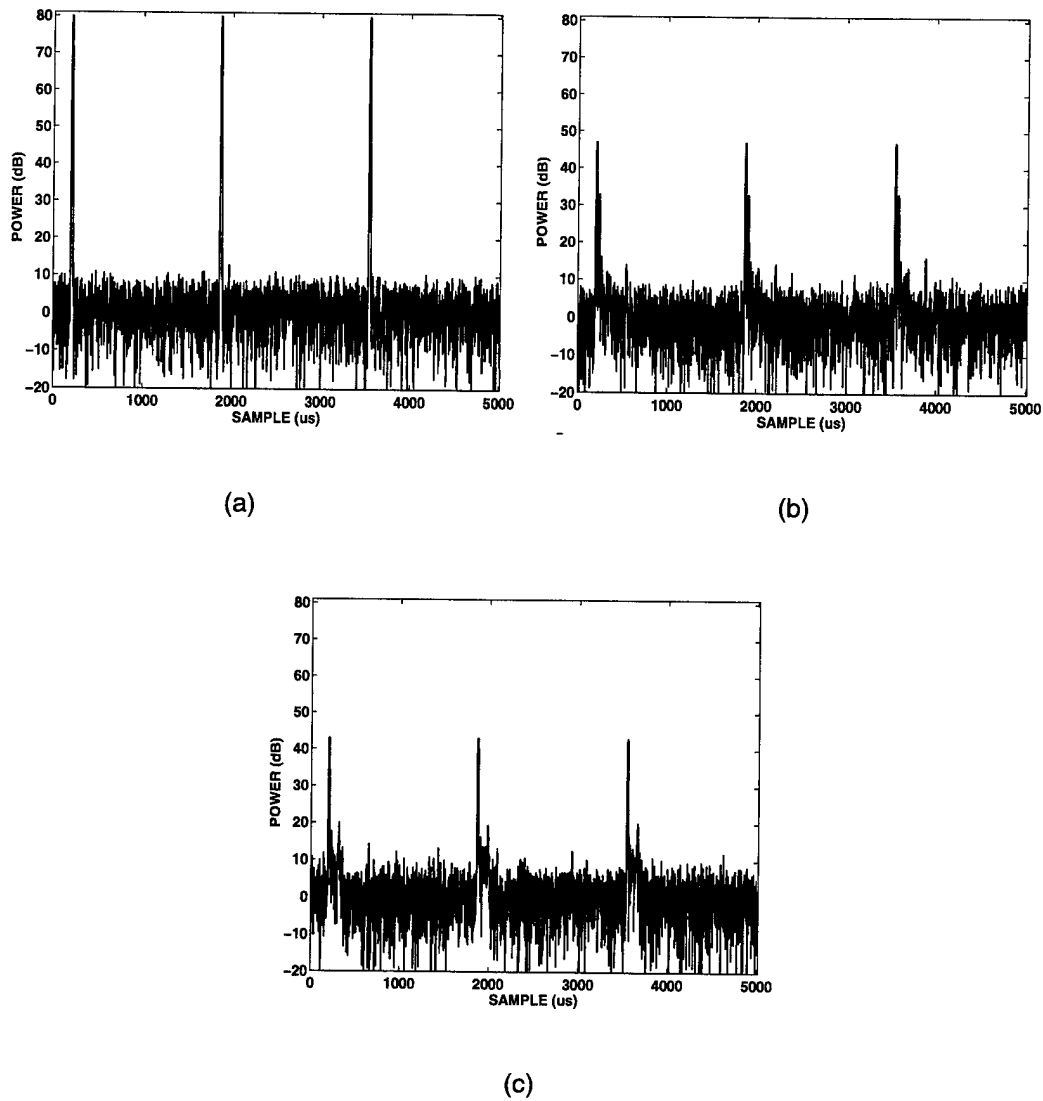


Figure 7.3. Received power versus sample for (a) the direct path beam at 302 degrees (true north), and multipath beams at (b) 228 and (c) 262 degrees.

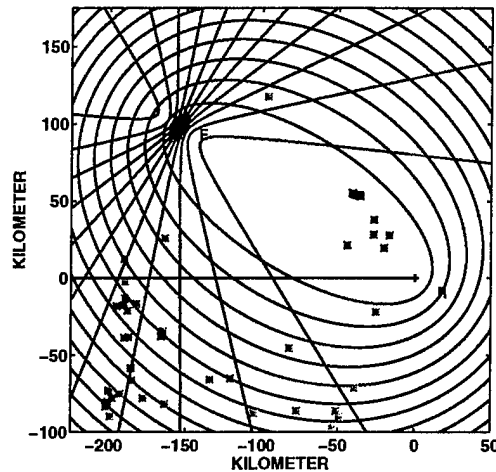


Figure 7.4. Map of scatterers used for the localization of data set HOT-6138.

#### 7.4 SELF-CORRELATED EMITTER WAVEFORM

We now consider correlation in the emitter waveform. An emitter waveform that is correlated with itself can generate multiple TDOA peaks during cross-correlation operations. The multiple TDOA estimates can produce false targets or ghosts. This is illustrated graphically in Figure 7.5 where three hyperbolas are seen to intersect at nine points.

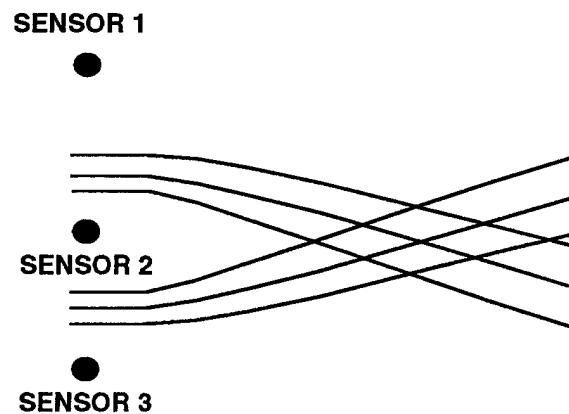


Figure 7.5. Correlation in the emitter waveform can produce multiple TDOA estimates which can generate false emitter positions when using multisensor localization TDOA techniques.



To investigate the effect of self-correlation for the techniques described in this report, we introduce self-correlation to data set HOT-6067 as shown in Figure 7.6. The autocorrelation function for the correlated data set is shown in Figure 7.7. The peaks are close enough to generate ghosts at realistic ranges.

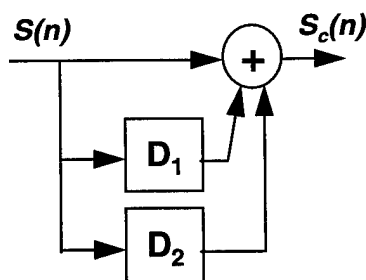


Figure 7.6. Schematic for introducing self correlation.

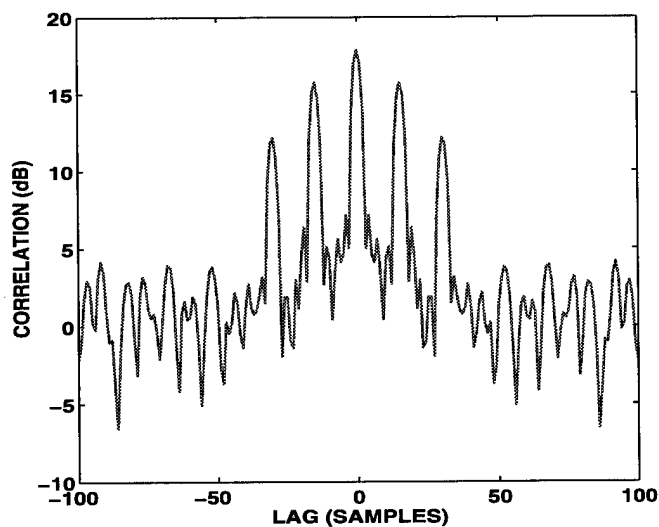


Figure 7.7. Autocorrelation function of self-correlated emitter waveform.

The estimator designed for homogeneous clutter was used for this data set and the results are shown in Figure 7.8. Part (a) shows the log-likelihood function for the original data set and part (b) shows the log-likelihood function for the correlated data set. There is some spreading of the peak but no false localizations occur. Ghosts are not generated because the Doppler present in the multipath signal corresponds only to the true emitter since it is due to the emitter's motion. The correlation manifests itself as increased noise which blurs the peak of the likelihood function.

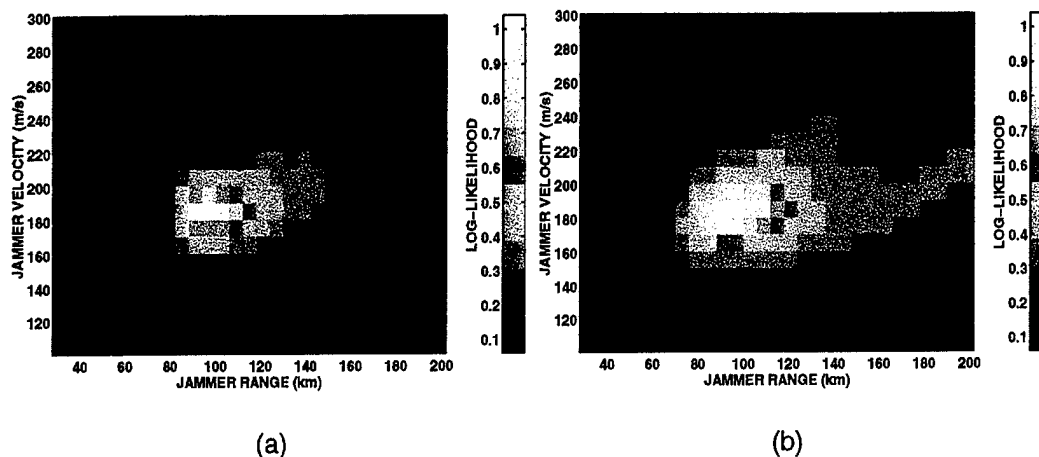


Figure 7.8. Log-likelihood function (a) without and (b) with self-correlation. No false targets are generated.

## 7.5 MULTIPLE EMITTERS

The localization techniques described in this report are readily extended to the case of multiple emitters. In this section we consider three possible approaches for use with the estimator for homogeneous clutter. The basic scenario is shown in Figure 7.9. This figure shows a single multipath beam and two reference beams, one for each emitter. The two emitter waveforms are assumed to be uncorrelated.

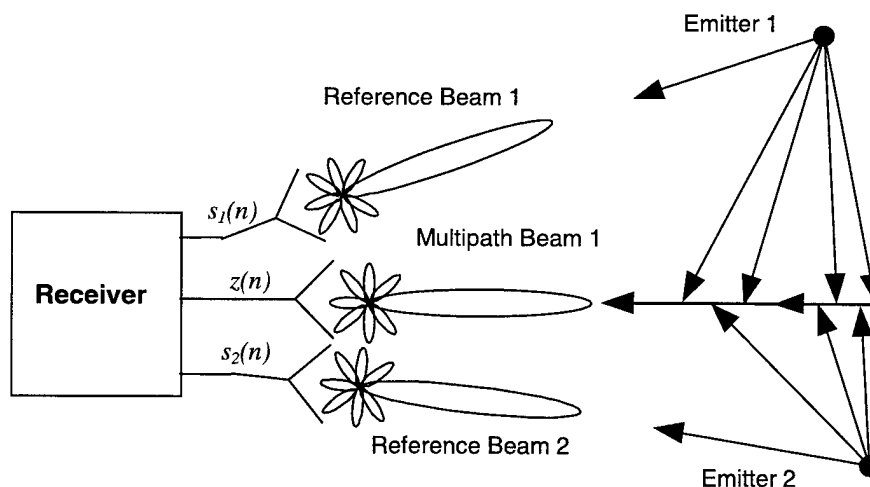


Figure 7.9 Localization of two emitters. The multipath beam contains energy from both emitters. Separate reference beams collect the two emitter waveforms.

### 7.5.1 Sub-optimum Technique

The simplest approach is to localize the emitters one at a time while essentially ignoring the presence of the other emitters. This is not optimum because the other emitters will produce TSI in the receive beam which effectively raises the noise level of the receiver. The situation can be improved somewhat by assuring that the receive and reference beams are orthogonal. This assures that unwanted emitter energy does not enter through the sidelobes. An example using this sub-optimum technique with Mountaintop data will be given in Section 7.5.4.

### 7.5.2 Full Maximum Likelihood Approach

The maximum likelihood solution described in Chapter 4 can be extended to multiple emitters. The cost is fairly high, however. For example, to localize two emitters, the dimensions of the parameter search doubles, as does the size of the covariance matrix that is inverted at each step of the search.

To extend the ML solution to two emitters,  $s_1$  and  $s_2$ , we rewrite (3.21) as

$$\mathbf{S} = \begin{bmatrix} s_1(P) & s_1(P-1) & \cdots & s_1(2) & s_1(1) & s_2(P) & s_2(P-1) & \cdots & s_2(2) & s_2(1) \\ & s_1(P) & \cdots & \cdots & s_1(2) & & s_2(P) & \cdots & \cdots & s_1(2) \\ \vdots & \vdots & \vdots & \vdots & \vdots & \vdots & \vdots & \vdots & \vdots & \vdots \\ s_1(N-1) & s_1(N-2) & \cdots & & \vdots & s_2(N-1) & s_2(N-2) & \cdots & & \vdots \\ s_1(N) & s_1(N-1) & \cdots & \cdots & s_1(N-P+1) & s_2(N) & s_2(N-1) & \cdots & \cdots & s_2(N-P+1) \end{bmatrix} \quad (7.3)$$

and solve  $\mathbf{a} = (\mathbf{S}^H \mathbf{S})^{-1} \mathbf{S}^H \mathbf{z}$  for the filter coefficients. The length of the coefficient vector  $\mathbf{a}$  will be  $2P$ , where  $P$  is the length of the original filter. The parameter vector is written as

$$\boldsymbol{\theta} = \{R_1, H_1, V_1, A_1, R_2, H_2, V_2, A_2\}. \quad (7.4)$$

To maximize the likelihood function it is necessary to search over the entire parameter vector for the minimum output of the localization filter.

### 7.5.3 Maximum Likelihood EM Approach

The expectation-maximization (EM) algorithm [74] can be used to simplify the full ML approach described above. We write the received signal for two emitters with parameter vectors  $\boldsymbol{\theta}_1$  and  $\boldsymbol{\theta}_2$  as

$$z(n) = m_{\boldsymbol{\theta}_1}(n) + m_{\boldsymbol{\theta}_2}(n) + g(n), \quad (7.5)$$

where  $g(n)$  is additive Gaussian noise. Using the current estimate for one of the emitters,  $\boldsymbol{\theta}_1$  say, we obtain

$$\hat{z}_2(n) = z(n) - m_{\hat{\boldsymbol{\theta}_1}}(n). \quad (7.6)$$

This is an estimate of the signal due to emitter 2 alone given that  $m_{\hat{\boldsymbol{\theta}_1}}(n)$  is the signal due to emitter 1.

We then use the estimated signal  $\hat{z}_2(n)$  to estimate  $\boldsymbol{\theta}_2$  as we did in Chapter 3 when only one emitter was present. Then the estimate of the signal due to emitter 1 is modified to be

$$\hat{z}_1(n) = z(n) - m_{\hat{\boldsymbol{\theta}_2}}(n) \quad (7.7)$$

and proceed to refine our estimate of  $\boldsymbol{\theta}_1$ . We continue this iterative procedure until the parameter sets converge. Initial guesses at the parameter sets can be obtained using the sub-optimal method described above.

#### 7.5.4 Two Emitter Example Using the Sub-optimum Technique

In this section we will localize two emitters in Mountaintop data using the sub-optimum approach described in Section 7.5.1. The two-emitter data set will be generated by combining two separate data sets, each of which contains a single emitter. This approach is necessary because the Mountaintop experiments did not use more than one airborne emitter. The Milligan Gulch data sets HOT-6161 and HOT-6165 were used. HOT-6161 was localized in Chapter 6 and the geometry was shown in Figure 6.2. The data for HOT-6165 was collected a few minutes after HOT-6161 while the emitter was traveling along approximately the same track.

An advantage of studying multiple emitters with a data set constructed in this manner is that one can first investigate the localization of the emitters separately, and then investigate the performance for the combined data set. The conventional and MVDR spatial power spectra are shown in Figure 7.10 (a) and (b) for the individual data sets HOT-6161 and HOT-6165, respectively. The spatial spectra for the combined data set are shown in (c). The conventional spatial power spectral estimate does not resolve the two emitters but the MVDR spectrum does due to its high resolution properties. The eigenvalues of the spatial covariance matrix are shown in part (d). The two strong eigenvalues correspond to the strong direct paths and the weaker eigenvalues correspond to the emitter multipath. Note that even the weakest eigenvalue is a full 10 dB above receiver noise.

The sub-optimum approach localizes an emitter in the presence of TSI from other emitters. The TSI from other emitters acts to increase the noise level and will reduce localization performance. Some attempts can be made to minimize the effect of the other emitters, however. For example, spatially adaptive antenna beams can be used for the reference beams. This assures that emitter reference signal for one emitter does not contain any energy from the other emitter. The adapted antenna patterns for the two emitters are shown in Figure 7.11. Sidelobe cancellers are used to remove from the multipath beam the direct-path and short-time-delay signals from each of the two emitters.

The emitters were localized and the results are shown in Figure 7.12. Parts (a) and (b) are the results of the single emitter localization, and parts (c) and (d) are for the two-emitter data set. Both emitters have been localized, but the dynamic range of the log-likelihood function has been reduced significantly as the result of the apparent noise increase due to the presence of the second emitter. Nevertheless, the localization is successful and could be used to initiate an iterative procedure such as the EM algorithm.

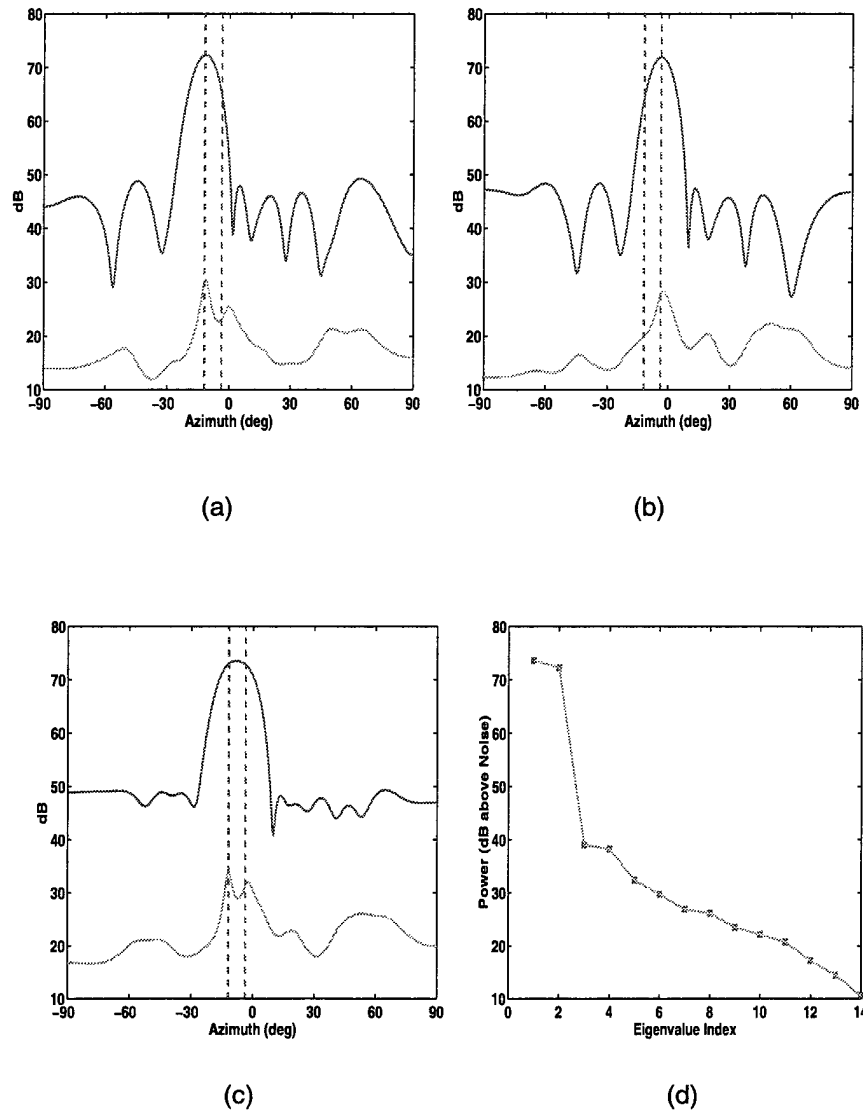


Figure 7.10. Conventional and MVDR spatial power spectra in dB above thermal noise for single-emitter data sets (a) HOT-6161, (b) HOT-6165, and (c) the two-emitter combination of the data sets. The dashed lines represent the true emitter angles. Part (d) shows the eigenvalues for the combined data set.

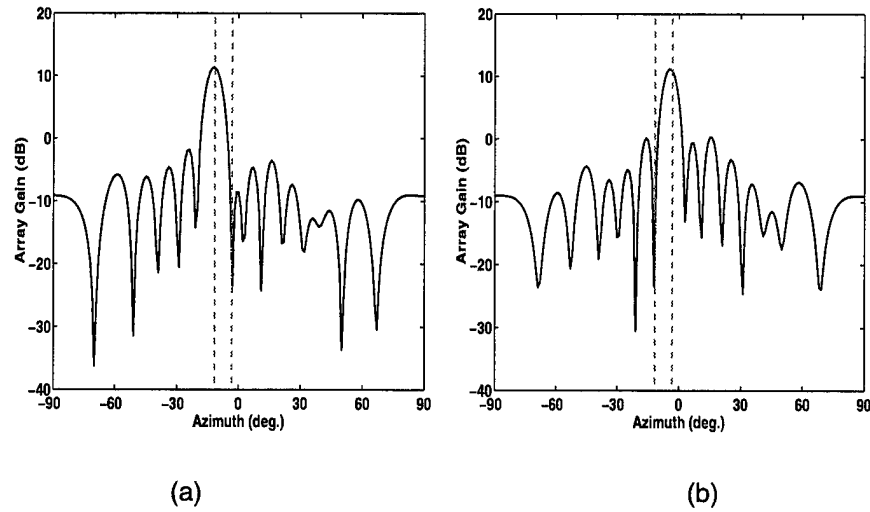


Figure 7.11. Adapted beam patterns for the two reference beams. Spatial nulls are placed at the location of the other emitter.

## 7.6 CHAPTER SUMMARY

In this chapter we have outlined methods by which the basic results of Chapters 3–6 can be extended to include a broader range of scenarios and class of emitter signals. We showed that receiver motion could be handled by a simple adjustment to the Doppler terms for the moving emitter. We also considered the pulsed and self-correlated waveforms, as well as multiple emitters, and demonstrated good performance using Mountaintop data for each case. In the next chapter we present conclusions as well as some additional topics for further research.

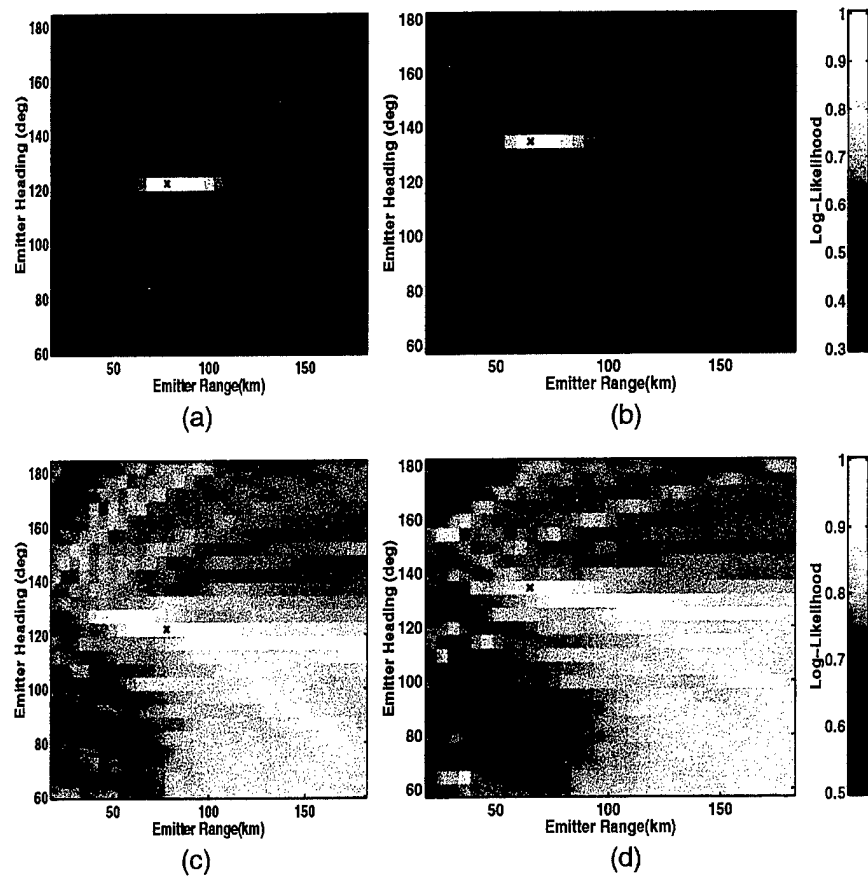


Figure 7.12. Single and multiple emitter localization results for data set HOT-6161 and HOT-6165. Parts (a) and (b) show the single emitter results, and (c) and (d) show the multiple emitter results for HOT-6161 and HOT-6165, respectively.



## 8. SUMMARY AND CONCLUSIONS

### 8.1 SUMMARY

The work described in this report established how to localize passively a moving emitter using out-of-plane multipath signals reflected by the terrain. This is a novel localization technique that assumes no *a priori* knowledge on the location of the multipath sources. The emitter parameters of range, heading, velocity, and altitude are estimated by exploiting the correlation between the direct-path signal and the delayed and Doppler modulated multipath signals. In this section we summarize the results and suggest areas for future research.

Two basic assumptions about the scattering properties of the terrain lead to two different maximum likelihood (ML) estimators of emitter parameters. The first assumption is that the terrain scattering is fundamentally homogeneous; in this case the ML estimator is found to have the structure of a time-varying FIR filter. The time-varying nature of the filter is due to the Doppler modulators that are computed deterministically for each trial parameter set. The trial parameters are selected from a dense multidimensional parameter grid over which we search for the true emitter parameters. The filter coefficients (which are nuisance parameters) are computed using the method of least squares at each point in the search. The trial parameter set that minimizes the filter output is the ML estimate.

The second assumption is that the terrain scattering is fundamentally inhomogeneous and dominated by a number of discrete scatterers. This assumption leads to a two-part estimator which first estimates the scattering parameters of azimuth, differential delay, and Doppler, and then estimates the emitter parameters of range, heading, velocity, and altitude. The nonlinear localization equations are linearized by using a truncated Taylor series expansion and the emitter parameters are estimated by performing a coarse least-squares search followed by an iterate minimization technique.

The Cramer-Rao lower bounds for each estimator are derived and used to study estimator performance for a number of scenarios. The effect of varying the emitter and several receiver parameters was considered. We saw that estimator performance was related to emitter velocity, as well as other factors such as emitter power, heading, altitude, etc. Monte-Carlo simulations are performed to validate the bounds calculations and overall implementation of the estimators prior to their use with field data. We also discussed potential limitations that could arise when applying these bounds to real data. These limitations resulted from simplifications in the models that could be accounted for by the introduction of model noise above the thermal noise level. The model noise was found to be 20 dB for data set HOT-6067.

In Chapter 6 we demonstrated the estimators using field data collected at White Sands Missile Range during the DARPA/Navy Mountaintop program. Several emitters were localized using both estimators. In general, the estimator designed for inhomogeneous clutter performed better than the estimator for homogeneous clutter. This difference in performance can probably be attributed to the inhomogeneous nature of the bistatic clutter at WSMR. However, the estimator for homogeneous clutter

performed better than the estimator for inhomogeneous clutter when the bandwidth of the receiver was reduced to 20 kHz or less. For such low bandwidths, the discrete scattering model breaks down due to the loss of range resolution.

In Chapter 7 we showed how the basic results could be extended to include a broader range of scenarios and class of emitter signals. We discussed the incorporation of Doppler modulation generated by a moving receiver as well as the moving emitter. This was found to require only a minor change in the way relative Doppler shift is computed. We also considered the localization of multiple emitters and used a sub-optimum technique to localize two emitters simultaneously. In addition, we considered various emitter waveforms including pulsed and self-correlated waveforms and provided an example for each using Mountaintop data. In both cases the emitters were localized without any additional false targets (or ghosts).

## 8.2 FUTURE RESEARCH

There are several potential areas for further research related to the topics in this report. They can be roughly divided into two areas: further investigations into the bistatic scattering properties of the terrain and further work on the estimation techniques. We discuss a few examples in this section.

A very important question is whether or not this localization technique can be used over the ocean. Sea clutter presents two potential problems. The first is that sea clutter exhibits intrinsic motion that will generate additional Doppler shifts. This may reduce localization performance or bias estimates if not accounted for. The second problem is that sea clutter may be too homogeneous to use the estimator designed for inhomogeneous clutter unless sea spikes are prevalent. In addition, the general bistatic scattering levels for sea clutter may be much lower than for land clutter; however, we saw in Section 6.4 that there is considerable excess signal-to-noise ratio available for the Mountaintop parameters and, based on that observation, we believe the estimator designed for homogeneous clutter will work over the ocean. This assertion should be validated with field data, however.

There are several issues related to the estimator for the inhomogeneous scattering model that should be investigated further. The work here assumed that all the scatterers that were detected had variances inversely proportional to their SNR. However, we saw in Section 6.3.3 that by excluding one of eighty scatterers, the localization estimates improved significantly. We believe the parameters for this scatterer have been corrupted by coherent interference. Future work could investigate effective ways of selecting a minimum subset of scatterers that will produce good localization estimates. An alternative to excluding particular scatterers could be to treat them as nuisance parameters to be estimated along with the emitter parameters. A related issue is the effect of "false scatterers" on the localization estimator. For example, a noise spike or bistatic scattering from a target such as a moving aircraft will have erroneous scattering parameters when viewed as bistatic clutter, and these false scatterers could degrade localization estimates. Future work should include a study of the behavior of this estimator in the presence of erroneous scattering parameters. The Hough transform described in Chapter 2 may be a useful tool for evaluating graphically the contributions of individual scatterers.

The Doppler terms computed in this report were based on a flat-earth approximation. Future work could include a reformulation of the geometry using site-specific digital elevation data. This improved geometric model may reduce localization errors or biases, especially for mountainous terrain such as that found at WSMR.

The use of *a priori* scattering information was not considered in this report; however, if *a priori* knowledge of the location of strong scatterers was available, it could be used to localize emitters. This may permit the localization of stationary emitters that would otherwise not be possible using the techniques described in Chapters 3 and 4. Sources of *a priori* knowledge on bistatic scattering could include site-specific bistatic clutter models that use digital elevation data. Another source of terrain knowledge could be extracted from the monostatic clutter data collected in an active mode. The idea would be to compare azimuth-delay maps measured using cross-correlation of the emitter waveform to maps generated based on trial emitter locations and the *a priori* clutter information.

We close this section by noting that in this report we have demonstrated the ability to localize moving emitters, using out-of-plane multipath, for one system operating at one site. The Mountaintop radar has a UHF phased-array receiver and was operating over desert and mountainous terrain at WSMR. To fully explore the usefulness of these localization techniques for other applications, modeling and measurement programs should be carried out for additional systems and over additional terrain types.

## **APPENDICES**

Appendices A–D contain the geometrical relations and derivations necessary to support the work contained in this report. Included is the determination of the Doppler shift terms for two- and three-dimensional approximations as well as the general three-dimensional solution. Also included are the differential terms necessary to form the Fisher information matrix.

## APPENDIX A

### DOPPLER TERMS FOR TWO-DIMENSIONAL APPROXIMATION

The two-dimensional approximation to the bistatic geometry of concern here makes use of the fact that the platform ranges are generally much greater than the platform altitudes. For example, the height of the Mountaintop receiver above the ground is approximately 1.2 km and the emitter altitude is 7-8 km while the range to the emitter is typically 100-200 km. Therefore, we shall assume for this section that the receiver, emitter, and scatterer are all located in the same horizontal plane. The top-down view of the bistatic triangle is shown in Figure A.1. We have also assumed that the earth is flat and defined the azimuthal angle of the emitter relative to the receiver to be zero.

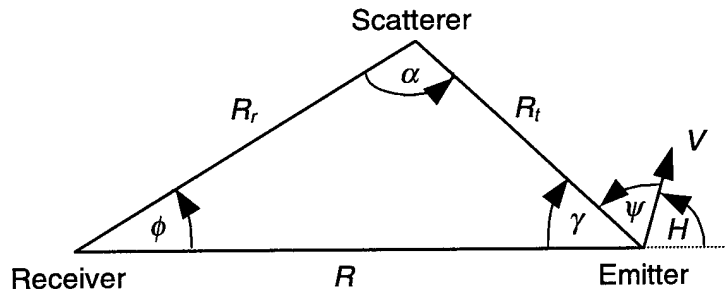


Figure A.1. Bistatic triangle formed by the receiver, emitter, and scatterer.

The goal is to obtain an expression for Doppler shift  $f$  as a function of the emitter parameters ( $R$ ,  $H$ ,  $V$ ), and the measurable quantities of bistatic delay  $D$  and scatterer azimuth  $\phi$ . The bistatic delay  $D$  is related to the range to the emitter  $R$ , the range to the scatterer  $R_r$ , and the range from the emitter to the scatterer  $R_t$  as

$$D = R_r + R_t - R . \quad (\text{A.1})$$

Using the law of cosines we can solve for the range to the scatterer  $R_r$  in terms of the emitter range  $R$ , bistatic delay  $D$ , and angle  $\phi$

$$R_r = \frac{RD + D^2/2}{D + R - R \cos \phi} . \quad (\text{A.2})$$

The range from the emitter to the scatterer  $R_t$  is obtained by rewriting (A.1) as

$$R_t = R + D - R_r . \quad (\text{A.3})$$

The angle  $\gamma$  can be obtained using the law of sines,

$$\gamma = \sin^{-1} \left( \frac{R_r \sin \phi}{R_t} \right) , \quad (\text{A.4})$$

and the angle  $\psi$  can be written in terms of  $H$  and  $\gamma$ ,

$$\psi = 180 - H - \gamma . \quad (\text{A.5})$$

The Doppler shift observed at the location of the scatterer due to the emitter motion is

$$f_s = \frac{V}{\lambda} \cos \psi , \quad (\text{A.6})$$

which can also be written as

$$f_s = -\frac{V}{\lambda} \cos(H + \gamma) , \quad (\text{A.7})$$

where we have made use of (A.5). The Doppler shift for the direct-path signal is

$$\begin{aligned} f_{dp} &= \frac{V}{\lambda} \cos(180 - H) \\ &= -\frac{V}{\lambda} \cos(H) . \end{aligned} \quad (\text{A.8})$$

The stationary receiver measures the relative Doppler shift between the direct and scattered paths,

$$\begin{aligned} f &= f_s - f_{dp} \\ &= \frac{V}{\lambda} (-\cos(H + \gamma) + \cos(H)) . \end{aligned} \quad (\text{A.9})$$

The angle  $\gamma$  can be expressed in terms of the desired quantities by using (A.2) and (A.3) in (A.4) as

$$\begin{aligned}
\gamma &= \sin^{-1} \left( \frac{R_r \sin \phi}{R_t} \right) \\
&= \sin^{-1} \left( \frac{\left( \frac{RD + D^2/2}{D + R - R \cos \phi} \right) \sin \phi}{R + D - \left( \frac{RD + D^2/2}{D + R - R \cos \phi} \right)} \right) \\
&= \sin^{-1} \left( \frac{(D^2 + 2RD) \sin \phi}{D^2 + 2R^2 + 2RD - 2(R^2 + DR) \cos \phi} \right)
\end{aligned} \tag{A.10}$$

and finally,

$$f = \frac{V}{\lambda} \left( \cos(H) - \cos \left( H + \sin^{-1} \left( \frac{(D^2 + 2RD) \sin \phi}{D_p^2 + 2(R^2 + RD_p)(1 - \cos \phi)} \right) \right) \right), \tag{A.11}$$

which is the final result.

To summarize this appendix, we have derived an expression for the differential Doppler shift, between the scattered and direct path, in terms of the emitter parameters ( $R$ ,  $H$ ,  $V$ ) and the measured parameters ( $D$ ,  $\phi$ ). This equation was derived based on the assumption that the receiver, scatterer, emitter, and emitter velocity are contained in the same plane. Appendix B provides an approximation for the case when the emitter altitude is nonzero and Appendix C treats the general case.

## APPENDIX B

### DOPPLER TERMS FOR THREE-DIMENSIONAL APPROXIMATION

The development in Appendix A contains no provision for emitter altitude estimation because it assumes that both platforms are at zero altitude. In this appendix, we relax this restriction slightly to allow the emitter to have a nonzero altitude that is small compared to the range terms. The Doppler shift at the scatterer for the two-dimensional case was

$$f_s = \frac{V}{\lambda} \cos \psi, \quad (\text{B.1})$$

where  $\psi$  was the azimuth angle measured from the emitter velocity vector to the scatterer. If the emitter is elevated, then  $\psi$  will be a conical angle measured relative to the emitter velocity vector to the scatterer. Using direction cosines, we can write

$$\cos \psi = \cos A_{ts} \cos E_{ts}, \quad (\text{B.2})$$

where  $A_{ts}$  and  $E_{ts}$  are, respectively, the azimuth and elevation angles to the scatterer. We can write the cosine of the elevation angle in terms of the scatterer range  $R_t$  and emitter height  $h_t$  as

$$\cos E_t = \sqrt{1 - \frac{h_t^2}{R_t^2}}, \quad (\text{B.3})$$

and rewrite (A.9) as

$$f = \frac{V}{\lambda} \left( - \left( \sqrt{1 - \frac{h_t^2}{R_t^2}} \right) \cos(H + \gamma) + \cos(H) \right), \quad (\text{B.4})$$

and repeat the algebra in (A.10) and (A.11). The final equation is

$$f = \frac{V}{\lambda} \left( \cos(H) - \left( \sqrt{1 - \frac{h_t^2}{R_t^2}} \right) \cos \left( H + \sin^{-1} \left( \frac{(D^2 + 2RD) \sin \phi}{D_p^2 + 2(R^2 + RD_p)(1 - \cos \phi)} \right) \right) \right), \quad (\text{B.5})$$

with  $R_t$  given by

$$R_t = \frac{R^2 + 3D^2/2 + DR - (R^2 + DR) \cos \phi}{D + R - R \cos \phi}. \quad (\text{B.6})$$

This assumes the height of the emitter is not large enough to change significantly the range terms  $R$  or  $R_p$ . Appendix C treats the general case where no such assumptions or restrictions are necessary.



## APPENDIX C

### DOPPLER TERMS FOR COMPLETE THREE-DIMENSIONAL SOLUTION

In this appendix we consider the general three-dimensional case shown in Figure C-1. The receiver is located at the origin of the rectangular coordinate system, and the conical angles to the scatterer  $C_{rs}$  and emitter  $C_{rt}$  are measured relative to the  $x$ -axis. We desire to obtain an expression relating the Doppler shift  $f$  to the emitter parameters ( $R, H, V, h_t$ ), and the measurable quantities of bistatic delay  $D$ , scatterer cone angle  $C_{rs}$ , and emitter cone angle  $C_{rt}$ .

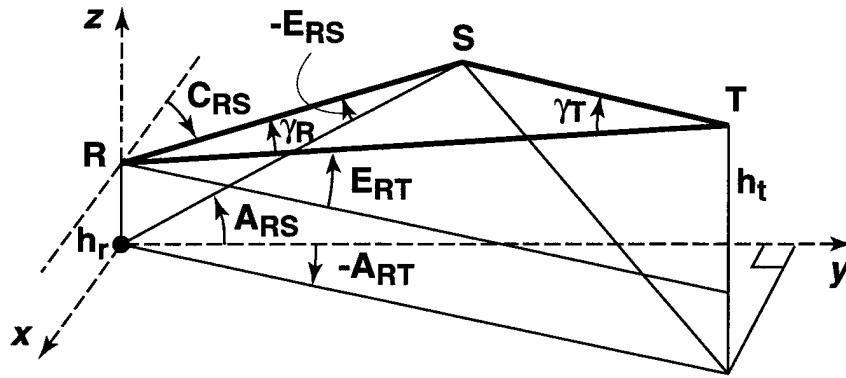


Figure C.1. General three-dimensional bistatic geometry.

An expression for  $\gamma_r$ , the receiver angle between the emitter and the scatterer, can be obtained using direction cosines [47]

$$\cos \gamma_r = \cos E_{rs} \cos E_{rt} \cos(A_{rs} - A_{rt}) + \sin E_{rs} \sin E_{rt} \quad , \quad (C.1)$$

where the angles are as shown in the figure. If  $\gamma_r$  were known, we could proceed as we did above in (A.2)–(A.11); however, this is not the case so we shall proceed as follows. We first write the measured conical angles in terms of azimuth and elevation angles,

$$\cos \gamma_{rt} = \cos A_{rt} \cos E_{rt} \quad (C.2)$$

and

$$\cos \gamma_{rs} = \cos A_{rs} \cos E_{rs} \quad . \quad (C.3)$$

The receiver azimuth and elevation angles to the emitter can be written as

$$A_{rt} = \sin^{-1} \left( \frac{\cos C_{rt}}{\cos E_{rt}} \right) \quad (C.4)$$

$$E_{rt} = \sin^{-1} \left( \frac{h_t - h_r}{R} \right) . \quad (C.5)$$

Similarly, the receiver azimuth and elevation angles to the scatterer can be written as

$$A_{rs} = \sin^{-1} \left( \frac{\cos C_{rs}}{\cos E_{rs}} \right) \quad (C.6)$$

$$E_{rs} = \sin^{-1} \left( \frac{\sqrt{(R_r^2 - h_r^2)}}{R_r} \right) . \quad (C.7)$$

We can now insert (C.1) into (A.2) to yield

$$R_r = \frac{RD - D^2/2}{D + R - R(\cos E_{rs} \cos E_{rt} \cos(A_{rs} - A_{rt}) + \sin E_{rs} \sin E_{rt})} \quad (C.8)$$

and solve numerically using Newton's method. The numerical method is required because  $R_r$  appears on both sides of (C.8) because of the elevation angle described by (C.7). For the initial values required to start the iterative technique, we set the two elevation angles to zero, and then (C.8) reduces to the two-dimensional case (A.2) which can be solved directly.

We proceed in a similar manner to obtain the azimuth and elevation angles of the scatterer relative to the emitter. The range from the emitter to the scatterer was given by (A.3) as

$$R_t = R + D - R_r . \quad (A.3)$$

The elevation angle  $E_t$  to the scatterer is

$$E_t = \sin^{-1} \left( \frac{\sqrt{(R_t^2 - h_t^2)}}{R_t} \right) . \quad (C.9)$$

To find the azimuth angle we rewrite (C.1) for the transmitter as

$$\cos \gamma_t = \cos E_t \cos E_{tr} \cos(A_t - A_{tr}) + \sin E_t \sin E_{tr} \quad (C.10)$$

and solve for  $A_t$ . The angle  $\gamma_t$  is determined using the law of cosines

$$\gamma_t = \cos^{-1} \left( \frac{R^2 + R_t^2 - R_r^2}{2RR_t} \right). \quad (\text{C.11})$$

With the bistatic triangle determined, we now proceed to determine relative Doppler shift. For this development it will be convenient to use vectors and dot products. As a final check on our derivations, we shall show that the three-dimensional case will reduce to the two-dimensional case described above when the receiver and emitter altitudes are set to zero.

We now introduce two unit vectors:  $\hat{\mathbf{R}}_{rt}$  is the unit vector along  $R$ , directed toward the transmitter and  $\hat{\mathbf{R}}_t$  is the unit vector along  $R_t$  directed toward the scatterer. Expressions for these vectors are

$$\hat{\mathbf{R}}_{rt} = \hat{\mathbf{x}} \cos A_{rt} \cos E_{rt} + \hat{\mathbf{y}} \sin A_{rt} \cos E_{rt} + \hat{\mathbf{z}} \sin E_{rt} \quad (\text{C.12})$$

$$\hat{\mathbf{R}}_t = \hat{\mathbf{x}} \cos A_t \cos E_t + \hat{\mathbf{y}} \sin A_t \cos E_t + \hat{\mathbf{z}} \sin E_t.$$

The emitter velocity vector is

$$\mathbf{V} = V(\hat{\mathbf{x}} \cos H + \hat{\mathbf{y}} \sin H). \quad (\text{C.13})$$

The differential Doppler shift is

$$\begin{aligned} f &= f_s - f_{dp} \\ &= \mathbf{V} \cdot \hat{\mathbf{R}}_t - \mathbf{V} \cdot \hat{\mathbf{R}}_{rt} \\ &= \mathbf{V} \cdot (\hat{\mathbf{R}}_t + \hat{\mathbf{R}}_{rt}) \end{aligned} \quad (\text{C.14})$$

where we have made use of the fact that  $\hat{\mathbf{R}}_{rt} = -\hat{\mathbf{R}}_{tr}$ . After plugging in terms we can write

$$\begin{aligned} f &= \frac{V}{\lambda} (\hat{\mathbf{x}} \cos H + \hat{\mathbf{y}} \sin H) \cdot [\hat{\mathbf{x}} (\cos A_t \cos E_t + \cos A_{rt} \cos E_{rt}) + \\ &\quad \hat{\mathbf{y}} (\sin A_t \cos E_t + \sin A_{rt} \cos E_{rt}) + \hat{\mathbf{z}} (\sin E_t - \sin E_{rt})] . \end{aligned} \quad (\text{C.15})$$

After carrying out the dot product we obtain

$$f = \frac{V}{\lambda} (\cos H (\cos A_t \cos E_t + \cos A_{rt} \cos E_{rt}) + \sin H (\sin A_t \cos E_t + \sin A_{rt} \cos E_{rt})) \quad (\text{C.16})$$

which is the desired expression. All the terms on the right side of the equation depend on measured or known quantities and emitter parameters we want to estimate. (To obtain  $\omega$  from  $f$  we multiply by  $2\pi$ .) As a check on this equation, we set the receiver height, emitter height, and  $A_{rt}$  equal to zero and compare to (A.9), the two-dimensional approximation. For this case, (C.16) yields

$$\begin{aligned}
f &= \frac{V}{\lambda} (\cos H (\cos A_t + 1) + \sin H \sin A_t) \\
&= \frac{V}{\lambda} (\cos H \cos A_t + \sin H \sin A_t + \cos H) \\
&= \frac{V}{\lambda} (\cos(H - A_t) + \cos H).
\end{aligned} \tag{C.17}$$

Since  $A_t$ , the angle to the scatterer from the emitter, is  $180 - \gamma$ , where  $\gamma$  was defined in Figure A.1, we can rewrite this result as

$$\begin{aligned}
f &= \frac{V}{\lambda} (\cos(H - 180 + \gamma) + \cos H) \\
&= \frac{V}{\lambda} (-\cos(H + \gamma) + \cos H)
\end{aligned} \tag{C.18}$$

which is equivalent to (A.9).

Delay-Doppler ridges were computed using the equations derived in Appendices A–C and the results are shown in Figure C.2. The two-dimensional treatment used to derive Equation (A.11) over-

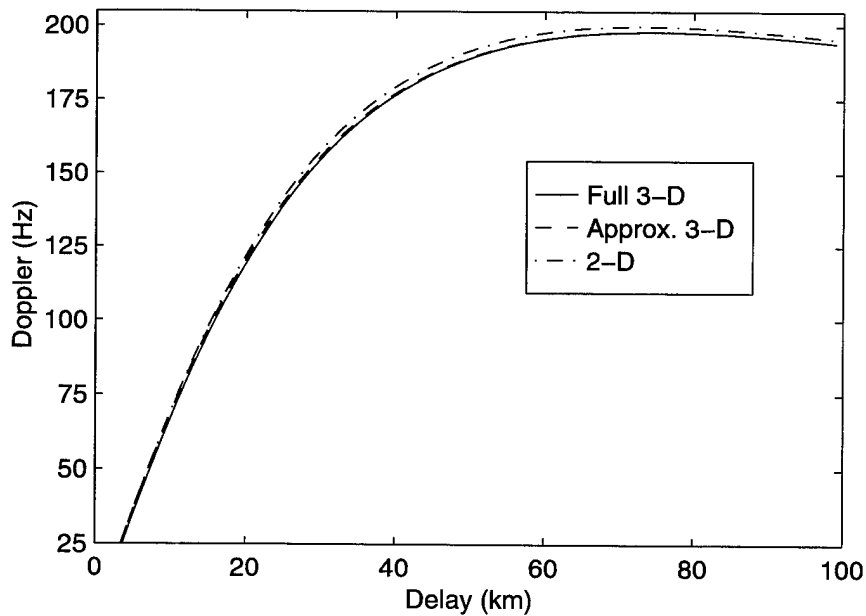


Figure C.2. Delay-Doppler ridge for three methods of calculation. The emitter range is 100 km and its heading is 90 degrees. The altitudes for the emitter and receiver are 8 km and 1.2 km, respectively.

predicts the Doppler frequency slightly because it uses azimuthal angles instead of conical angles. The approximate three-dimensional solution that resulted in Equation (B.4) is very close to the full three-dimensional solution because it accounts for the emitter conical angles. One can see from the figure that the approximate and full three-dimensional solutions are almost identical for this case.

## APPENDIX D

### ELEMENTS OF THE FISHER INFORMATION MATRIX

In this appendix we derive the expressions for the individual elements of the Fisher information matrix corresponding to the statistical formulation that was presented in Chapter 4. It was shown there that the elements of the Fisher matrix  $\mathbf{F}$  are

$$F_{ij} = \frac{2}{\sigma^2} \sum_{n=1}^N \left( \frac{\partial m_r(n)}{\partial \theta_i} \frac{\partial m_r(n)}{\partial \theta_j} + \frac{\partial m_i(n)}{\partial \theta_i} \frac{\partial m_i(n)}{\partial \theta_j} \right), \quad (\text{D.1})$$

with

$$m(n) = \sum_{p=1}^P a_p s(n - D_p) e^{j\omega_p(n - D_p)}. \quad (\text{D.2})$$

The scattering coefficient  $a_p$  and the emitter waveform  $s(n)$  are complex. The real and imaginary terms can be written in an amplitude-phase form as

$$\begin{aligned} m_r(n) &= \sum_{p=1}^P |a_p| |s(n - D_p)| \cos(\omega_p(n - D_p) + \varphi_{s(n-D_p)} + \varphi_{a_p}) \\ m_i(n) &= \sum_{p=1}^P |a_p| |s(n - D_p)| \sin(\omega_p(n - D_p) + \varphi_{s(n-D_p)} + \varphi_{a_p}). \end{aligned} \quad (\text{D.3})$$

For convenience, we combine the phase terms in  $\varphi_p$  and drop the absolute value symbols by redefining  $a_p$  and  $s(n)$  to be amplitudes and rewrite (D.3) as

$$\begin{aligned} m_r(n) &= \sum_{p=1}^P a_p s(n - D_p) \cos(\omega_p(\boldsymbol{\theta})n + \varphi_p) \\ m_i(n) &= \sum_{p=1}^P a_p s(n - D_p) \sin(\omega_p(\boldsymbol{\theta})n + \varphi_p). \end{aligned} \quad (\text{D.4})$$

The dependence of  $\omega$  on the emitter parameters  $\boldsymbol{\theta}$  has been indicated by their inclusion in the sum.

The entire parameter vector contains the desired emitter parameters and the 2P nuisance parameters. This is written as  $\{R, H, V, A, \varphi_1, \varphi_2, \dots, \varphi_P, a_1, a_2, \dots, a_P\}$ . The required derivatives are

$$\frac{\partial m_r(n)}{\partial \theta_i}, \frac{\partial m_i(n)}{\partial \theta_i} \quad (\text{D.5})$$

$$\frac{\partial m_r(n)}{\partial a_p}, \frac{\partial m_i(n)}{\partial a_p} \quad (D.6)$$

$$\frac{\partial m_r(n)}{\partial \varphi_p}, \frac{\partial m_i(n)}{\partial \varphi_p} \quad (D.7)$$

where  $\theta$  denotes the desired emitter parameters  $\{R, H, V, A\}$ . Differentiating (D.4) with respect to the desired parameters yields

$$\frac{\partial m_r(n)}{\partial \theta_i} = \sum_{p=1}^P -a_p s(n - D_p) \sin(\omega_p(\theta)n + \varphi_p) \frac{d\omega_p(\theta)}{d\theta_i} \quad (D.8)$$

$$\frac{\partial m_i(n)}{\partial \theta_i} = \sum_{p=1}^P a_p s(n - D_p) \cos(\omega_p(\theta)n + \varphi_p) \frac{d\omega_p(\theta)}{d\theta_i} \quad (D.9)$$

To complete the differentiation, we require the evaluation of

$$\frac{d\omega_p(\theta)}{d\theta_i} \quad (D.10)$$

for each of the desired parameters. For range  $R$ , heading  $H$ , and velocity  $V$ , we differentiate (A.11) with respect to each parameter. For convenience, we first rewrite (A.11) as

$$f = \frac{V}{\lambda} \left( \cos(H) - \cos\left(H + \sin^{-1} \frac{\mu}{v}\right) \right) \quad (D.11)$$

with

$$\mu = (D^2 + 2RD) \sin \phi \quad (D.12)$$

and

$$v = D^2 + 2R^2 + 2RD - 2(R^2 + DR) \cos \phi. \quad (D.13)$$

The required derivatives are

$$\frac{d\omega_p(\theta)}{dR} = 2\pi \left( \frac{V}{\lambda} \right) \left( \sin\left(H + \sin^{-1} \frac{\mu}{v}\right) \right) \left( \frac{1}{\sqrt{1 - \left(\frac{\mu}{v}\right)^2}} \right) \left( \frac{v(2D \sin \phi) - \mu(1 - \cos \phi)(4R + 2D)}{v^2} \right) \quad (D.14)$$

$$\frac{d\omega_p(\theta)}{dH} = 2\pi \frac{V}{\lambda} \left( -\sin H + \sin \left( H + \sin^{-1} \frac{\mu}{v} \right) \right) \quad (\text{D.15})$$

$$\frac{d\omega_p(\theta)}{dV} = 2\pi \frac{1}{\lambda} \left( \cos(H) - \cos \left( H + \sin^{-1} \frac{\mu}{v} \right) \right) . \quad (\text{D.16})$$

For altitude, we differentiate (B.5) with respect to  $A$  as

$$\frac{d\omega_p(\theta)}{dA} = 2\pi \frac{V}{\lambda} \left( \left( \frac{A}{R_t^2} \right) \left( 1 - \frac{A^2}{R_t^2} \right)^{-1/2} \cos \left( H + \sin^{-1} \frac{\mu}{v} \right) \right) \quad (\text{D.17})$$

with  $R_t$  given by

$$R_t = \frac{R^2 + 3D^2/2 + DR - (R^2 + DR)\cos\phi}{D + R - R\cos\phi} . \quad (\text{D.18})$$

We next differentiate (D.4) with respect to the nuisance parameters. The result is

$$\frac{\partial m_r(n)}{\partial \varphi_p} = -a_p s(n - D_p) \sin(\omega_p(\theta)n + \varphi_p) \quad (\text{D.19})$$

$$\frac{\partial m_i(n)}{\partial \varphi_p} = a_p s(n - D_p) \cos(\omega_p(\theta)n + \varphi_p) \quad (\text{D.20})$$

for the phase terms, and

$$\frac{\partial m_r(n)}{\partial a_p} = s(n - D_p) \cos(\omega_p(\theta)n + \varphi_p) \quad (\text{D.21})$$

$$\frac{\partial m_i(n)}{\partial a_p} = s(n - D_p) \sin(\omega_p(\theta)n + \varphi_p) \quad (\text{D.22})$$

for the amplitude terms. The sum over  $P$  is not present as it was for (D.8) and (D.9) because we have assumed that only the  $p^{\text{th}}$  term in the summation depends on  $a_p$  or  $\varphi_p$ .

With the above derivatives determined, the Fisher information matrix is formed by substituting the above expressions in (D.1). The results so far contain the emitter waveform  $s(n)$  explicitly. If we assume that the emitter waveform has variance  $\sigma_s^2$  and a correlation length that is less than the filter coefficients spacing, we can write the Fisher matrix in terms of  $\sigma_s^2$ . When this is true, the expected values of products of the form



$$\left( \sum_{k=1}^P a_k s(n - D_k) \right) \left( \sum_{l=1}^P a_l s(n - D_l) \right), \quad (\text{D.23})$$

where we have used the real-valued notation introduced for convenience, reduce to

$$\sum_{k=1}^P a_k^2 \sigma_s^2. \quad (\text{D.24})$$

Hence, for the emitter parameters terms, the diagonal elements of the Fisher information matrix can be written as

$$F_{ii} = \frac{N\sigma_s^2}{\sigma^2} \sum_{p=1}^P a_p^2 \left( \frac{d\omega_p(\theta)}{d\theta_i} \right)^2, \quad (\text{D.25})$$

and the general expression is

$$F_{ij} = \frac{N\sigma_s^2}{\sigma^2} \sum_{p=1}^P a_p^2 \frac{d\omega_p(\theta)}{d\theta_i} \frac{d\omega_p(\theta)}{d\theta_j}. \quad (\text{D.26})$$

For the nuisance parameters on the diagonal, the phase terms reduce to

$$\frac{Na_p^2 \sigma_s^2}{\sigma^2}, \quad (\text{D.27})$$

and the amplitude terms reduce to

$$\frac{N\sigma_s^2}{\sigma^2}. \quad (\text{D.28})$$

In these equations, the quantity  $\frac{\sigma_s^2}{\sigma^2}$  is the SNR for the direct-path signal and the quantity  $\frac{Na_p^2 \sigma_s^2}{\sigma^2}$  represents the integrated SNR at the  $p^{\text{th}}$  filter coefficient. The final form of the Fisher matrix for this assumption was noted in Chapter 5 and shown to contain a lot of zero terms off the diagonal.

## REFERENCES AND BIBLIOGRAPHY

1. W.W. Goj, *Synthetic-Aperture Radar and Electronic Warfare*, Artech House, Norwood, Mass., 1993.
2. R.L. Fante and J.A. Torres, "Cancellation of Diffuse Jammer Multipath by an Airborne Adaptive Radar," *IEEE Trans. Aerosp. Electron. Syst.*, AES-31, No. 2, April 1995, pp. 805-820.
3. A. Farina, *Antenna-Based Signal Processing Techniques for Radar Systems*, Artech House, Norwood, Mass., 1992.
4. S. Haykin, Editor, *Array Signal Processing*, Prentice-Hall, Inc., 1985.
5. M.V. Maksimov, et al., *Radar Anti-Jamming Techniques*, Artech House, Norwood, Mass., 1979.
6. G.W. Titi, "An Overview of the ARPA/NAVY Mountaintop Program," *IEEE Adaptive Antenna Systems Symposium*, November 1994.
7. R.A. Gabel, private communication, Lincoln Laboratory, MIT, March 1995.
8. S.M. Kogon, D.B. Williams, and E.J. Holder, "Beamspace techniques for hot clutter cancellation," *Proc. of IEEE Int. Conf. on Acoustics, Speech, and Signal Processing*, Volume 2, May 1996, pp. 1177-1180.
9. R.A. Gabel, private communication, Lincoln Laboratory, MIT, March 1994.
10. J.K. Jao, private communication, Lincoln Laboratory, MIT, March 1994.
11. G.W. Titi, private communication, Lincoln Laboratory, MIT, December 1994.
12. S.D. Coutts, "3-D Jammer Localization," *Proceedings of the Adaptive Sensor Array Processing (ASAP) Workshop*, Vol. 1, AD-A309824, Lincoln Laboratory, MIT, March 1996.
13. L.B Van Brunt, *Applied ECM*, Volume 2, EW Engineering, Inc., Dunn Loring, VA, 1982.
14. J.C. Hassab, *Underwater Signal and Data Processing*, CRC Press, Inc., Boca Raton, Florida, 1989.
15. P.J.D. Gething, *Radio Direction Finding and Superresolution*, Peter Peregrinus Ltd., London, United Kingdom, Second Edition, 1991.
16. H.H. Jenkins, *Small Aperture Radio Direction Finding*, Artech House, Inc., Norwood, MA, 1991.
17. D.H. Johnson and D.E. Dudgeon, *Array Signal Processing Concepts and Techniques*, Prentice-Hall, Inc., 1993.
18. W.C. Morchin, *Airborne Early Warning Radar*, Artech House, Inc., 1990.
19. F.J. Berle, "Mixed triangulation/trilateration technique for emitter location," *IEE Proceedings*, Vol. 133, Pt. F, No. 7, December 1996, 638-641.

20. B. Braban and J.F. Grandin, "A problem of multilocalization of radar emitters in counter-measures solved by image processing techniques," *Revue Technique Thomson-CSF*, Vol. 25, No. 1, March 1993, 239-259.
21. D. J. Torrieri, "Statistical Theory of Passive Location Systems," *IEEE Trans. Aerosp. Electron. Syst.*, AES-20, No. 2, March 1984, pp. 183-198.
22. W.E. Foy, "Position-Location Solutions by Taylor-Series Estimation," *IEEE Trans. Aerosp. Electron. Syst.*, AES-12, No. 2, March 1976, pp. 187-194.
23. B. Friedlander, "A Passive Localization Algorithm and Its Accuracy Analysis," *IEEE Journal of Oceanic Engineering*, Vol. OE-12, No. 1, January 1987, pp. 234-245.
24. M. Wax, "Position Location from Sensors with Position Uncertainty," *IEEE Trans. Aerosp. Electron. Syst.*, AES-19, No. 5, September 1983, pp. 658-662.
25. P.M. Schultheiss, J.P. Ianniello, "Optimum range and bearing estimation with randomly perturbed arrays," *J. Acoust. Soc. Am.*, Vol. 68, No. 1, July 1980, pp. 167-173.
26. R.F. Treharne, "Vertical Triangulation Using Skywaves," *Proceedings I.R.E.E.*, Australia, November 1967, pp. 419-424.
27. R.L. Johnson, Q.R. Black, and A.G. Sonsteby, "HF Multipath Passive Single Site Radio Localization," *IEEE Trans. Aerosp. Electron. Syst.*, AES-30, No. 2, April 1994, pp. 462-469.
28. H.C. Höring, "Comparison of the fixing accuracy of single-station locators and triangulation systems assuming ideal shortwave propagation in the ionosphere," *IEE Proceedings*, Vol. 137, Pt. F, No. 3, June 1990, pp. 173-176.
29. L.F. McMamara, "Ionospheric modeling in support of single station location of long range transmitters," *Journal of Atmospheric and Terrestrial Physics*, Vol. 50, No. 9, 1988, pp. 781-795.
30. K. Spingarn, "Passive Position Location Estimation Using the Extended Kalman Filter," *IEEE Trans. Aerosp. Electron. Syst.*, AES-23, No. 4, July 1987, pp. 558-567.
31. Y.T. Chan and J.J. Towers, "Sequential Localization of a Radiating Source by Doppler-Shifted Frequency Measurements," *IEEE Trans. Aerosp. Electron. Syst.*, AES-28, No. 4, October 1992, pp. 1084-1089.
32. K. Becker, "An Efficient Method of Passive Emitter Localization," *IEEE Trans. Aerosp. Electron. Syst.*, AES-28, No. 4, October 1992, pp. 1091-1104.
33. B. Friedlander, "Accuracy of source localization using multipath delays," *IEEE Trans. Aerosp. Electron. Syst.*, Vol. 24, No. 4, July 1988, pp. 346-359.
34. M.J.D. Rendas, J.M.F. Moura, "Cramer-Rao bound for Localization Systems in Multipath Environments," *IEEE Trans. Aerosp. Electron. Eng.*, Vol. 39, No. 12, pp. 2593-2610, December 1991.

35. H.P. Bucker, "Use of calculated sound fields and matched-field detection to locate sound sources in shallow water," *J. Acoust. Soc. Am.*, Vol. 59, No. 2, February 1976, pp. 368-373.
36. A.B. Baggeroer, W.A. Kuperman, and P.N. Milkalevsky, "An Overview of Matched Field Methods in Ocean Acoustics," *IEEE Journal of Oceanic Engineering*, Vol. OE-18, No. 4, October 1993, pp. 401-424.
37. A.B. Baggeroer and W.A. Kuperman, "Matched field processing: Source localization in correlated noise as an optimum parameter estimation problem," *J. Acoust. Soc. Am.*, Vol. 83, No. 2, February 1988, pp. 571-587.
38. C.H. Knapp and G.C. Carter, "The Generalized Correlation Method for Estimation of Time Delay," *IEEE Trans. on Acoust., Speech, Signal Processing*, Vol. ASSP-24, No. 4, August 1976, pp. 320-327.
39. G.C. Carter, "Coherence and Time Delay Estimation," *Proc. of the IEEE*, Vol. 75, No. 2, February 1987, pp. 236-255.
40. F.A. Reed, P.L. Feintuch, and N.J. Bershad, "Time Delay Estimation Using the LMS Adaptive Filter - Static Behavior," *IEEE Trans. on Acoust., Speech, Signal Processing*, Vol. ASSP-29, No. 3, June 1981, pp. 561-570.
41. F.A. Reed, P.L. Feintuch, and N.J. Bershad, "Time Delay Estimation Using the LMS Adaptive Filter - Dynamic Behavior," *IEEE Trans. on Acoust., Speech, Signal Processing*, Vol. ASSP-29, No. 3, June 1981, pp. 571-576.
42. P.M. Schultheiss and E. Weinstein, "Estimation of Differential Doppler Shifts," *J. Acoust. Soc. Am.*, Vol. 66, No. 5, November 1979, pp. 1412-1419.
43. M. Wax, "The Joint Estimation of Differential Delay, Doppler and Phase," *IEEE Trans. on Information Theory*, Vol. IT 28, No. 5, September 1982, pp. 817-820.
44. P.C. Chestnut, "Emitter Location Accuracy Using TDOA and Differential Doppler," *IEEE Trans. Aerosp. Electron. Syst.*, Vol. 39, No. 12, December 1991, pp. 2593-2610.
45. N. Levanon, "Interferometry against differential Doppler performance of two emitter location airborne systems," *IEE Proceedings*, Vol. 136, Pt. F, No. 2, April 1989, pp. 70-74.
46. H.A. Corriher, et al., Chapter XVII, "Elements of Radar Clutter," of *Principles of Modern Radar*, H.A. Ecker, ed., Georgia Institute of Technology, Atlanta, 1972.
47. N.J. Willis, *Bistatic Radar*, Artech House, Inc., Norwood, MA, 1991.
48. M.C. Jackson, "The Geometry of Bistatic Radar Systems," *IEE Proc.*, 133(7) Pt. F, December 1986.
49. R.A. Monzingo and T.W. Miller, *Introduction to Adaptive Arrays*, John Wiley & Sons, Inc., 1980.
50. B. Carlson, et al., "An Ultralow Sidelobe Adaptive Array Antenna," *The Lincoln Laboratory Journal*, Vol. 3, Number 2, 1990.

51. J. Ward, "Space-Time Adaptive Processing for Airborne Radar," Lincoln Laboratory Technical Report 1015, 13 Dec. 1994.
52. P. Beckman and A. Spizzichino, *The Scattering of Electromagnetic Waves from Rough Surfaces*, Artech House, Inc., Dedham, MA, 1987.
53. G.T. Ruck, D.E. Barrick, et al., *Radar Cross Section Handbook*, Volume 2, Plenum Press, New York, NY, 1970.
54. F.T. Ulaby, R.K. Moore, and A.K. Fung, *Microwave Remote Sensing, Active and Passive*, Volume 1-3, Addison-Wesley Publishing Co., Reading, MA, 1982.
55. A.K. Fung, *Microwave Scattering and Emission Models and Their Applications*, Artech House, Inc., Norwood, MA, 1994.
56. M. Skolnik, *Radar Handbook*, Chapter 17, McGraw-Hill, New York, 1990.
57. J. Illingworth and J Kittler, "A Survey of the Hough Transform," *Computer Vision, Graphics, and Image Processing*, 44, 87-116 (1988).
58. S.R. Deans, "Hough transform from the Radon transform," *IEEE Trans. Pattern Analysis and Machine Intelligence*. PAMI-3(2), March 1981.
59. P. Hough, Methods and means for recognizing complex patterns. U.S. Patent 3,069,654, 1962.
60. B.D. Carlson, E.D. Evans, and S.L. Wilson, "Search Radar Detection and Track with the Hough Transform, Part 1: System Concept," *IEEE Trans. Aerosp. Electron. Syst.*, 30, January 1994.
61. V.F. Leavers, *Shape Detection in Computer Vision using the Hough Transform*, Springer-Verlag, London, 1992.
62. H.B. Lee, "A Novel Procedure for Assessing the Accuracy of Hyperbolic Multilateration Systems," *IEEE Trans. Aerospace and Elect. Syst.*, January 1975.
63. M. Skolnik, *Radar Handbook*, Chapter 25, McGraw-Hill, New York, 1990.
64. J.G. Proakis, et al., *Advanced Digital Signal Processing*, Macmillan Publishing Co., New York, 1992.
65. S. Haykin, *Adaptive Filter Theory*, Prentice-Hall, Inc., New Jersey, 1986.
66. R. A. Gabel, "Signal Subspace Issues in TSI Mitigation," *Proceedings of the Adaptive Sensor Array Processing (ASAP) Workshop*, Vol. 1, AD-A309824, Lincoln Laboratory, MIT, March 1996.
67. S.M. Kay, *Fundamentals of Statistical Signal Processing: Estimation Theory*, PTR Prentice Hall, Inc., Englewood Cliffs, New Jersey, 1993.
68. H.L. Van Trees, *Detection, Estimation, and Modulation Theory, Part I*, John Wiley & Sons, New York, 1968.
69. A.D. Whalen, *Detection of Signals in Noise*, Academic Press, New York, 1971.

70. D. Rife, "Single-Tone Parameter Estimation from Discrete-Time Observations," *IEEE Transactions on Information Theory*, September 1974.
71. S. Stein, "Algorithms for Ambiguity Function Processing," *IEEE Trans. Acoust., Speech, Signal Processing*, Vol. ASSP-29, No. 3, June 1981.
72. R.A. Gabel, private communication, Lincoln Laboratory, MIT, March 1996.
73. J. Capon, "High-Resolution Frequency-Number Spectrum Analysis," *Proc. IEEE*, 57, 1969, pp.1408-1418.
74. M. Feder and E. Weinstein, "Parameter Estimation of Superimposed Signals Using the EM Algorithm," *IEEE Trans. Acoust., Signal Process.*, Vol. 36, April 1988, pp. 477-489.

REPORT DOCUMENTATION PAGE			Form Approved OMB No. 0704-0188	
<small>Public reporting burden for this collection of information is estimated to average 1 hour per response, including the time for reviewing instructions, searching existing data sources, gathering and maintaining the data needed, and completing and reviewing the collection of information. Send comments regarding this burden estimate or any other aspect of this collection of information, including suggestions for reducing this burden, to Washington Headquarters Services, Directorate for Information Operations and Reports, 1215 Jefferson Davis Highway, Suite 1204, Arlington, VA 22202-4302, and to the Office of Management and Budget, Paperwork Reduction Project (0704-0188), Washington, DC 20503.</small>				
1. AGENCY USE ONLY (Leave blank)	2. REPORT DATE 30 September 1998	3. REPORT TYPE AND DATES COVERED Technical Report		
4. TITLE AND SUBTITLE  Passive Localization of Moving Emitters Using Out-of-Plane Multipath		5. FUNDING NUMBERS  C — F19628-95-C-0002		
6. AUTHOR(S)  Scott D. Coutts				
7. PERFORMING ORGANIZATION NAME(S) AND ADDRESS(ES)  Lincoln Laboratory, MIT 244 Wood Street Lexington, MA 02420-9108		8. PERFORMING ORGANIZATION REPORT NUMBER  TR-1046		
9. SPONSORING/MONITORING AGENCY NAME(S) AND ADDRESS(ES)  DARPA/STO 3701 North Fairfax Drive Arlington, VA 22203		10. SPONSORING/MONITORING AGENCY REPORT NUMBER  ESC-TR-97-081		
11. SUPPLEMENTARY NOTES  None				
12a. DISTRIBUTION/AVAILABILITY STATEMENT  Approved for public release; distribution is unlimited.			12b. DISTRIBUTION CODE	
13. ABSTRACT (Maximum 200 words)  <p>The purpose of this work is to establish how a moving emitter can be localized by a passive receiver through the use of out-of-plane multipath signals reflected by the terrain. This is a novel localization technique that assumes no a priori knowledge of the location of the multipath sources. The emitter parameters of range, heading, velocity, and altitude are estimated by exploiting the correlation between the direct-path signal and the delayed, attenuated, and Doppler modulated signals reflected by the terrain.</p> <p>Two basic assumptions about the terrain scattering properties lead to different maximum likelihood (ML) estimators of emitter parameters. The first assumption is that the terrain scattering is fundamentally homogeneous; in this case the ML estimator is found to have the structure of a time-varying FIR filter. The second assumption is that the terrain scattering is fundamentally inhomogeneous and dominated by a number of discrete scatterers. This assumption leads to a two-part estimator which first estimates the scattering parameters of azimuth, differential delay, and Doppler shift, and then estimates the emitter parameters using the scatterer parameter estimates. The Cramer-Rao lower bounds of the variances for each estimator are derived and used to study estimator performance for several scenarios.</p> <p>The proposed estimators are successfully demonstrated using field data collected at White Sands Missile Range during the DARPA/Navy Mountaintop program. Several extensions to the basic results are considered such as localizing pulsed and self-correlated emitters, multiple emitters, and the effects of receiver motion.</p>				
14. SUBJECT TERMS passive localization multipath bistatic clutter			15. NUMBER OF PAGES 153	
			16. PRICE CODE	
17. SECURITY CLASSIFICATION OF REPORT Unclassified	18. SECURITY CLASSIFICATION OF THIS PAGE Unclassified	19. SECURITY CLASSIFICATION OF ABSTRACT Unclassified	20. LIMITATION OF ABSTRACT Same as Report	